Improving Image Reconstruction and Machine Learning Methods in Breast Microwave Sensing

Tyson Adam Reimer

A thesis submitted to the Faculty of Graduate Studies of

The University of Manitoba

In partial fulfillment of the requirements of the degree of

Master of Science

Department of Physics and Astronomy

The University of Manitoba

Winnipeg, Manitoba, Canada

©2020 by Tyson Adam Reimer

Abstract

Breast microwave sensing (BMS) is an emerging modality that has the potential to be used as a breast cancer screening technique but challenges remain before the modality is suitable for clinical use. Improvements to image-based and machine learning tumor-detection methods are required. This thesis presents novel improvements in image reconstruction and machine learning methods. This work presents the development of the largest open-access experimental dataset in the published BMS literature to-date, the University of Manitoba Breast Microwave Imaging Dataset (UM-BMID). The impact of the inverse chirp z-transform (ICZT) on radar-based image reconstruction was compared to that of the standard inverse discrete Fourier transform using a subset of this dataset. The ICZT was found to reduce image artifacts, improve image contrast, and increase tumor-detection in reconstructions. A novel reconstruction method, the iterative delay-and-sum (itDAS) beamformer, was compared to two literature standard approaches. The novel method improved image contrast by as much as 249% on average and allows for the implementation of correction factors to improve the radar signal model used in the literature standard algorithms. Three correction factors were examined and modeling the output pulse of the BMS system significantly increased the contrast of itDAS reconstructions. The diagnostic capability of machine learning methods in BMS was investigated using UM-BMID. The area under the curve of the receiver operating characteristic curve of a convolutional neural network was estimated to be between $(76 \pm 3)\%$ and $(91 \pm 3)\%$, where the upper estimate is obtained when the testing set is constrained to consist of phantoms with breast volumes that are within the breast volume bounds of the training set and when the tumor is located at the same vertical position as the antennas. This thesis has set the stage for future large-scale analyses in BMS through the development of the first and largest open-access dataset in the published literature and through the promising results obtained with the application of machine learning methods and the novel itDAS beamformer.

Contributions

The following are the primary contributions presented by the author in this thesis:

- Development of the open-access University of Manitoba Breast Microwave Imaging Dataset (UM-BMID), the first open-access experimental dataset in the breast microwave sensing literature and the largest presented in the literature to-date by an order of magnitude.
- Experimental evaluation of the effects of the inverse chirp z-transform for frequency-to-time domain conversion on radar-based image reconstruction with respect to image artifacts, contrast, localization error, and tumor detection.
- Development of the novel iterative delay-and-sum (itDAS) and iterative delay-multiply-and-sum (itDMAS) reconstruction algorithms and a comparison of the itDAS and itDMAS algorithms to the literature standard delay-and-sum and delay-multiply-and-sum algorithms with respect to image contrast and localization error.
- Implementation and evaluation of three correction factors with the itDAS algorithm, correcting for the beam pattern of the system antennas, the frequency-dependent gain of the antennas, and the output time-domain pulse of the system.
- Evaluation of the diagnostic performance of logistic regression, dense neural network, and convolutional neural network (CNN) classifiers for tumor-detection using UM-BMID and a comparison between these methods and reconstructed image-based methods for tumor-detection.
- Evaluation of three methods to improve model generalization: the use of a simplified CNN architecture, the use of two novel data augmentation strategies, and the use of a reduced sinogram data representation model.

Acronyms

BMS Breast Microwave Sensing. i, 3, 5, 6, 87

CNN Convolutional Neural Network. i, 66

DAS Delay-and-Sum. i, 6, 7, 27, 29, 88

DMAS Delay-Multiply-and-Sum. i, 7, 27, 34, 88

DNN Dense Neural Network. i, 66, 81

FD Frequency Domain. i, 31

FWHM Full Width at Half Maximum. i, ix, 37

ICZT Inverse Chirp z-Transform. i, 31

IDFT Inverse Discrete Fourier Transform. i, 31

IQM Image Quality Metric. i, 4

itDAS Iterative Delay-and-Sum. i, 27, 34

itDMAS Iterative Delay-Multiply-and-Sum. i, 34

ML Machine Learning. i, 8

MLEM Maximum-Likelihood Expectation-Maximization. i, 33

MRI Magnetic Resonance Imaging. i, 2

PET Positron Emission Tomography. i, 8, 33

ROC AUC Area Under the Curve of the Receiver Operating Characteristic Curve. i, 23, 24

SCR Signal-to-Clutter Ratio. i, 39

SFR Sample to Feature Ratio. i, 73, 74

SMR Signal-to-Mean Ratio. i, 39

SVM RBF Support Vector Machine with Radial Basis Function Kernel. i, ix, 24, 25

TD Time Domain. i, 31

UM-BMID University of Manitoba Breast Microwave Imaging Dataset. i, 12, 14, 25, 63, 87

VNA Vector Network Analyzer. i, 19

Acknowledgments

I would like to thank Prof. Stephen Pistorius for acting as my supervisor during my M.Sc. and during my time as an undergraduate summer research student. I appreciate every opportunity that has been provided to me and I sincerely cherish my time in the research group.

I would also like to extend my thanks to the colleagues I've had in the research group over the past few years. I thank Jorge Sacristan and Diego Rodriguez-Herrera for the many valuable discussions we've had over the years and Mario Solis-Nepote for the generous and valuable mentorship he provided to me during my undergraduate and graduate studies. I would also like to thank the undergraduate students I have had the pleasure to work with during my time as a graduate student - I hope that they enjoyed their time in our research group as much as I enjoyed our time together.

I extend my sincerest thanks to the support staff in the Department of Physics and Astronomy - Susan Beshta, Robyn Beaulieu, and Aymsley Bishop-Mahon. They have provided constant support during my graduate and undergraduate studies at the University of Manitoba.

I extend my gratitude to the funding organizations that have supported my studies at the University of Manitoba - the National Science and Engineering Research Council of Canada, the CancerCare Manitoba Foundation, the University of Manitoba, and the Canadian Breast Cancer Foundation.

I thank my friends and family for support during my studies. The past few years have moved quickly, and I appreciate their patience and support through this time. I am extremely fortunate to have an excellent group of people in my life.

Contents

Abstract i

Contributions ii

Acronyms iii

Acknowledgments iv

List of Tables vii

List of Figures viii

1 Introduction to Microwave Sensing for Breast Cancer Detection 1

1.1 Background and Justification 1

1.2 Introduction to Breast Microwave Sensing 3

1.3 Current Image Reconstruction Methods 5

1.4 Past Machine Learning Investigations in BMS 8

1.4.1 Machine Learning: Terminology and Methods 8

1.4.2 Machine Learning in BMS 9

1.5 Problem Definition 10

1.5.1 Problem Statement 10

1.5.2 Thesis Objectives 11

2 Generation of an Open-Access Experimental Dataset 12

2.1 Introduction 12

2.2 Methods 14

2.2.1 3D-Printed MRI-Derived Breast Phantoms 14

2.2.2 Pre-Clinical Breast Microwave Imaging System 19

2.2.3 Experimental Scan Procedure and Dataset Generation 20

2.2.4 Initial Machine Learning Methods 22

2.3 Results and Discussion 24

2.3.1 UM-BMID: The University of Manitoba Breast Microwave Imaging Dataset 24
2.3.2 Initial Machine Learning Analysis for Tumor Detection in UM-BMID . . . 24
2.4 Conclusions . . . 25

3 Improving Signal Processing and Image Reconstruction Methods 27
3.1 Introduction to Image Reconstruction in Breast Microwave Imaging . . . 27
3.2 Methods . . . 29
3.2.1 Literature Standard Beamformers . . . 29
3.2.2 Propagation Speed Estimation and Skin Suppression . . . 29
3.2.3 Frequency-to-Time Domain Conversion . . . 31
3.2.4 The itDAS Reconstruction Algorithm . . . 33
3.2.5 Implementation of Correction Factors in the itDAS Algorithm . . . 34
3.2.6 Selected Data for Image Reconstruction Analysis . . . 38
3.2.7 Image Quality Metrics . . . 39
3.3 Results . . . 40
3.3.1 Effects of the ICZT on Frequency-to-Time Domain Conversion . . . 40
3.3.2 Evaluation of the Novel itDAS Algorithm . . . 43
3.3.3 Reconstructions using Correction Factors with the itDAS Beamformer . . . 43
3.4 Discussion . . . 45
3.4.1 Determination of Optimal Time-Domain Resolution with the ICZT . . . 45
3.4.2 Comparing the itDAS Algorithm to DAS and DMAS . . . 51
3.4.3 Modeling Antenna and System Parameters in itDAS . . . 55
3.5 Conclusion . . . 58

4 Application of Machine Learning Methods for Tumor-Detection 60
4.1 Introduction to Machine Learning Methods in BMS . . . 60
4.2 Methods . . . 62
4.2.1 Defining Tumor-Detection as a Binary Classification Problem . . . 62
4.2.2 Selected Datasets . . . 63
4.2.3 Data Structure and Model Selection . . . 64
4.2.4 Machine Learning Models and Training Methods . . . 67
4.3 Results . . . 68
4.3.1 Classifier Performance on UM-BMID Gen-1 . . . 68

4.3.2 Classifier Performance on UM-BMID Gen-2 70
4.4 Discussion 72
4.4.1 Interpretation of Results and Limitations 72
4.4.2 Reducing the Dimensionality of the Feature Space 74
4.4.3 Data Augmentation Strategies 74
4.4.4 Revisiting Model Architecture Selection 76
4.4.5 Evaluation of Model Generalization 76
4.4.6 Viability of Machine Learning for Automated Tumor Detection Compared to Image-based Detection in Breast Microwave Sensing 82
4.5 Conclusions 85

5 Conclusions **87**

A Appendix **91**

References **107**

List of Tables

2.1 Second Generation Phantom Properties 18

3.1 Breast Density and BI-RADS Classifications of Phantoms Used in Beamformer Comparisons 38

3.2 Image Quality Metrics of Reconstructions Displayed in Figure 3.7 43

3.3 Image Quality Metrics of Reconstructions Displayed in Figure 3.8 45

4.1 BI-RADS Assessment Categories [5] 62

4.2 Comparison of the Two Generations of UM-BMID, Adapted from [44] 64

4.3 Parameters of the Adam Optimizer used in this Investigation 68

4.4 Effects of Sinogram Reduction and Data Augmentation on UM-BMID Gen-2 . . . 76

4.5 Effects of Techniques to Improve Model Generalization on CNN Model Performance 77

4.6 Comparison of Image-based Detection by DAS, DMAS, and itDAS 84

List of Figures

2.1 First generation of 3D-printed MRI-derived breast phantoms. Adipose shells labeled A1 through A3, fibroglandular shells labeled F1 through F5. 16

2.2 Glass bulbs (filled with saline solution) used to model tumors. 0.5 cm radius tumor shown at left, 1.0 cm radius tumor shown in the middle, and 1.5 cm radius tumor shown at right. 17

2.3 Second generation of 3D-printed MRI-derived breast phantoms. (a) Adipose shells labeled A1 through A3 and A11 through A16, (b) fibroglandular shells labeled F1 through F5 and F11 through F14. 18

2.4 Radar-based breast microwave sensing system developed in our laboratory; (a) displays the top of the bed system and (b) displays the radar module. 20

2.5 Classification performance obtained by logistic regression classifier on generation one scans in UM-BMID compared to performance obtained by SVM RBF on simulated data from [84]. Figure modified from [44]. 25

3.1 Time-domain radar signals obtained using the IDFT and ICZT (evaluated at 1024 points between 0 ns and 6 ns response times). Signals obtained from one antenna position from an experimental phantom scan. Figure adapted from [104]. 33

3.2 Antenna beam pattern model and data obtained from antenna datasheet. A piecewise quadratic function was used to model the beam pattern. Shaded region indicates fit uncertainties. 36

3.3 Antenna gain model and data obtained from antenna datasheet. 37

3.4 Measured VNA output pulse and Gaussian function used to model the output pulse. The variance of the Gaussian was extracted from measured S_{21} and used to model the Gaussian pulse function $p(t)$. The full-width at half-maximum (FWHM) of the model and the measured pulse are displayed. 37

3.5 DMAS reconstructions of a 15 mm radius lesion in a Class I phantom using (a) the IDFT and (b) the ICZT, and of a 15 mm radius lesion in a Class III phantom using (c) the IDFT and (d) the ICZT. The solid green circle indicates the tumor location, the dashed white circle indicates the approximate phantom boundary, and the dashed black circle indicates the antenna trajectory during the scan. Each image is normalized to its maximum intensity value. Figure adapted from [104]. 41

3.6 (a) SMR and (b) SCR of images in Fig. 3.5. Figure adapted from [104]. 42

3.7 Reconstructions of breast phantoms by (left to right) the DAS, DMAS, itDAS, and itDMAS beamformers. (a-d) display the reconstructions of a 15 mm radius lesion in a Class I (A2F1) phantom, (e-h) display the reconstructions of a 10 mm radius lesion in a Class II (A3F4) phantom, (i-l) display the reconstructions of a 15 mm radius lesion in a Class III (A2F4) phantom, and (m-p) display the reconstructions of a 15 mm radius lesion in a Class IV (A1F4) phantom. Each image is normalized to its maximum intensity. The dashed black circle indicates the antenna trajectory during the scan, the dashed white line indicates the approximate breast phantom boundary, and the solid green circle indicates the known tumor position. Figure adapted from [105]. 44

3.8 itDAS reconstructions of the A1F1 Class II phantom containing a 15 mm radius tumor produced using (a) no correction factors, (b) the correction factor for the antenna's beam pattern, as described in Eq. 3.5, (c) the correction factor for the antenna's gain, as described in Eq. 3.6, and (d) the correction factor for the VNA's output pulse, as described in Eq. 3.7. Each image is normalized to its maximum intensity. The dashed black circle indicates the antenna trajectory during the scan, the dashed white line indicates the approximate breast phantom boundary, and the solid green circle indicates the known tumor position. 45

3.9 DMAS reconstructions of a 15 mm radius lesion in a Class III phantom using (a) the IDFT, (b) the ICZT with 100 time-points from 0 ns to 6 ns (60.6 ps time-step size), (c) the ICZT with 200 time-points (30.2 ps time-step size), and (d) the ICZT with 550 time-points (10.9 ps time-step size). Figure adapted from [104]. 46

3.10 Localization error of the Class III reconstructions as a function of the time-step size. The dashed line indicates the radius of the tumor. Figure adapted from [104]. . 47

3.11 Average total absolute-difference of images produced using time-step sizes greater than 5.9 ps and the image produced after using the ICZT for FD-to-TD conversion with a time-step size of 5.9 ps, for 10 scans of the Class III phantom. Standard deviations of the average total absolute-difference over the images from the 10 scans are the displayed uncertainties. The shaded red region indicates the 99.7% confidence intervals on the fit. Figure adapted from [104]. 49

3.12 Average (a) SMR and (b) SCR for the reconstruction algorithms using scans of phantoms representative of the four BI-RADS density classification categories. Figure adapted from [105]. 53

3.13 The measured sinogram (after ideal skin suppression) and the forward projection of the image estimate at each of the first six iterations during the itDAS reconstruction (displayed in Figure 3.7 (c)) of the Class I phantom. Each sinogram and forward projection has been normalized to have a maximum value of unity. Figure adapted from [105]. 54

3.14 The models of the time-domain representation of the antenna's frequency-dependent gain and the output pulse of the VNA used in the implementation of the respective correction factors. 56

3.15 Average (a) SMR and (b) SCR of reconstructions for phantoms of each BI-RADS density classification category produced by the itDAS reconstruction algorithm using various correction factors. 57

4.1 Sinogram obtained from phantom scan. 65

4.2 Sinogram obtained from scan of 2 mm diameter metal rod in imaging chamber. . . 66

4.3 Average ROC AUC over cross validation sets to determine optimal number of training epochs when using the first generation of UM-BMID. Standard deviation of ROC AUC over the cross validation sets indicated in shaded regions. The optimal number of training epochs was determined to be 105. 69

4.4 Diagnostic performance of logistic regression and CNN classifiers on test set of first generation scans of UM-BMID. 70

4.5 Diagnostic performance of logistic regression and CNN classifiers on test set of second generation scans of UM-BMID. 71

4.6 Diagnostic performance of logistic regression and CNN classifiers on first generation of UM-BMID after training on second generation of UM-BMID. 72

4.7 Effects of data augmentation strategies on the diagnostic performance of CNN classifier on first generation of UM-BMID after training on second generation of UM-BMID. 78

4.8 Diagnostic performance of the (simplified) CNN classifier on each adipose shell after training on scans of all phantoms excluding that adipose shell. Full data augmentation was used during training. Adipose shell volume also displayed for reference. 79

4.9 Diagnostic performance of logistic regression and CNN classifiers on first generation of UM-BMID after training on second generation of UM-BMID when using the full sinogram data representation, data augmentation strategies, and the simplified CNN architecture. 81

1. Introduction to Microwave Sensing for Breast Cancer Detection

---

This chapter introduces breast microwave sensing as a potential method for breast cancer detection. Breast microwave sensing systems and methods are described and the standard methods for image reconstruction and past applications of machine learning methods in breast microwave sensing are reviewed. The chapter concludes with the problem statement of this thesis.

1.1 Background and Justification

Breast cancer is projected to be the most prevalent cancer in Canadian women in 2020 [1]. The Canadian Cancer Society estimates that 1 in 8 women in Canada will develop breast cancer at some point in their life [2]. Breast cancer detection is required to deliver treatment and medical imaging systems allow for non-invasive cancer diagnosis.

The standard method of breast cancer detection is x-ray mammography. Mammography operates by irradiating the breast with ionizing x-rays, and the contrast in the x-ray attenuation of the tissues is used to create an image of the breast. While mammography is widely used as a breast cancer screening tool, its benefits have been questioned [3]. Its use of x-rays delivers a dose of ionizing radiation to the patient during a scan, and this exposure to ionizing radiation introduces an inherent health risk that must be weighed against the potential benefits of mammography as a diagnostic tool. Currently, this risk-benefit analysis has resulted in mammography being used as a screening tool only for women above a particular age - in Canada, mammography is currently used as a breast cancer screening tool only for women above 50 years of age [4].

There are two primary healthy tissues of interest in the breast - adipose tissue and fibroglandular tissue. The breast density (relative amount of fibroglandular tissue to adipose tissue) of the breast [5] is one factor that affects the diagnostic performance of mammography [6, 7]. High-density breasts (relatively large fibroglandular content) present a particular challenge to mammography [6,7], and given that 42.9–43.1% of American women between the ages of 40–74 have dense breasts [8], this also presents a challenge to the use of mammography as a screening tool. High breast density is also most prevalent in younger women [8], which, in combination with mammography's use of ionizing radiation, have limited its use as a screening tool in younger women [4].

The merits of mammography as a breast cancer screening tool have also been questioned due to its relatively high false-positive rate [3]. The cumulative risk of a false-positive after ten mammograms is estimated to be between 20-60% [3]. A false-positive diagnosis results in unnecessary medical interventions, typically further diagnostic imaging or an invasive biopsy. In addition to the healthcare costs associated with unnecessary follow-up activities, the stress and anxiety that may be experienced by an individual who received a false-positive diagnosis are unnecessary negative patient outcomes. The costs associated with false-positives must be considered when evaluating the use of mammography as a screening tool.

Other diagnostic imaging modalities have costs associated with them that significantly limit their viability as a cancer screening tool. Magnetic resonance imaging (MRI) is an expensive and time-consuming method. The large cost, limited availability, and challenges with specificity limit MRI from being used as a breast cancer screening tool [9].

Ultrasound can be used to detect the presence of cancerous lesions, and while it has a good specificity, it requires a trained operator and may have a higher false-positive rate than mammography [9]. While ultrasound can be used as a diagnostic tool for follow-up investigations (after a mammogram) and may increase sensitivity [9], the requirement of having a trained operator and the potential of increasing the false-positive rate [9] over that of mammography limits the use of ultrasound as a screening tool.

Ultrasound and MRI have features that restrict their utility as screening tools, and the high false-positive rate of mammography [3] and its use of ionizing x-ray radiation are challenges that limit its viability as a screening tool. The prevalence of breast cancer [1, 2] and the challenges present in current imaging systems [3, 6, 7, 9] have prompted research into alternative methods for breast cancer detection.

1.2 Introduction to Breast Microwave Sensing

Investigations into the use of microwave-based systems for breast cancer detection have been ongoing for over two decades [10–12]. Low-power microwave systems have the potential to be used as a breast cancer detection tool that uses non-ionizing radiation [11–14]. Breast microwave sensing (BMS) systems operate by interrogating the tissues with an incident microwave field, typically operating at frequencies between 900 MHz and 10 GHz [11, 12, 14]. When an incident field interacts with the breast tissues, the tissues produce a scattered field, and the resultant field can be measured using antenna-based systems.

The complex dielectric constant ε completely determines the interaction of the electromagnetic field with the breast tissues,

$$\varepsilon = \varepsilon' + j\varepsilon'', \tag{1.1}$$

where ε' and ε'' are the real and imaginary parts of the constant, respectively. It is more convenient to discuss the relative dielectric constant ε_r,

$$\varepsilon_r = \frac{\varepsilon}{\varepsilon_0} = \varepsilon_0\left(\varepsilon_r' + j\varepsilon_r''\right). \tag{1.2}$$

Early measurements of the dielectric properties of breast tissues reported contrasts as high as 10:1 between cancerous and healthy tissues [15]. This promising contrast prompted research efforts focusing on the use of microwave-based imaging systems for breast cancer detection. Higher

contrast may result in higher specificity, addressing the concern of a screening tool with a high false-positive rate. While recent and larger-scale investigations have reported the contrast to be between 8–10% [16], this contrast is still favorable to that of mammography. Microwave-based imaging systems have the potential to be non-ionizing (allowing for repeated use throughout a patient's life, without delivering a dose of ionizing radiation), higher-contrast (resulting in a lower false-positive rate), and less expensive than mammography.

These potential benefits have prompted several research groups to develop BMS systems capable of clinical operation [17–21] and experimental investigations using these systems have been performed with phantoms and patients.

While research into the viability of BMS as a breast cancer screening tool has been ongoing for the past two decades and several groups have performed patient studies [19, 21–35], several challenges remain before BMS systems are ready for regular clinical use as a screening tool. Image reconstructions techniques are an active area of research [36–41] and only two studies have presented a comparison of these reconstruction methods on phantom [42] and patient data [35]. The performance of reconstruction methods as a function of breast size, breast density, tumor size, and tumor position has not been studied. The development of robust image quality metrics (IQMs) is also an area of research that has received little attention from the community. Objective tumor-detection methods, via machine learning or other algorithmic techniques, has also not been rigorously investigated.

Imaging system design varies widely - some groups have developed monostatic [19,43], bistatic [17], or multistatic (60 antennas in [21]) imaging systems that perform measurements in the frequency domain using a vector network analyzer, and other research groups have opted for time-domain hardware [20]. Most systems have been designed to be used with a coupling medium or gel [18–21] to minimize contrast at the exterior skin interface, while two research groups have designed their systems for in-air operation [17, 43]. The antenna design, number of antennas, and antenna positioning systems vary across the literature [17, 18, 20, 21, 43], and no gold-standard exists. Phantom

design and development are also active areas of work [44–51].

Despite these numerous remaining challenges, several patient studies have been performed [19, 21–35]. While patient investigations have examined up to 225 patients [34], controlled experimental investigations have been limited to small-scale phantom studies (up to 5 unique phantoms [52]). Phantoms allow for controlled and reproducible experimentation. Due to the many remaining challenges in BMS, phantom experiments are still needed to investigate and evaluate methods under controlled conditions, and the relatively large-scale patient studies may be premature, given the lack of control in patient studies and the difficulty in interpreting patient imaging results (due in part to image registration challenges).

This work aims to address three of the present challenges in BMS. The largest dataset in the published literature to-date was developed [44]. The dataset was generated using experimental scans of MRI-derived phantoms and is the first open-access dataset in BMS, to the best of our knowledge [44] (available at `https://bit.ly/UM-bmid`). This dataset was developed to facilitate relatively large-scale analysis of BMS methods on an experimental dataset collected under controlled conditions and was made open-access to facilitate analysis by the research community on a standard dataset. A novel image reconstruction technique was developed and compared to literature standard methods using experimental scans of an array of breast phantoms, and the viability of machine learning methods for automated tumor detection was investigated using the open-access experimental dataset described herein.

1.3 Current Image Reconstruction Methods

Image reconstruction methods in BMS can be broadly categorized as tomographic or radar-based approaches. Tomographic techniques aim to reconstruct maps of the complex permittivity of the tissues [53–58]. Tomographic reconstruction algorithms begin from the full electromagnetic inverse scattering model and define the reconstruction task as an optimization problem [53–59].

While these methods typically make some assumptions about the physical model, they move from the full electromagnetic model toward a simpler approach through approximations.

Breast microwave tomography has seen success primarily in simulation studies [58,60–68] and translation to experiment is challenging and ongoing. Applications of these techniques to experimental systems have been presented in a small number of studies [18,53,55], but these studies have been exclusively performed by the research group at Dartmouth College. Tomographic algorithms are also computationally expensive and can take hours or days of computation time to produce a reconstructed image.

Radar-based reconstruction algorithms do not reconstruct maps of the dielectric properties of the breast. Instead, these methods are used to reconstruct images that display a reflectivity map of the imaging region, in which regions of strong reflections are apparent. Radar-based methods have been widely used in phantom-based experiments [20,36–43,45,50,52,69] and in patient studies [19, 24, 25, 28, 35]. These approaches have been demonstrated to be advantageous compared to tomographic techniques due to their shorter computation time (typically taking seconds to reconstruct an image) and their relatively rapid transition from simulation [10, 70] to experiment in several independent research groups [20, 71–73].

The first radar-based method proposed for image reconstruction in BMS is the current literature standard algorithm: the delay-and-sum (DAS) beamformer [10]. This method synthetically focuses the individual radar responses to reconstruct a reflectivity map,

$$I(\mathbf{r}) = \sum_{m=1}^{M} \mathbf{s}_m\big(t_m(\mathbf{r})\big), \tag{1.3}$$

where $\mathbf{s}_m$ is the reflected radar signal measured at the m^{th} position and $t_m(\mathbf{r})$ is the time-of-flight,

$$t_m(\mathbf{r}) = 2\frac{\left|\mathbf{r}-\mathbf{r}_m\right|}{v} \tag{1.4}$$

where v is the average propagation speed and $\mathbf{r}_m$ is the position of the m^{th} antenna.

This approach uses time-domain signals measured at various positions in the imaging domain to reconstruct an image. The estimated time-of-flights $t_m(\mathbf{r})$ of response positions $\mathbf{r}$ are used to back-project the individual radar signals onto the image-space.

The initial success of this approach [10, 71] prompted the development of several DAS derivatives. Despite the initial promising performance of the DAS beamformer, the method has several limitations. The DAS algorithm neglects most of the physics of microwave imaging, the images reconstructed using DAS have high intensity clutter responses that can obfuscate the tumor response [35, 42], and the accurate estimation of the times-of-flight $t_m(\mathbf{r})$ is required to obtain high-quality reconstructions [69].

Several DAS-derivatives have been developed to address these challenges. The primary focus in the development of these algorithms has been clutter reduction, with the goal of reconstructing images with a higher tumor-to-clutter contrast. One of the major DAS-derivatives is the delay-multiply-and-sum (DMAS) beamformer [38]. This method artificially increases the number of radar-signals used to reconstruct the image through pair-wise signal multiplication,

$$I(\mathbf{r}) = \sum_{m=1}^{M-1} \sum_{n=m+1}^{M} \mathbf{s}_m(t_m(\mathbf{r})) \cdot \mathbf{s}_n(t_n(\mathbf{r})). \tag{1.5}$$

This method does not improve the physics model of the reconstruction process over DAS, but it has been empirically demonstrated to produce images with higher tumor-to-clutter ratios in both phantom [42] and patient studies [35]. Other DAS-derivatives include the improved delay-and-sum [40], the coherence-factor delay-and-sum [41], and the channel-ranked delay-and-sum [39]. DAS-derivatives have been developed primarily to reduce clutter intensity and increase contrast in images by rewarding signal coherence [38, 40, 41]. The DAS algorithm and DAS-derivatives have been used in many patient imaging studies [19, 21–33].

Other radar-based methods have been proposed [74–77], but the DAS and DMAS beamformer have been used as standards-of-comparison [35, 38, 42]. Despite their widespread use, DAS and DMAS have limitations. Both algorithms require accurate estimation of the time-delays $t_m(\mathbf{r})$ and

use a simple radar signal model. This model neglects the physics of electromagnetic scattering and can not account for the antenna beam pattern and frequency-dependent gain, signal attenuation and dispersion within the breast, and other path-dependent or system-specific effects. While DMAS does improve image contrast over DAS [35, 42], the pair-wise signal multiplication does not have a physical justification, and low image contrast is still a challenge, particularly in air-based systems [78].

To address these challenges, a novel image reconstruction technique was developed. An iterative structure used in positron emission tomography (PET) [79] was adapted for use with the standard DAS beamformer. This iterative structure allows select components of the physics model to be incorporated into the reconstruction algorithm, enabling the evaluation of their individual effects on image quality.

1.4 Past Machine Learning Investigations in BMS

Machine learning (ML) methods have been used in many research applications in recent years and have been proposed for use as an automated diagnosis tool in medical applications. Machine learning techniques have the potential to perform automated cancer detection using the measured electromagnetic information, potentially bypassing the challenges in image reconstruction and image-based tumor detection in BMS.

1.4.1 Machine Learning: Terminology and Methods

ML methods use computationally intelligent algorithms to perform a task. In general, this involves mapping input information (features) that describe a specific instance/sample to a target outcome. ML algorithms typically learn this input-output relationship from a set of data consisting of individual samples described by features and known outcomes. After training on this known dataset (the training set), the performance of the algorithm can be evaluated using a testing dataset.

For example, suppose that we want to predict the presence of lung cancer given an x-ray image of the lungs. The x-ray image pixel intensities can be used as numerical features to describe the people who underwent the imaging procedures. In this example, the individual people are the samples, the features are the pixel intensities, and the target outcome is a binary prediction that indicates the presence or absence of lung cancer.

In medical diagnosis, ML can be used to perform a classification task, in which input information is mapped to a target categorical prediction. In the diagnosis of a disease, the problem can be framed as a binary classification task, in which target information is mapped to a binary outcome (presence or absence of the disease). While this binary classification approach simplifies the diagnosis problem, it is a reasonable starting point for algorithmic diagnosis.

ML models learn an input-output relationship through training on a training dataset and the performance of a trained model can be evaluated using a previously unseen testing dataset. Testing aims to evaluate the ability of trained ML models to generalize (i.e., to determine the performance of the model on new data). Appropriate training methods are necessary to ensure model generalization. If a model performs poorly on new data but performs well on the training data, the model is described as having overfit on the training data (indicating an input-output relationship has been learned, but this relationship is specific to the individual samples in the training dataset). Underfitting occurs when a model performs poorly on both the training and testing sets. Overfitting is often a concern, particularly with small datasets, and appropriate methods for evaluating the generalizability of ML models must be carefully selected.

1.4.2 Machine Learning in BMS

ML investigations in BMS have primarily focused on classifying tumor responses as benign or malignant [80–83]. Applications of ML methods have relied on simulated data [83–85], small-scale experimental datasets (one phantom in [86], one cylindrical phantom in [80–82]), small-scale experimental datasets with simulated tumor-responses injected into the data [87], or small-scale

experimental datasets using nonphysical phantom materials (ex: three metal spheres used to represent tumors in [88]). One article presented results on data from 18 patient scans [89] and reported promising accuracy of 98.55% with a support vector machine, but the limited description of the ML methods in [89] prohibit replication. Additionally, the training procedures used in [89] allowed for data contamination, limiting the ability of their evaluation methods to accurately evaluate the generalizability of the model.

The feasibility of differentiating benign and tumor tissues has been demonstrated [80–82], but a thorough analysis of the feasibility of ML for tumor-detection using a large experimental dataset has not yet been published in the literature.

This thesis presents an investigation into the potential diagnostic capability of machine learning methods in breast microwave sensing using a large-scale (over 1000 unique experimental phantom scans) open-access dataset [44].

1.5 Problem Definition

1.5.1 Problem Statement

Breast microwave sensing is a promising modality that could be used as a breast cancer screening tool [11, 13, 14]. Microwave-based systems have the potential to be non-ionizing and low-cost tools for cancer detection. Despite the rapid transition from simulation [10] to phantom-based experiments [71] to patient studies [19], there are several challenges remaining before these systems are ready for clinical use. Small-scale independent investigations have limited the depth of analysis that has been performed, robust image reconstruction techniques have not been developed or evaluated using diverse and controlled experiments, and tumor-detection techniques have yet to be evaluated using large-scale experimental datasets.

1.5.2 Thesis Objectives

The main objective of this thesis is the development of a large-scale open-access dataset for the development and evaluation of novel radar-based image reconstruction techniques, and the evaluation of the diagnostic capability of machine learning methods for tumor-detection in breast microwave sensing. This work addresses three of the major challenges in BMS today: the lack of large-scale controlled phantom experiments and open-access datasets (Chapter 2), the lack of a robust image reconstruction technique (Chapter 3), and the lack of a large-scale experimental investigation into the viability of automated tumor-detection methods (Chapter 4).

2. Generation of an Open-Access Experimental Dataset

This chapter describes the development of an open-access experimental dataset for use in breast microwave sensing: the University of Manitoba Breast Microwave Imaging Dataset (UM-BMID). The motivation for constructing this dataset, the experimental system used to perform the scans, and the array of anthropomorphic 3D-printed MRI-derived breast phantoms that were scanned to produce the dataset are discussed. A preliminary application of machine learning for tumor detection in a subset of the dataset is presented, and the chapter concludes by describing the completed dataset. A portion of this chapter describes work presented in the publication [44].

2.1 Introduction

Early investigations in BMS used simulated results [10, 70] or simple experimental setups [71] to demonstrate the potential of using microwaves for breast cancer detection. The promising initial results prompted several research groups to develop more realistic experiments using breast phantoms and more advanced imaging systems [17, 20, 34, 40, 43]. The first phantoms were cylindrical [71, 73] and did not accurately represent the morphology or dielectric properties of the breast tissues. Phantom development has progressed significantly since these early investigations - standard phantoms today more closely model both the morphology and dielectric properties of the breast tissues. Several independent research groups have developed phantoms that more accurately model the breast tissues [41, 46–48, 69, 90, 91].

Along with the advances in phantom design, groups have also developed BMS systems capable

of scanning patients [17–20, 34, 40, 43] and several patient investigations have been performed [19, 22, 24, 27, 34]. Despite the progress of imaging system and breast phantom development, much of the research in BMS still relies on simulation [83, 92–97]. While simulation allows for controlled evaluation and development of new methods, experimental validation is ultimately required, and results obtained in simulation can be challenging to realize in experiment.

Phantom studies can be used as a controlled experimental method for the evaluation of algorithms and methods in BMS. While several patient studies have been performed [19, 21–35], the difficulties presented in interpreting patient results (due to incomplete knowledge of the true dielectric properties of the breast and their distribution within the breast and image-registration challenges) and the numerous challenges present in BMS (ex: image reconstruction, permittivity estimation, skin suppression methods, image quality analysis), patient studies may be premature.

Large-scale phantom experiments are necessary to evaluate methods in BMS under controlled conditions. Only after a method is found to be viable in phantom experiments can it be reasonably applied to patient data. Other factors that have yet to be investigated, but are hypothesized to affect the performance of BMS systems (ex: breast density, breast size, tumor size, and tumor position), should first be examined under controlled experimental conditions before large clinical trials are performed.

Another challenge facing BMS research is the lack of open-access data and open-source analysis in the literature (notably, [98] presents an open-source implementation of common image reconstruction algorithms, but this is the only open-source work described in the literature to-date). This limits the reproducibility and transparency of research in the field. While data from phantom and patient scans have been shared among individual research groups [35, 99], none of the datasets presented in the literature to-date are open-access. This has resulted in the presence of data silos in BMS research, in which individual groups generally operate independently rather than cooperatively or collaboratively. The field is broadly concerned with the development of microwave-based diagnostic methods in healthcare, and the presence of data silos and lack of community trans-

parency and reproducibility are detrimental to the overall goals of the research community.

To address the challenges of closed-source analysis methods, closed-access datasets, and prevalence of simulation-based investigations in BMS, we have created an open-access dataset, the University of Manitoba Breast Microwave Imaging Dataset (UM-BMID). This dataset contains data from scans of 3D-printed MRI-derived breast phantoms performed using a pre-clinical BMS system, the 3D-printable .stl files used to create the phantoms, and metadata describing the individual scans. The dataset is open-access and is available at `https://bit.ly/UM-bmid` and use of this dataset by the broader research community is encouraged. To promote transparency and reproducibility, all code used to produce the ready-to-use .pickle (for use in Python) and .mat (for use in Matlab and Octave) files and the .py files used to perform the analysis presented in this chapter are available at `https://github.com/UManitoba-BMS/UM-BMID`.

2.2 Methods

2.2.1 3D-Printed MRI-Derived Breast Phantoms

Phantoms allow for controlled experimentation - a necessary tool in the development and evaluation of methods in BMS. Three primary phantom designs have been used in the literature: solid phantoms [46,47], liquid phantoms [40,45,48,100], and gel phantoms [101–103]. Solid phantoms use solid materials as the tissue-mimicking materials and are both mechanically robust and stable over long periods of time. These phantoms can be 3D-printed [47], facilitating reproduction, but these phantoms also have limitations due to their solid fabrication - a solid phantom has only one tissue geometry, and no modifications can be made due to the solid components. Tumor analogs must be a permanent component of solid phantoms, limiting the ability to compare healthy-breast phantoms and cancerous phantoms of the same tissue geometry. This limitation could be addressed through the construction of many phantoms of the same tissue geometry, but a new phantom must be developed for each new tissue geometry. This restricts the use of solid phantoms for large-scale

analysis.

Gel-based materials can closely model the dielectric properties of breast tissues [102, 103], but are not mechanically robust. These phantoms must be prepared individually by hand and are therefore individually unique. This limits reproducibility of the phantoms and the level of control attainable in experiments using gel-based phantoms, as the exact distribution of dielectric properties is unknown. The use of gel materials allows for repositioning of tumor analogs within the phantoms, which is advantageous for investigating the effects of tumor position and size on algorithms in BMS. However, the lack of control over the healthy tissue distributions within phantoms, and the need to produce a new phantom for each unique healthy-tissue geometry prohibit the use of gel-based phantoms for large-scale experimentation in BMS.

Liquid-based phantoms use liquids as the tissue-mimicking materials and use shells to contain these liquids. The initial liquid-based phantoms used cylindrical [73] or hemispherical shells [40] made of low-permittivity plastics. Recent phantom development has used 3D-printing technology to produce printed shells that are derived from MRI images of patients [45, 48, 100]. These 3D-printed MRI-derived liquid-based phantoms mimic the *in vivo* tissue morphology, and liquids that mimic the reported dielectric properties of breast tissues can be used with these phantoms. While these phantoms require the use of low-permittivity plastic (a cost absent in solid- and gel-based phantoms), they are unique in their ability to model both the morphology and dielectric properties of breast tissues. These phantoms have typically been produced using a two-shell model, in which an adipose shell and a fibroglandular shell are printed separately and combined when in-use. This allows for the use of many unique adipose-fibroglandular shell combinations with a small number of 3D-printed shells. Tumor analogs can also be freely inserted into liquid-based phantoms. The use of 3D-printed shells also enhances the reproducibility of these phantoms, as the .stl files used to produce the phantoms can be shared. The .stl files can be readily used with any suitable 3D-printer to reproduce the phantoms. Liquid-based phantoms are currently most well-suited for large-scale experiments due to the reproducibility of the individual phantoms, freedom of tumor positioning, and ability to produce a large number of unique phantoms from a relatively small

number of individual shells.

Our laboratory has developed two generations of 3D-printed MRI-derived breast phantoms. These phantoms are derived from the repository of numerical phantoms developed from MRI scans of nine patients provided by the University of Wisconsin-Madison [47].

The prototype from the first generation was initially presented in [45] and a selection of the phantoms from this generation have been used in past studies [36, 37]. The first generation array is displayed in Fig. 2.1 and consists of three adipose shells (labeled A1 through A3) and five fibroglandular shells (labeled F1 through F5). When in use, an adipose shell is combined with a fibroglandular shell. The phantom ID is defined as a combination of adipose and fibroglandular shell labels (ex: A1F1 corresponds to the phantom constructed using the A1 adipose shell and F1 fibroglandular shell). These hollow shells are then filled with liquids selected to mimic the dielectric properties of breast tissues. Glycerin was used as the adipose-tissue surrogate, a 30% solution of Triton X-100 was used as the fibroglandular surrogate, and saline solution was used as the tumor-mimicking liquid. The dielectric properties of these materials are described in [45].

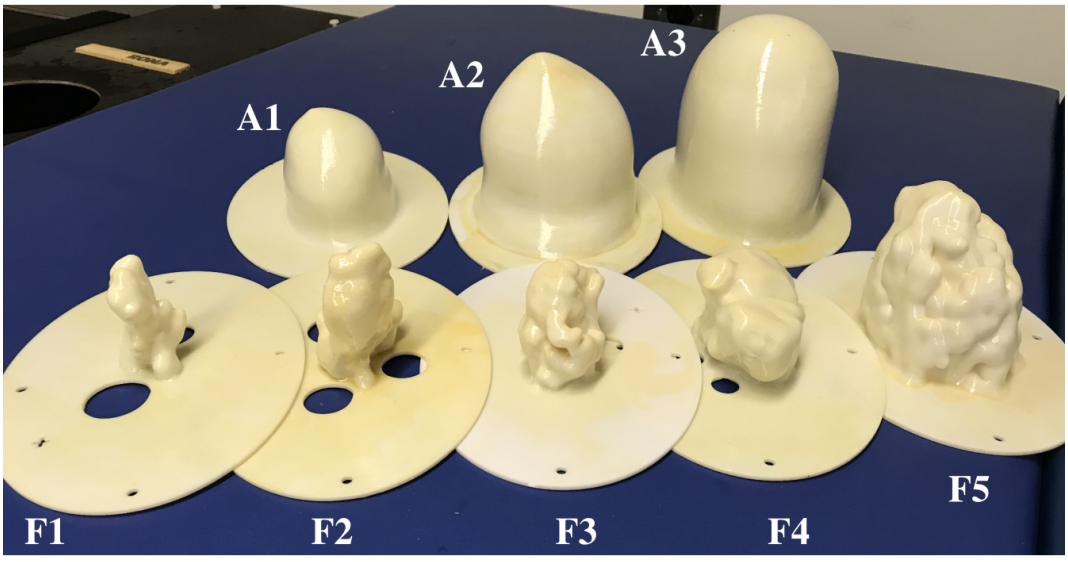


Figure 2.1: First generation of 3D-printed MRI-derived breast phantoms. Adipose shells labeled A1 through A3, fibroglandular shells labeled F1 through F5.

Thirteen unique adipose-fibroglandular shell combinations can be constructed using the first generation phantoms, allowing for a diverse array of phantoms that are representative of all four

BI-RADS breast density classification categories [5]. Physical size constraints prevent all five fibroglandular shells being used with all three adipose shells (ex: shell F5 does not physically fit within shell A1). The first generation phantoms were printed with polycarbonate using a Fortus 400mc printer (Stratasys Inc., Eden Prairie, USA). The phantom shells were observed to allow the diffusion of liquids across the shell material, and an oil-based polyurethane coating was applied to the shells to prevent such diffusion [45].

Spherical glass bulbs were used as the shells containing the tumor-mimicking liquid. These bulbs were created by a glass blower and are displayed in Fig. 2.2.

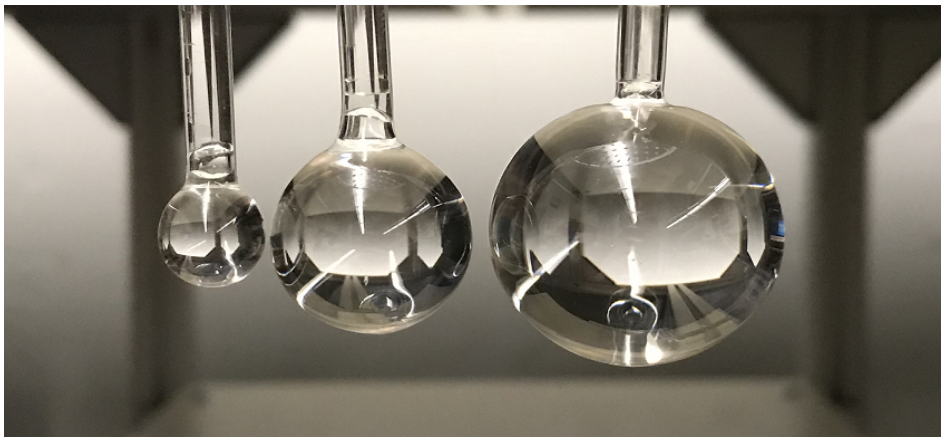


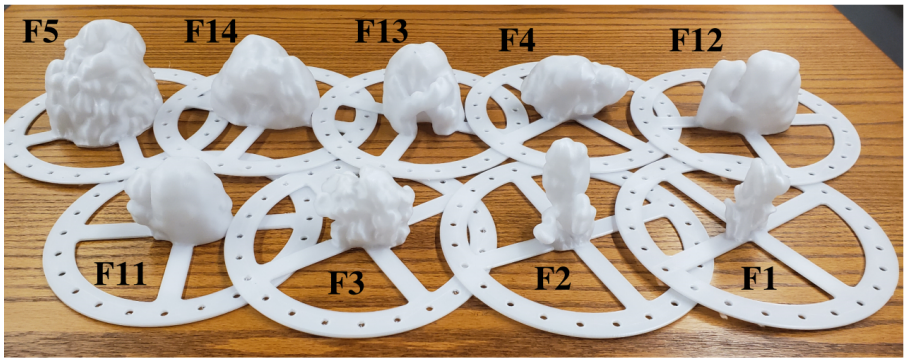
Figure 2.2: Glass bulbs (filled with saline solution) used to model tumors. 0.5 cm radius tumor shown at left, 1.0 cm radius tumor shown in the middle, and 1.5 cm radius tumor shown at right.

A second generation of 3D-printed phantoms was developed to address some of the challenges observed when using the first generation phantoms and to expand the phantom array. A photograph of the second generation of phantoms is displayed in Fig. 2.3.

The bases of the fibroglandular shells of the second generation phantoms were modified to allow for greater freedom tumor analog positioning (in the first generation phantoms, the circular holes in the shell bases were designed to be used as sites for tumor insertion). These bases were also modified to allow for consistent positioning of the fibroglandular shells at 24 rotational positions. Two pegs on the bases of the adipose shells can be inserted into two of the 24 holes in the fibroglandular shell base, allowing for reproducible and fixed-positioning of the phantoms at



(a)



(b)

Figure 2.3: Second generation of 3D-printed MRI-derived breast phantoms. (a) Adipose shells labeled A1 through A3 and A11 through A16, (b) fibroglandular shells labeled F1 through F5 and F11 through F14.

24 rotational positions.

66 unique adipose-fibroglandular shell combinations can be constructed using the second generation phantoms. Table 2.1 displays some of the geometry parameters of the phantoms contained within the second generation.

Table 2.1: Second Generation Phantom Properties

	Minimum Value	Maximum Value
Adipose shell volume	294.7 cm^3	1113.3 cm^3
Fibroglandular shell volume	12.8 cm^3	275.6 cm^3
Breast density (fibroglandular %)	1.15%	38.25%
Adipose shell diameter	12.0 cm	16.3 cm
Chest-to-nipple length	7.76 cm	13.82 cm

The second-generation phantoms were printed using a Prusa i3 MK3 3D-printer and were printed using polycarbonate copolyester. The shells printed with this material were observed to be watertight and did not require a coating.

2.2.2 Pre-Clinical Breast Microwave Imaging System

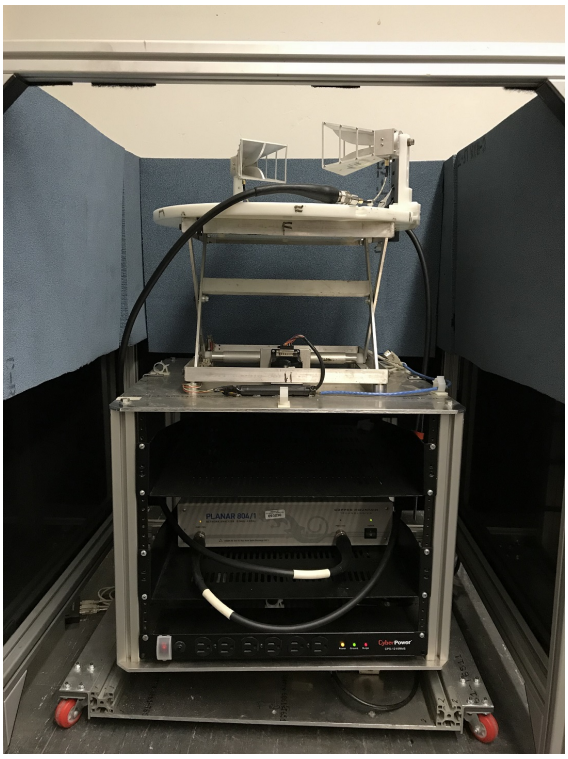
A pre-clinical rotating radar-based breast microwave imaging system [17] was used to perform the phantom scans that comprise UM-BMID. A photograph of this system is displayed in Fig. 2.4. The imaging system operates using a vector network analyzer (VNA) (Planar 804/1, Copper Mountain Technologies, Indianapolis, IN, USA) to supply a stepped-frequency continuous-wave signal at 1001 frequency points over 1-8 GHz to a double-ridged horn antenna (LB-20200-SF, A-INFO, Chengdu, China). The system operates in air, without the use of a coupling medium. To-date, our group is one of only two that have published in the literature that do not require a coupling medium or gel or contact between the antennas and the breast tissues [17, 43].

The system can operate in monostatic (one antenna) or bistatic (two antennas) scan configurations. The VNA measures the S_{11} scattering parameters in the monostatic configuration and measures the S_{11} and S_{21} scattering parameters in the bistatic scan configuration. The antennas are attached to a platform, shown in Fig. 2.4 (b), and are rotated to 72 positions along a circular trajectory during a scan. The S-parameters are measured at each of these 72 positions. During bistatic operation, the two antennas are separated by 60°. The radius of the antenna trajectory can be adjusted based on the size of the breast. For all scans performed in UM-BMID, the antenna radius was between 20 cm and 23 cm.

While the system is capable of performing measurements with the antennas at multiple heights, all scans performed in this work used only one antenna height. Despite performing measurements at only one height, the measurements capture 3D-responses due to the beamwidth of the antennas. At the central scan frequency, the 3 dB beamwidth of the antenna is 41.4°, corresponding to a vertical distance of 15.1 cm at the center of the scan region, assuming the antennas are positioned



(a)



(b)

Figure 2.4: Radar-based breast microwave sensing system developed in our laboratory; (a) displays the top of the bed system and (b) displays the radar module.

with a 20 cm scan radius. 3D responses from the phantoms are therefore measured by the antennas, even for a single antenna height.

2.2.3 Experimental Scan Procedure and Dataset Generation

Scans of both generation-one and generation-two phantoms are included in the dataset. Scans of the first generation of phantoms were performed first and prompted the development of the second generation of phantoms. In the scans of each phantom generation, the scans were performed so that half of all scans were of healthy phantoms (no tumor analog included in the scan), and half were of scans of phantoms containing a tumor surrogate. Within these healthy and cancerous scans, the scans were performed so that an approximately uniform distribution over BI-RADS breast density class [5] was obtained, and within the cancerous scans, an approximately uniform

distribution across the three tumor sizes was obtained. This was done so that the effects of these factors (breast density and tumor size) could be analyzed in future work.

The scans of the second generation of phantoms were performed so that no two scans were identical with respect to the following combination of metadata:

- Breast phantom ID
- Adipose shell $(x,\ y)$ translation within the imaging chamber
- Fibroglandular shell $(x,\ y)$ translation within the adipose shell
- Fibroglandular shell rotation with respect to the adipose shell
- Tumor size
- Tumor $(x,\ y)$ position

No two scans performed using the second generation of phantoms had an identical set of the above metadata.

Reference scans are required to perform meaningful analysis of phantom scans. Empty-chamber reference scans can be used to remove reflections from the imaging system chamber and system components (i.e., reflections due to the antennas, cable connections, etc.). All scans in UM-BMID have an accompanying empty-chamber reference scan to facilitate this calibration. For all tumor-containing scans of the second generation phantoms, a scan of an adipose-only phantom (fibroglandular and tumor components removed) was also performed. This was done to facilitate comparisons of image reconstruction techniques in such a way so as to be agnostic to the choice of skin suppression method. Image reconstruction analyses typically require a skin suppression algorithm to remove the skin reflections. To compare different image reconstruction techniques in a way that is agnostic to the choice of skin suppression method, a healthy phantom scan is required.

Scans of the first generation of phantoms were performed using a monostatic scan configuration and the S_{11} scattering parameters were measured in these scans. A bistatic configuration was used

for all scans of the second generation phantoms and the S_{11} and S_{21} scattering parameters were measured in these scans.

2.2.4 Initial Machine Learning Methods

To demonstrate a potential use of UM-BMID, a logistic regression classifier was used to predict the presence of a tumor in scans obtained using the scan data obtained with the first generation of phantoms. The individual scans were defined as the samples in the machine learning model and a binary classification approach was used to predict the presence of a tumor within the phantom from the scan. The binary class label was defined as the presence of a tumor within the phantom during the scan. The samples were described using the magnitude of the time-domain S_{11} parameters, obtained via the inverse discrete Fourier transform. A time-window was applied to discard responses that did not occur in the region of interest, cropping the time-domain signals to remove all responses that occurred before 0.71 ns or after 5.71 ns. These bounds were empirically selected to contain the responses that occurred within the breast tissues. Each sample was therefore described using 35×72 features, corresponding to 35 time-domain responses at each of the 72 antenna positions used in the scan.

The 249 samples that comprise the first-generation dataset were randomly split into training and testing sets. 50 samples were assigned to the testing set. This random sorting was subject to the following constraints: the test set was required to have approximately uniform distributions of breast density class, class label, and tumor size. These conditions were imposed to ensure the test set was representative of the overall dataset.

A custom implementation of a logistic regression classifier was used. This was done to facilitate transparency in the initial publication presenting the dataset [44], and the code used in the implementation (available in Python and Matlab/Octave) is available at `https://github.com/UManitoba-BMS/UM-BMID`.

The logistic regression classifier was trained using gradient descent with the learning rate set

to 1. While more sophisticated optimization functions could have been used, gradient descent was selected for this analysis due to its simplicity, and to demonstrate a potential first-use of UM-BMID. The stopping iteration was determined using a grid-search over the set $\{10^1, 10^2, 10^3, 10^4, 10^5, 10^6\}$. The optimal stopping iteration was defined as the largest number of iterations during training that did not result in 100% classification accuracy on the training set, which would have indicated that the model had overfit on the training set.

Four metrics were used to evaluate the performance of the classifier on the test set. The diagnostic accuracy was defined as

$$\text{Diagnostic Accuracy} = \frac{tp+tn}{tp+tn+fp+fn}, \tag{2.1}$$

where tp is the number of true-positive predictions, tn is the number of true-negative predictions, fn is the number of false-negatives, and fp is the number of false-positives. The sensitivity was defined as

$$\text{Sensitivity} = \frac{tp}{tp+fn}. \tag{2.2}$$

The specificity was defined as

$$\text{Specificity} = \frac{tn}{tn+fp}. \tag{2.3}$$

The fourth metric used to evaluate the performance of the classifier was the area-under-the-curve of the receiver operating characteristic curve (ROC AUC).

2.3 Results and Discussion

2.3.1 UM-BMID: The University of Manitoba Breast Microwave Imaging Dataset

UM-BMID contains data from over 1250 scans of breast phantoms. Excluding reference scans, there are 249 scans of generation-one phantoms and 1008 scans of generation-two phantoms. The complete dataset is available at `https://bit.ly/UM-bmid`, and the code used to produce the analysis in this chapter is available at `https://github.com/UManitoba-BMS/UM-BMID`.

The .stl files used to produce the 3D-printed phantoms (both generations) are also available at `https://bit.ly/UM-bmid` to facilitate reproducibility. These phantoms are available for any research group to utilize and can be printed using desktop 3D-printers.

2.3.2 Initial Machine Learning Analysis for Tumor Detection in UM-BMID

The optimal stopping iteration was determined to be 10^5 iterations using 5-fold grid search cross-validation. Fig. 2.5 displays the average classification performance metrics on the test set over 10 runs and the reported uncertainties are the standard deviations across the 10 runs. The results obtained on the first generation scans in UM-BMID are compared to the results obtained using a support vector machine with radial basis function (SVM RBF) in a 2019 2D-simulation study [84].

The ROC AUC and diagnostic accuracy results obtained in this investigation are in agreement with those obtained in [84]. This demonstrates the feasibility of using ML methods for automated tumor-detection in BMS.

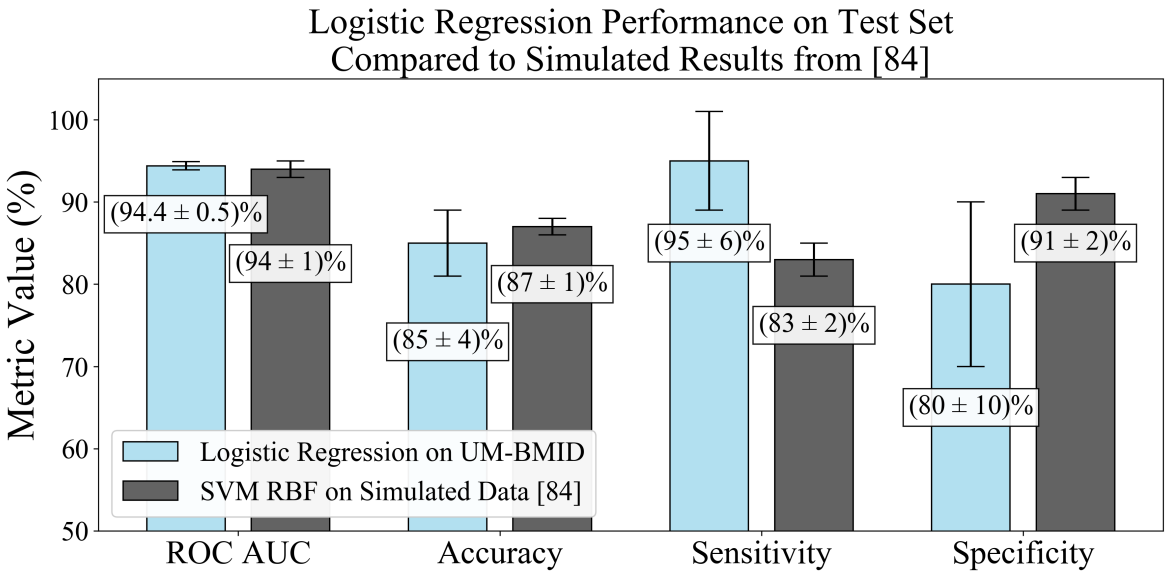


Figure 2.5: Classification performance obtained by logistic regression classifier on generation one scans in UM-BMID compared to performance obtained by SVM RBF on simulated data from [84]. Figure modified from [44].

2.4 Conclusions

The largest dataset presented in the published literature to-date has been developed - the University of Manitoba Breast Microwave Imaging Dataset (UM-BMID) is also the first open-access dataset in BMS. While the dataset has limitations (ex: only one antenna vertical position and the presence of low-permittivity plastics in phantoms), this work presents the first opportunity to perform relatively large-scale analyses (over 1250 scans) using controlled phantom experiments with extensive metadata. Specifically, machine learning analyses benefit from large datasets, and this dataset could serve as a standard in ML applications in BMS. The diversity of the dataset allows for analyses into the effects of breast size, breast density, tumor size, tumor position, and other phantom factors on the performance of image reconstruction and tumor-detection methods in BMS.

UM-BMID is available at `https://bit.ly/UM-bmid`. This repository contains the frequency-domain scattering parameter measurements from the individual phantom scans, metadata for each

scan, the 3D-printable .stl files used to produce the MRI-derived phantoms, and documentation regarding scan procedure and metadata. Further documentation is also available at `https://github.com/UManitoba-BMS/UM-BMID`.

This dataset is used in Chapters 3 & 4 in this thesis. While the diagnostic accuracy of $(85 \pm 4)\%$ obtained in this chapter demonstrates the feasibility of using machine learning methods for automatic tumor detection with the time-domain S-parameters, a more rigorous investigation is warranted. This preliminary ML analysis demonstrates the feasibility of using classification algorithms for tumor detection in BMS and a thorough investigation is presented in Chapter 4. This chapter describes UM-BMID, the dataset that is investigated in greater depth for image reconstruction and further machine learning applications in Chapters 3 & 4.

3. Improving Signal Processing and Image Reconstruction Methods

This chapter compares the effects of two methods of frequency-to-time domain conversion on radar-based image reconstruction using a standard beamformer. An investigation into the optimal time-step size used to represent the time-domain radar signals, with respect to optimizing image quality, is described. A portion of this work was presented in the articles [104, 105]. This chapter also describes a novel image reconstruction algorithm for use in radar-based breast microwave imaging: the iterative delay-and-sum (itDAS) beamformer. Reconstructed images of scans of MRI-derived phantoms in an air-based BMS system produced by the itDAS beamformer are compared to those obtained with the standard delay-and-sum and delay-multiply-and-sum methods. A second algorithm, the iterative delay-multiply-and-sum (itDMAS) algorithm is also presented. The implementation of three correction factors into the forward model of the itDAS algorithm is presented and the effects of the correction factors on reconstructions are discussed.

3.1 Introduction to Image Reconstruction in Breast Microwave Imaging

In radar-based image reconstruction the delay-and-sum (DAS) and delay-multiply-and-sum (DMAS) beamformers are literature standards and have been used as standards-of-comparison for novel beamformers [42]. While alternative beamformers have been developed, including the improved delay-and-sum [40], the coherence-factor based delay-and-sum [41], and the channel-ranked delay-and-sum [39] methods, recent investigations on phantom [42] and patient [35] data

indicate that only DMAS reduces both high- and low-intensity clutter while accurately localizing the tumor response.

Despite the breadth of work in radar-based BMS [14], no reconstruction algorithm other than the DMAS beamformer [38], which was developed in 2008, has been demonstrated to provide consistent improvements over the DAS method [35, 42]. The DAS beamformer and its derivatives have been used in many patient studies [19, 21–33], but the DAS beamformer is not without its limitations. DAS reconstructions can have a low contrast between the tumor and fibroglandular responses, particularly in dense breasts, and the DAS beamformer neglects much of the physics of microwave imaging. The DAS beamformer assumes a homogeneous propagation speed in the scan region, neglects signal attenuation, and ignores antenna and system-specific parameters. These components of the physics model are all expected to affect image reconstruction. While DMAS improves image contrast, it does not model additional physics components, and there is no physical justification for the pair-wise signal multiplication in DMAS (this pair-wise multiplication is the only difference between DMAS and DAS, as shown in Eq. 1.3 and Eq. 1.5).

This work proposes a novel image reconstruction technique that adapts the iterative functional form of the MLEM algorithm from PET for use in radar-based BMS. This iterative reconstruction algorithm allows for the implementation of correction factors into the signal model, building upon the straight forward DAS beamformer and incorporating more complex physics components. The effects of three correction factors on image reconstruction are explored. These corrections model the antenna's beam pattern, the antenna's frequency-dependent gain, and the output pulse of the VNA used to perform the S-parameter measurements.

This chapter also presents an investigation of the effects of the choice of time-step size used to represent the time-domain radar signals on image reconstruction using the DMAS beamformer. The DAS beamformer and its derivatives require time-domain radar signals, and systems that perform measurements with a VNA require a method for frequency-to-time domain conversion. The inverse discrete Fourier transform and the inverse chirp z-transform can be used for this transfor-

mation. The inverse discrete Fourier transform produces time domain signals with a fixed time-step size, while the inverse chirp z-transform allows for an arbitrarily-small time-step size. The effect of these two methods and the choice of time-step size on image quality are examined herein.

3.2 Methods

3.2.1 Literature Standard Beamformers

The delay-and-sum (DAS) beamformer is the standard method in the published literature for radar-based image reconstruction [10,19,35,42,71]. Several derivative algorithms have been developed using modifications to the signal model of the DAS beamformer [38–41]. These alternative beamformers have been designed to reward signal coherence and to increase contrast between the tumor response and clutter in the image.

The DAS beamformer is described in Eq. 1.3 and is used as a standard method for comparison purposes in this chapter. The DMAS beamformer (described in Eq. 1.5) is also used as a standard method in this chapter. DMAS was selected over alternative methods due to its performance in phantom [42] and patient [35] studies, in which six beamformers were compared (DAS, DMAS, improved delay-and-sum [40], channel-ranked delay-and-sum [39], coherence-factor delay-and-sum [41], and the robust capon beamformer [77]). The results in both studies demonstrated that only DMAS reduced both background and high-intensity clutter and accurately localized the tumor responses, relative to DAS [35, 42].

3.2.2 Propagation Speed Estimation and Skin Suppression

The average estimated propagation speed was used to determine the time-delays used for the summation of the radar signals in all image reconstruction methods presented herein, as in Eq. 1.3 and Eq. 1.5. The permittivity in the phantom was assumed to be that of the adipose tissue-

mimicking material at the central scan frequency (4.5 GHz), $\varepsilon_r' = 6.4$ [45]. The estimated average propagation speed was calculated using a 2D geometric model, assuming a circular scan region and a circular homogeneous breast phantom. While accurate permittivity estimation is an active area of work [31, 69, 106], this relatively straightforward approach of using an average estimate allows for the direct comparison of image reconstruction methods and has been used in other works comparing reconstruction methods [35, 38, 40, 76].

Large reflections occur at the exterior skin interface in BMS systems. These reflections can obscure the responses from the inner tissue structures [86, 96, 107–110], obfuscating the tumor and fibroglandular tissue responses in reconstructed images. Several groups have developed imaging systems that use coupling media to reduce the contrast at the exterior skin interface [18–21] but skin-response suppression techniques are still required to sufficiently remove the skin response. In air-operated systems [17, 43], a large contrast persists at the exterior skin interface.

While the phantoms in this work do not have a skin-mimicking material, the air-plastic interface that occurs at the exterior of the 3D-printed adipose shells produces large reflections that obscure the inner tissue responses. Despite the low-permittivity plastic, a theoretical analysis performed in [43] demonstrated that the reflections observed at an air-PLA plastic interface are similar to those obtained at an air-skin interface. The work in [43] compared the reflections at the air-PLA plastic interface to those of an air-skin interface, comparing two skin thicknesses of 0.7 mm and 2.5 mm (selected as representative of minimum and maximum expected breast skin thicknesses [111]). The theoretical analysis compared the reflections of an air-PLA-fat-fibroglandular transmission line model to that of an air-skin-fat-fibroglandular model, using a 1.2 mm PLA thickness [43] and tissue properties taken from tissue measurements [112]. The authors concluded that the reflected power from the air-PLA interface was between the power reflected from the two (0.7 mm thick and 2.5 mm thick) skin interfaces, indicating that low-permittivity plastics may be suitable for use as a skin-mimicking material in air-based BMS systems.

In this work, ideal skin suppression was performed to remove the exterior air-tissue reflections.

This was done to allow a direct comparison of the performance of reconstruction algorithms that is agnostic to the choice of practical skin suppression method. This ideal suppression was implemented by performing two scans of the phantom. The first scan was performed with all phantom tissue components and the second scan was performed after removing the inner tissue components, leaving only the adipose-mimicking material. The difference between these two scans was used as the calibrated dataset.

3.2.3 Frequency-to-Time Domain Conversion

BMS systems that use a VNA perform measurements in the frequency-domain (FD). The image reconstruction techniques in radar-based BMS, including the DAS and its derivatives, perform image reconstruction using the time-domain (TD) representation of the measured radar signals [10]. This requires a method for converting the measured FD signals to the TD prior to image reconstruction. This is done using the Fourier transform, but two numerical implementations have been used for this FD-to-TD conversion.

The inverse discrete Fourier transform (IDFT) is the standard numerical implementation of the inverse Fourier transform, and is used to convert a frequency-domain signal $\mathbf{S}(k)$, defined over $k = 0,\ 1,\ ...,\ K-1$ to a time domain signal $\mathbf{s}(n)$ defined over $n = 0,\ 1,\ ...,\ N-1$ (with $N = K$),

$$\mathbf{s}(n) = \frac{1}{K} \sum_{k=0}^{K-1} \mathbf{S}(k) \exp\left(\frac{j2\pi kn}{K}\right). \tag{3.1}$$

This method produces a TD signal $\mathbf{s}(n)$ with time step-size $\Delta t = \frac{1}{F_{span}}$, where F_{span} is the bandwidth of the FD signal [113]. The resulting time-step size after FD-to-TD conversion with the IDFT for a FD signal measured with the BMS system used in this work [17] (operating over 1-8 GHz) is $\Delta t \approx 0.143$ ns. In air, this corresponds to a distance step-size of approximately 43 mm.

The IDFT is a special case of the z-transform, evaluated at values of z evenly-spaced along the unit circle in the complex z-plane. The inverse chirp z-transform (ICZT) is another special case of

the z-transform, and can be evaluated at any point in the complex z-plane in general, but can also be used for FD-to-TD conversion if evaluated along an arc on the unit circle. In this special case, the ICZT is defined, within a scaling factor, as

$$\mathbf{s}(n) = \frac{1}{K} \sum_{k=0}^{K-1} \mathbf{S}(k) \exp\Big(j\theta_0 k\Big) \exp\Big(j\phi_0 kn\Big), \tag{3.2}$$

where the parameters θ_0 and ϕ_0 allow for the selection of the time-span of the signal $\mathbf{s}(n)$ and $n = 0, 1, \ldots, L-1$, where L can be selected as an arbitrary integer. The ICZT produces a TD signal $\mathbf{s}(n)$, represented by L points along the arc starting at angle $\omega_i = \theta_0$ and ending at the angle $\omega_f = (L-1)\phi_0 + \theta_0$. These angles ω_i and ω_f can be converted to time values t_i, t_f that describe the start and end points of the TD signal $\mathbf{s}(n)$ [113].

The ICZT allows for an arbitrarily-small time-step Δt used to represent the TD signal after FD-to-TD conversion (because of the parameter L), and allows for conversion to a specific time-span in the TD (because of the parameters θ_0 and ϕ_0). Fig. 3.1 displays sample measured radar signals from an experimental phantom scan with the system described herein, after FD-to-TD conversion via the IDFT and the ICZT.

In a stepped-frequency continuous-waveform system, a discrete measurement is made in the FD. In a TD radar system [20], a continuous signal is sampled and stored as a discrete TD signal. Just as the sampling frequency in a TD system determines the time-step size, the choice of the parameter L determines the step-size of the TD representation of the signal obtained using a FD system. As the sampling frequency becomes large, TD measurements approach the continuous representation of the signal, and as $L \to \infty$, so too does the $\mathbf{s}(n)$ signal obtained by the ICZT.

An analysis of the effects of the choice of time-step size Δt in FD-to-TD on image reconstruction using the standard DMAS beamformer was performed using two phantom scans. These two phantoms are from the first generation of phantoms in UM-BMID and were BI-RADS Class I (phantom ID: A2F1) and Class III (A1F3). This investigation was the first in the literature, to the best of our knowledge, to perform an examination of the effects of time step size on image

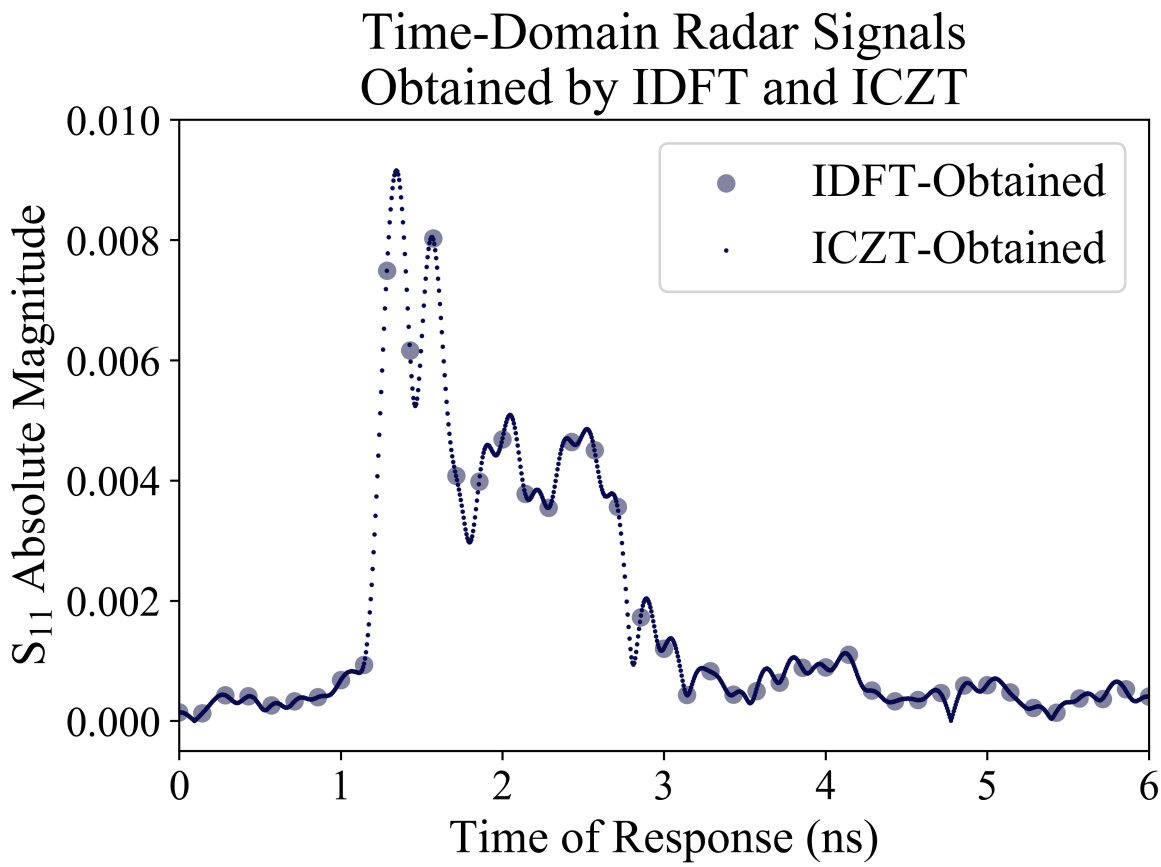


Figure 3.1: Time-domain radar signals obtained using the IDFT and ICZT (evaluated at 1024 points between 0 ns and 6 ns response times). Signals obtained from one antenna position from an experimental phantom scan. Figure adapted from [104].

reconstruction [104].

3.2.4 The itDAS Reconstruction Algorithm

The functional form of the maximum-likelihood expectation-maximization (MLEM) reconstruction algorithm from PET [79] was adapted for use in radar-based BMS. This functional form, with an additional normalization factor of $\hat{\mathbf{F}}[U]$ multiplying the measured dataset D, is

$$I^{n+1} = \frac{I^n}{\hat{\mathbf{B}}[U]}\hat{\mathbf{B}}\left[\frac{D\cdot\hat{\mathbf{F}}[U]}{\hat{\mathbf{F}}[I^n]}\right], \tag{3.3}$$

where I^n is the image estimate at the n^{th} iteration, $\hat{\mathbf{B}}$ is the back-projection operator, $\hat{\mathbf{F}}$ is the forward-projection operator, U is a unity matrix, and $\cdot$ indicates element-wise multiplication.

The forward operator was initially defined using a radar model,

$$\mathbf{s}_m(t) = \sum_{i=1}^{N} \sigma_i \delta(t - t_m(\mathbf{r}_i)). \tag{3.4}$$

This models the measured radar signal at the m^{th} position, $\mathbf{s}_m(t)$, as the sum of the responses from each pixel in the image-space. Each pixel is assumed to produce a point response weighted by the pixel's reflectivity σ.

The iterative delay-and-sum (itDAS) algorithm is defined using Eq. 3.3 as its functional form, Eq. 3.4 as its forward projection operator, and the delay-and-sum beamformer (as defined in Eq. 1.3) as its back-projection operator.

This iterative structure allows for any of the present DAS-derivatives to be used as the back-projection operator. One alternative choice was examined, in which the DMAS beamformer was used as the back-projection operator. This iterative DMAS-based algorithm was defined as the iterative delay-multiply-and-sum (itDMAS). The DMAS beamformer was selected for investigation due to its performance in two recent phantom [42] and patient [35] studies. These reports [35, 42] compared the reconstructions produced using DAS, DMAS, and four other reconstruction methods presented in the literature [39–41, 77] and found that only the DMAS beamformer reduced both background and high-intensity clutter while accurately localizing the tumor responses in reconstructions, compared to the DAS algorithm.

An implementation of the itDAS beamformer in Python is included in Appendix A.

3.2.5 Implementation of Correction Factors in the itDAS Algorithm

The itDAS beamformer allows for a choice of forward and back-projection operators. These operators can also be modified while retaining the iterative structure, allowing for the implemen-

tation of correction factors that improve the physics model. These correction factors could address challenges present when using the DAS or DMAS beamformers. These standard beamforming methods assume a radar model, and neglect signal attenuation, inhomogeneous propagation speed, the antenna's beam pattern and frequency-dependent gain, the output pulse-shape of the imaging system, and other path-dependent and system-specific effects. These factors could be incorporated into the forward and back-projection operators in Eq. 3.3.

This iterative structure also allows for the investigation of the effects of modeling individual physics components on the reconstructed images. In this work, the impacts of three correction factors were investigated. These correction factors were modeled in the forward projection operator $\hat{\mathbf{F}}$. The antennas beam pattern and frequency-dependent gain were present in all measurements but were not modeled in the forward projection model in Eq. 3.4. Both of these factors affected all measurements performed with the system and can be readily modeled and implemented into the forward operator. The VNA used in the system operated over a finite bandwidth and had its own frequency-dependent response that also affected all measurements. This frequency-dependence is mathematically equivalent to a time-domain output pulse and can be modeled in the forward projection operator.

The antennas beam pattern was implemented into the forward projection operator through a multiplicative factor $\beta(\phi_i)$ in Eq. 3.4,

$$\mathbf{s}_m(t) = \sum_{i=1}^{N} \beta(\phi_i)\sigma_i \delta(t - t_m(\mathbf{r}_i)). \tag{3.5}$$

The beam pattern of the antenna $\beta(\phi)$ is a function of the angle ϕ off the central axis of the antenna and is displayed in Fig. 3.2. A piece-wise quadratic function was used to model the beam pattern. The beam pattern for the antennas used in our system is described in the antenna documentation (LB-20200-SF, A-INFO, Chengdu, China). While the antenna has a beam pattern defined over the domain $-180^\circ \leq \theta \leq +180^\circ$, only responses in front of the antenna are of interest for the purposes of image reconstruction, and so the beam pattern model was developed over the

domain $-90^\circ \leq \theta \leq +90^\circ$.

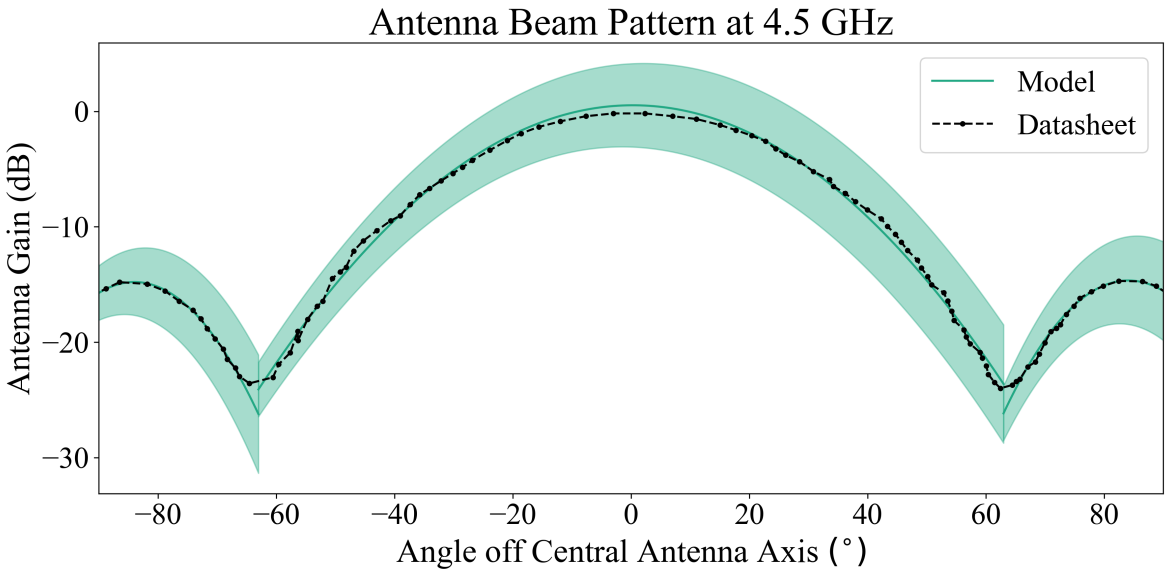


Figure 3.2: Antenna beam pattern model and data obtained from antenna datasheet. A piece-wise quadratic function was used to model the beam pattern. Shaded region indicates fit uncertainties.

The frequency-dependent gain of the antenna can be modeled as a function of frequency, $G(f)$, is also described in the antenna documentation, and can be incorporated into the forward signal model as,

$$\mathbf{s}_m(t) = \left[\sum_{i=1}^{N} \sigma_i \delta(t - t_m(\mathbf{r}_i)) \right] * g(t), \tag{3.6}$$

where $g(t)$ is the time-domain representation of the gain function $G(f)$ and $*$ denotes the convolution operator. The frequency-dependent gain of the antenna is displayed in Fig. 3.3. The antenna datasheet defined the antenna gain over the 2-20 GHz bandwidth, and because our system performs measurements from 1-8 GHz, the gain between 1-2 GHz was assumed to be equal to the gain at 2 GHz.

The output pulse of the VNA used in our system can also be modeled as a time-domain function $p(t)$, and can be incorporated into the signal model using

$$\mathbf{s}_m(t) = \sum_{i=1}^{N} \sigma_i p(t - t_m(\mathbf{r}_i)). \tag{3.7}$$

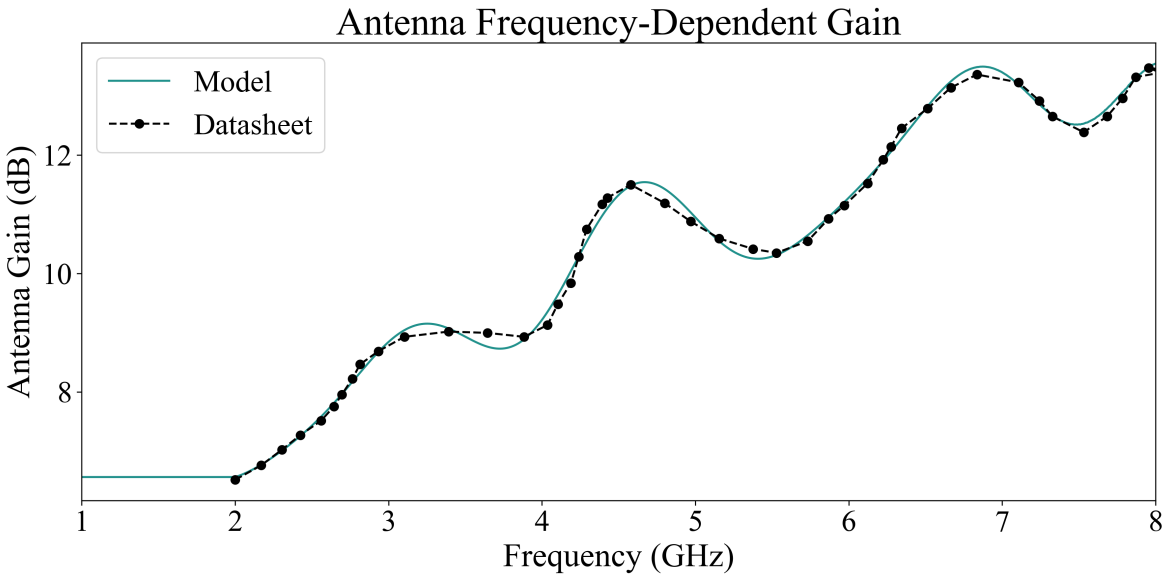


Figure 3.3: Antenna gain model and data obtained from antenna datasheet.

The output pulse of the VNA was measured by directly connecting the output and receiving ports of the VNA with a cable. The measured output pulse the Gaussian fit used to model the pulse are displayed in Fig. 3.4.

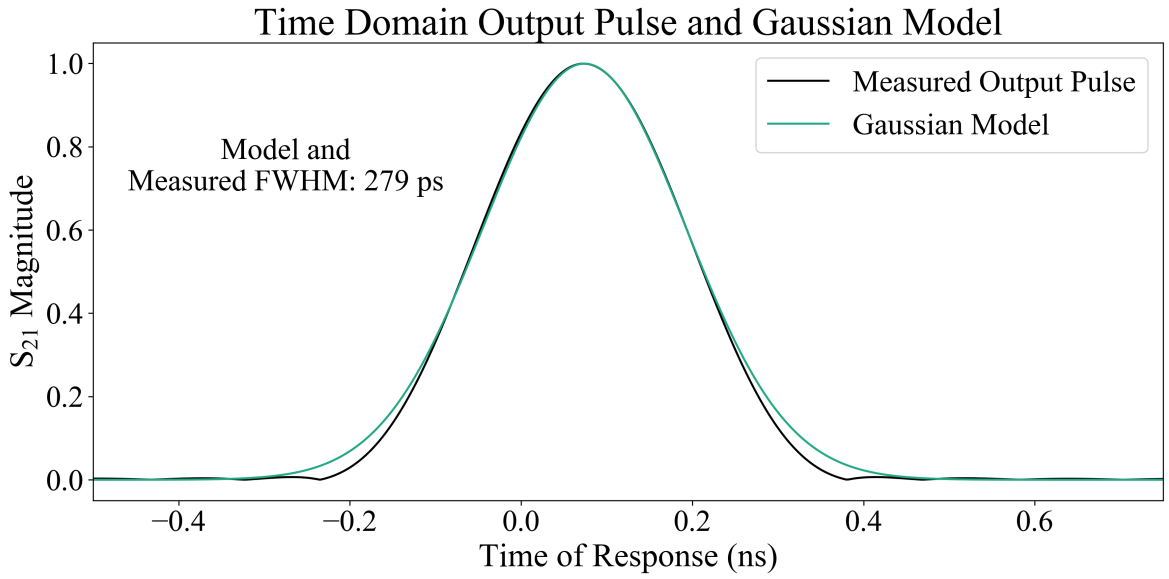


Figure 3.4: Measured VNA output pulse and Gaussian function used to model the output pulse. The variance of the Gaussian was extracted from measured S_{21} and used to model the Gaussian pulse function $p(t)$. The full-width at half-maximum (FWHM) of the model and the measured pulse are displayed.

These correction factors can be implemented individually into the forward signal model (as in Eq. 3.5, Eq. 3.6, and Eq. 3.7), or combined. This work examines the individual effects of these correction factors.

3.2.6 Selected Data for Image Reconstruction Analysis

A subset of the scans of the first generation of phantoms in UM-BMID was used to analyze the itDAS and itDMAS beamformers, and to compare them to their non-iterative counterparts. This subset consisted of scans of 9 unique phantoms, described in Table 3.1. Each phantom was scanned four times: once with a 15 mm radius tumor, once with a 10 mm radius tumor, once with a 5 mm radius tumor, and once without a tumor inclusion.

Table 3.1: Breast Density and BI-RADS Classifications of Phantoms Used in Beamformer Comparisons

	Fibroglandular Shell	Fibroglandular Volume	BI-RADS Classification
Small Adipose Shell (A1)	F1	4.4 %	Class II
	F3	19.9 %	Class III
	F4	37.2 %	Class IV
Medium Adipose Shell (A2)	F1	1.8 %	Class I
	F3	8.1 %	Class II
	F4	15.0 %	Class III
	F5	38.2 %	Class IV
Large Adipose Shell (A3)	F2	2.7 %	Class I
	F4	9.8 %	Class II

This subset was selected because it contains phantoms representative of each BI-RADS density classification category [5] and because these phantoms were the first that were scanned in UM-BMID.

3.2.7 Image Quality Metrics

No standard image quality metric is used throughout the literature in BMS, but most metrics aim to measure the contrast between the tumor response and clutter responses in the image. In radar-based image reconstruction in BMS, the image clutter is generally defined as the responses in the image that do not belong to the tumor. Clutter is primarily due to the presence of the fibroglandular tissues in the breast, due to their higher dielectric properties than adipose tissues [16, 112].

Three image quality metrics were used to quantitatively analyze the reconstructed images produced by each reconstruction algorithm. The signal-to-clutter ratio (SCR) is defined as

$$\mathrm{SCR} = 20\log_{10}\left(\frac{S_{max}}{C_{max}}\right), \tag{3.8}$$

where S_{max} is the maximum response in the known tumor region and C_{max} is the maximum response in the clutter region of the image. This is the same as the SCR defined in [114].

The signal-to-mean ratio (SMR) is defined as,

$$\mathrm{SMR} = 20\log_{10}\left(\frac{S_{max}}{C_{mean}}\right), \tag{3.9}$$

where C_{mean} is the mean response in the clutter region of the image. This definition is the same as in [114] and the same as the SCR definition in [37]. The uncertainty in C_{mean} was assumed to be zero, the uncertainty in S_{max} was defined to be the standard deviation of the intensity of the 75th percentile of pixels in the tumor region, and the uncertainty in C_{max} was defined to be the standard deviation of the intensity of the 95th percentile of pixels in the clutter region, as was done in [104]. The SMR and SCR provide a measure of the contrast between the tumor response and the clutter response in the reconstructed images.

The SCR can also be used as an objective metric for image-based tumor-detection. The SCR

compares the maximum response in the known tumor region to the maximum response in the clutter region of the image. A negative SCR therefore indicates that the maximum response in the image occurred outside the known tumor region, indicating that the tumor response is not identifiable in the image based on its intensity. While more sophisticated image-based tumor-detection criteria are necessary in BMS, the SCR can be used as a straight-forward criterion.

The localization error l was defined as

$$l = \left|\mathbf{r}_t - \mathbf{r}_{max}\right|, \tag{3.10}$$

where $\mathbf{r}_t$ is the known tumor position and $\mathbf{r}_{max}$ is the position of the maximum response in the reconstructed image.

3.3 Results

3.3.1 Effects of the ICZT on Frequency-to-Time Domain Conversion

The reconstructions of the two phantoms (A2F1 and A1F3, BI-RADS Class I and Class III, respectively) produced by the DMAS beamformer are displayed in Fig. 3.5, when produced using the IDFT for FD-to-TD conversion and when using the ICZT evaluated using a time step size of $\Delta t = 6$ ps.

The tumor response is prominent in both ICZT reconstructions, and in the IDFT reconstruction of the Class I phantom in Fig. 3.5, but is completely obfuscated by the clutter responses in the IDFT reconstruction of the Class III phantom in Fig. 3.5 (c). Prominent ring artifacts are also present in the images obtained after using the IDFT for FD-to-TD conversion but are absent in the ICZT-obtained images. While the ring artifacts do not completely obfuscate the tumor response in the Class I reconstruction in Fig. 3.5 (a), they do distort the tumor response compared to the ICZT-obtained reconstruction in Fig. 3.5 (b).

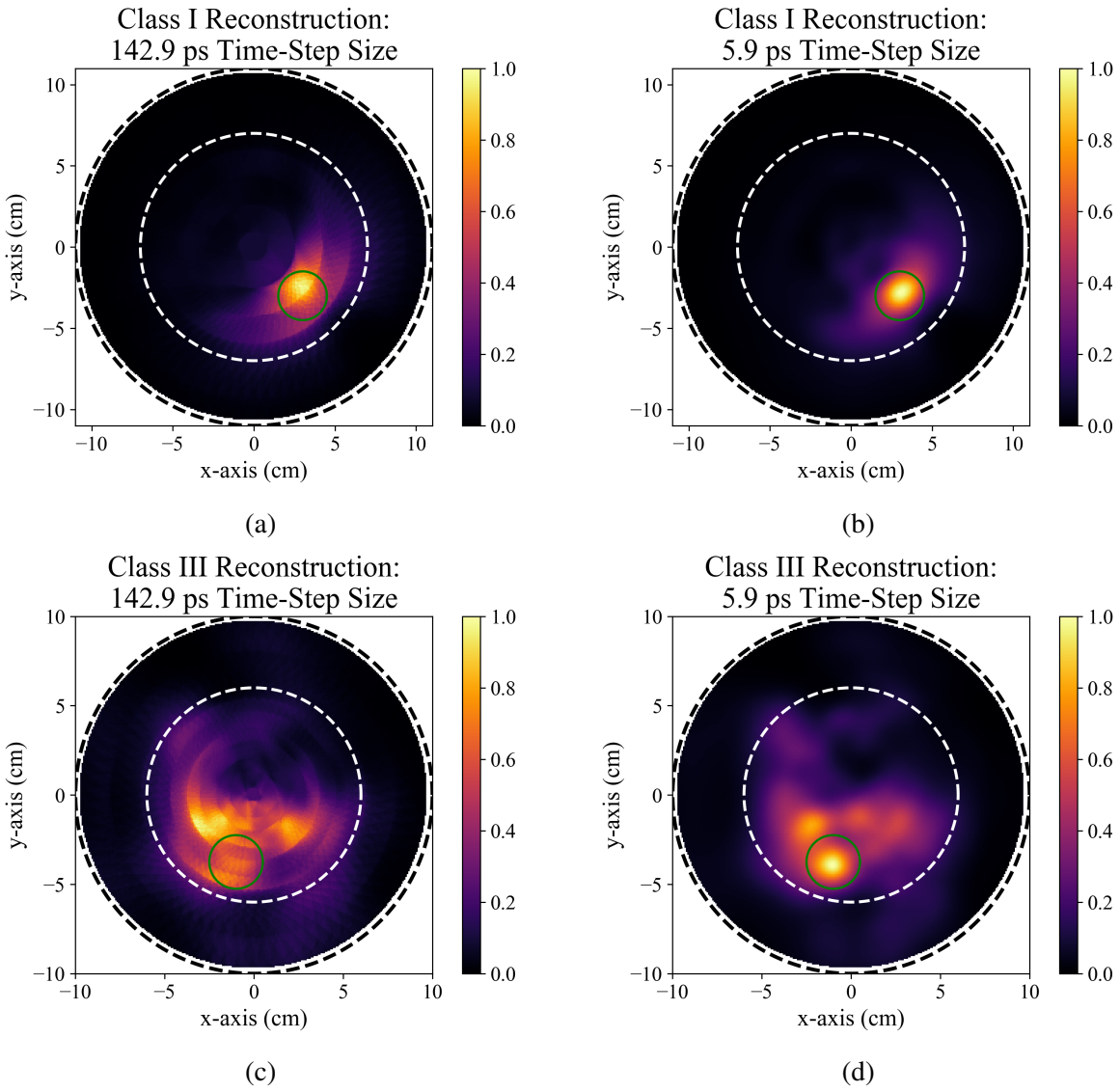
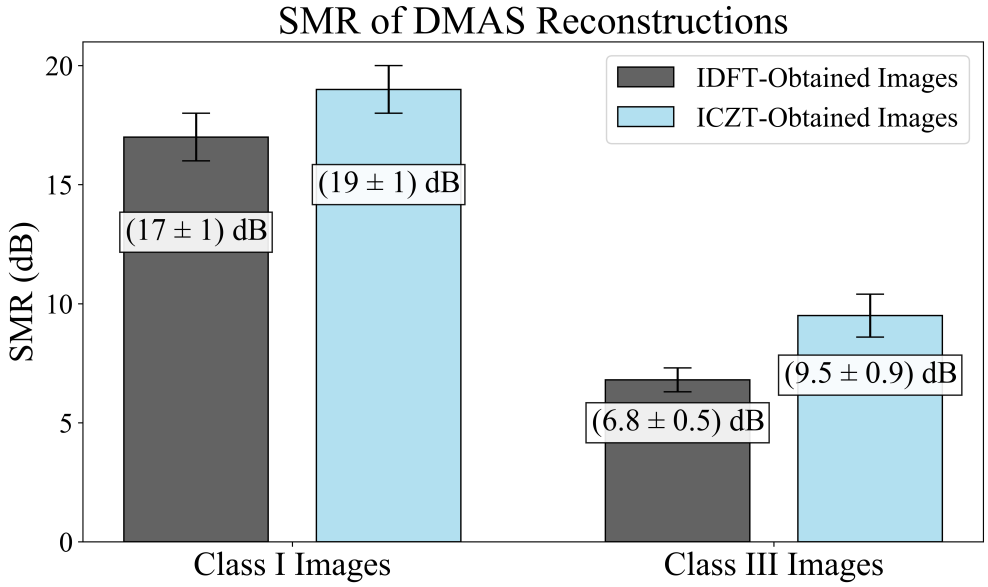


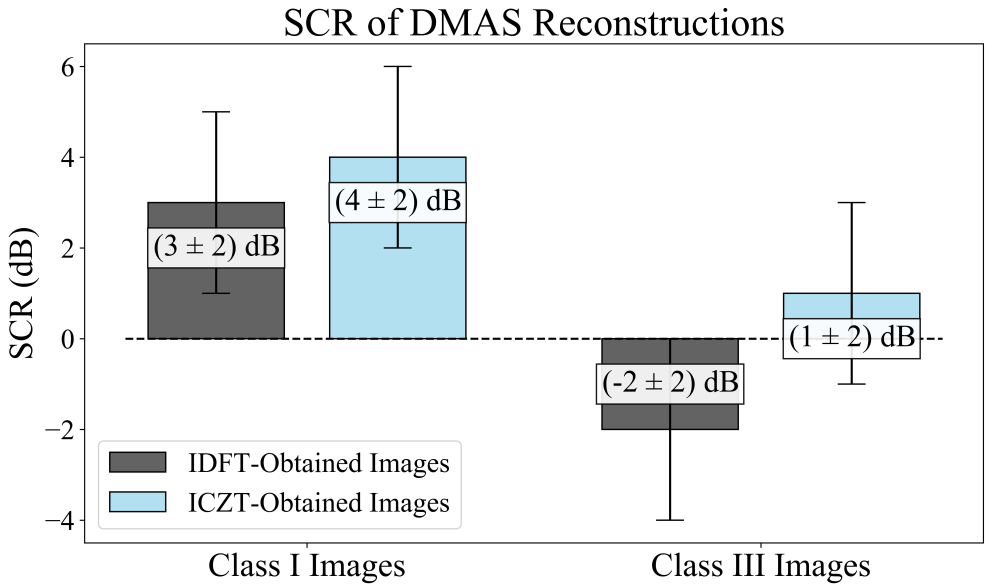
Figure 3.5: DMAS reconstructions of a 15 mm radius lesion in a Class I phantom using (a) the IDFT and (b) the ICZT, and of a 15 mm radius lesion in a Class III phantom using (c) the IDFT and (d) the ICZT. The solid green circle indicates the tumor location, the dashed white circle indicates the approximate phantom boundary, and the dashed black circle indicates the antenna trajectory during the scan. Each image is normalized to its maximum intensity value. Figure adapted from [104].

The SMR and SCR of each reconstruction are displayed in Fig. 3.6. No significant difference in either metric was observed in the Class I images, but the SMR of the ICZT-obtained Class III phantom reconstruction was significantly greater than that of the IDFT-obtained image. The SCR of the IDFT-obtained reconstruction of the Class III phantom was negative, indicating that the

largest response in the image occurred outside of the known tumor region, and therefore the tumor response was not identifiable in the reconstruction, as can be directly observed in Fig. 3.5 (c).



(a)



(b)

Figure 3.6: (a) SMR and (b) SCR of images in Fig. 3.5. Figure adapted from [104].

3.3.2 Evaluation of the Novel itDAS Algorithm

Reconstructions of four representative phantoms from the 27 tumor-containing scans are displayed in Fig. 3.7. The reconstructions produced by the DAS, DMAS, itDAS, and itDMAS beamformers of phantoms from each of the four BI-RADS density classification categories are displayed. The SMR and SCR of these images are displayed in Table 3.2. The iterative beamformers consistently produced higher SCR and significantly higher SMR than the non-iterative literature-standard algorithms.

Table 3.2: Image Quality Metrics of Reconstructions Displayed in Figure 3.7

		DAS	DMAS	itDAS	itDMAS
Class I Images	SMR (dB)	11 ± 1	19 ± 2	29 ± 2	30 ± 3
	SCR (dB)	1 ± 2	1 ± 2	2 ± 3	2 ± 3
Class II Images	SMR (dB)	4.2 ± 0.5	7.7 ± 0.9	13 ± 2	16 ± 2
	SCR (dB)	0 ± 1	0 ± 2	1 ± 2	1 ± 2
Class III Images	SMR (dB)	3.2 ± 0.6	6 ± 1	12 ± 2	16 ± 2
	SCR (dB)	1 ± 1	2 ± 2	4 ± 2	5 ± 3
Class IV Images	SMR (dB)	6.5 ± 0.4	10.7 ± 0.6	18 ± 1	22 ± 1
	SCR (dB)	0 ± 2	1 ± 2	0 ± 2	0 ± 2

3.3.3 Reconstructions using Correction Factors with the itDAS Beamformer

Reconstructions of the A1F1 Class II phantom by the itDAS beamformer using various correction factors are displayed in Fig. 3.8, and the SMR and SCR of the reconstruction methods are displayed in Table 3.3. Only the output pulse correction factor consistently improved the image contrast - the beam pattern correction factor consistently reduced SMR (but did not affect SCR), indicating that modeling the antennas beam pattern increased the intensity of the low-intensity clutter in the images. Correcting for the antenna's frequency-dependent gain did not have a significant effect on either the SMR or SCR of any reconstructed image - but did increase the SMR (albeit not significantly) in three images. Modeling the VNA's output pulse improved the SMR in

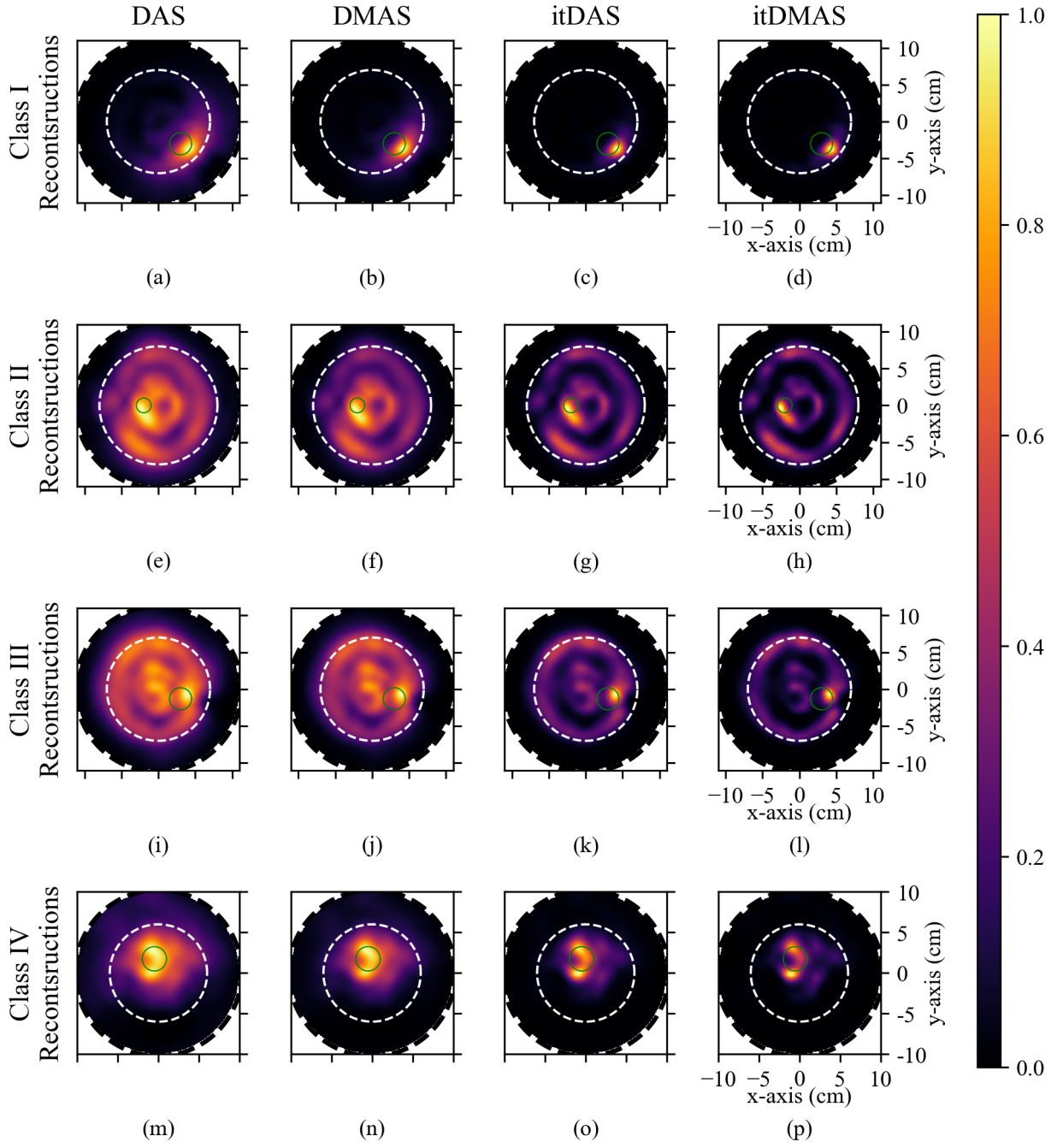


Figure 3.7: Reconstructions of breast phantoms by (left to right) the DAS, DMAS, itDAS, and itDMAS beamformers. (a-d) display the reconstructions of a 15 mm radius lesion in a Class I (A2F1) phantom, (e-h) display the reconstructions of a 10 mm radius lesion in a Class II (A3F4) phantom, (i-l) display the reconstructions of a 15 mm radius lesion in a Class III (A2F4) phantom, and (m-p) display the reconstructions of a 15 mm radius lesion in a Class IV (A1F4) phantom. Each image is normalized to its maximum intensity. The dashed black circle indicates the antenna trajectory during the scan, the dashed white line indicates the approximate breast phantom boundary, and the solid green circle indicates the known tumor position. Figure adapted from [105].

all reconstructions (significantly improved in three reconstructions) and improved the SCR in three reconstructions. Correcting for the VNA's output pulse consistently reduced low-intensity image clutter (indicated by the consistent SMR improvements) and reduced high-intensity clutter in some cases (indicated by the improved SCR in three images).

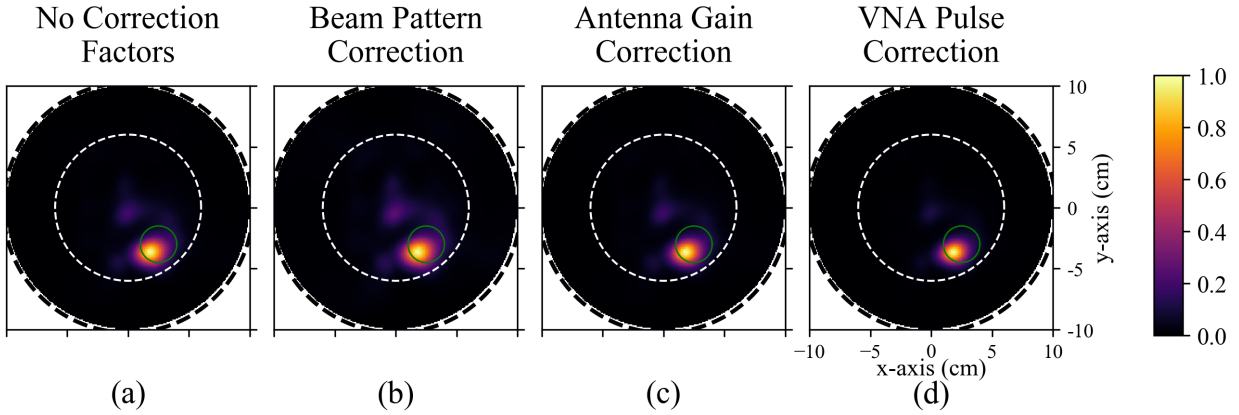


Figure 3.8: itDAS reconstructions of the A1F1 Class II phantom containing a 15 mm radius tumor produced using (a) no correction factors, (b) the correction factor for the antenna's beam pattern, as described in Eq. 3.5, (c) the correction factor for the antenna's gain, as described in Eq. 3.6, and (d) the correction factor for the VNA's output pulse, as described in Eq. 3.7. Each image is normalized to its maximum intensity. The dashed black circle indicates the antenna trajectory during the scan, the dashed white line indicates the approximate breast phantom boundary, and the solid green circle indicates the known tumor position.

Table 3.3: Image Quality Metrics of Reconstructions Displayed in Figure 3.8

	No Corrections	Antenna Beam	Antenna Gain	VNA Pulse
SMR (dB)	29 ± 2	26 ± 2	30 ± 2	35 ± 2
SCR (dB)	7 ± 2	7 ± 2	8 ± 2	9 ± 2

3.4 Discussion

3.4.1 Determination of Optimal Time-Domain Resolution with the ICZT

Tumor-detection and artifact presence are clearly dependent on the choice of time-step size used to represent the TD radar signals, as is evident in Fig. 3.5 (c) and Fig. 3.5 (d). To further

explore this relationship, Fig. 3.9 displays reconstructed images of the Class III phantom for four choices of time-step size, varying from 142.9 ps (IDFT equivalent) to 10.9 ps. The images in Fig. 3.9 (a)-(c) contain prominent ring artifacts, but these artifacts are not apparent in Fig. 3.9.

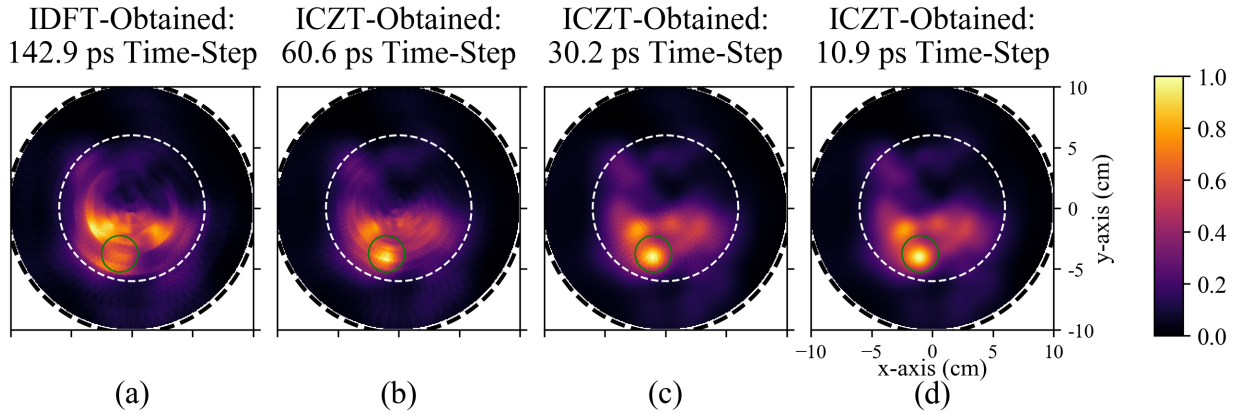


Figure 3.9: DMAS reconstructions of a 15 mm radius lesion in a Class III phantom using (a) the IDFT, (b) the ICZT with 100 time-points from 0 ns to 6 ns (60.6 ps time-step size), (c) the ICZT with 200 time-points (30.2 ps time-step size), and (d) the ICZT with 550 time-points (10.9 ps time-step size). Figure adapted from [104].

The results in Fig. 3.9 indicate that a time-step size of $\Delta t \leq 10.9$ ps is sufficient for artifact reduction. To examine the impact of time-step size on tumor detection, the localization error in reconstructions of the Class III phantom produced using various time-step sizes for FD-to-TD conversion was determined. These localization errors are displayed in Fig. 3.10.

These results indicate that for a time-step size $\Delta t \leq 4$ ps, the localization error in the image is unchanged, and for time-step sizes smaller than 20.1 ps (corresponding to 300 time-points used in the ICZT over 0-6 ns), the change in localization error is less than 1 mm. All time-step sizes less than that obtained when using the IDFT resulted in a localization error that was smaller than the tumor radius, indicating that these reconstructions contained an identifiable tumor response within the known tumor region. This indicates that reducing the time-step size from that obtained with the IDFT is sufficient for tumor-detection.

Given that 10.9 ps is sufficient for artifact reduction and tumor-detection, the maximum-allowable time-step size should be identified. A larger time-step size is desirable because it reduces the di-

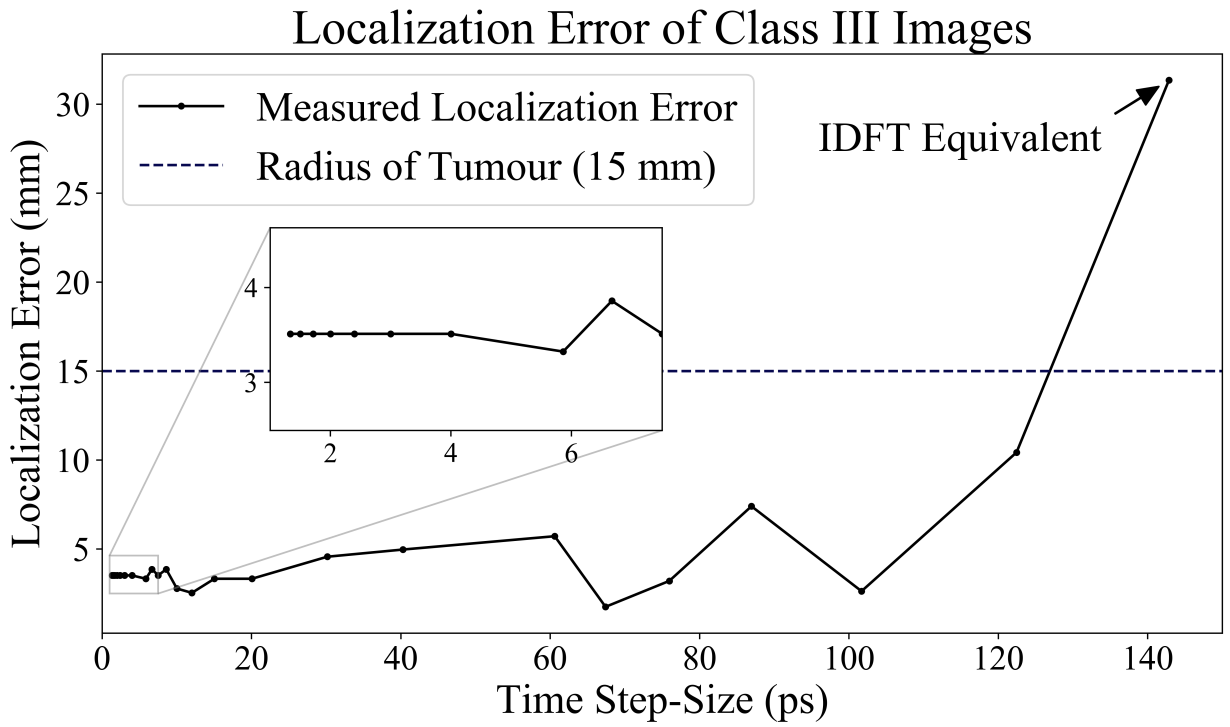


Figure 3.10: Localization error of the Class III reconstructions as a function of the time-step size. The dashed line indicates the radius of the tumor. Figure adapted from [104].

mensionality of the radar signals, reducing computation time during image reconstruction and during the application of signal processing methods. To quantify the presence of the ring artifacts, the total absolute-difference between images using a specified time-step size and the image produced using a time-step size of 5.9 ps were determined. This total absolute-difference D is defined as,

$$D = \sum_{i,j} |\sigma_{i,j}^{tar} - \sigma_{i,j}^{ref}|, \tag{3.11}$$

where $\sigma_{i,j}^{tar}$ is the intensity of the pixel at index (i, j) in the target image and $\sigma_{i,j}^{ref}$ is the intensity of the pixel at index (i, j) in the reference image (the image reconstructed after evaluating the ICZT at 1024 time-points over 0-6 ns). The reconstruction produced using the time-step size of 5.9 ps was selected as the reference image due to the absence of ring artifacts in the reconstruction, as displayed in Fig. 3.5 (b) and Fig. 3.5 (d).

While this metric does not specifically quantify the prominence of the ring artifacts, it is clear

from Fig. 3.9 that the most prominent differences in the reconstructions of the Class III phantom, produced with different time-step sizes, are due to the presence of the ring artifacts. Given that the image produced using a time-step size of 5.9 ps has the least prominent artifacts, the total absolute difference provides a measure of the relative impact of the ring artifacts on the image.

If the width of the ring artifacts determines the difference metric D, then D should be linearly related to the time-step size used in the ICZT (equivalently, D is inversely proportional to the number of time-points used to evaluate the ICZT along a fixed time-window). The ring widths w_{ring} are therefore hypothesized to be proportional to the time-step size used to represent the radar signals,

$$w_{ring} = v\Delta t, \tag{3.12}$$

where v is the estimated average propagation speed used in the reconstruction method. The DMAS beamformer back-projects the individual radar signals onto the image-space using the time-of-flights (as in Eq. 1.4). To determine the localization of the radar responses, the spatial arc that corresponds to a particular time-of-response t of single radar signal corresponds to the positions $\mathbf{r}$ such that

$$v\Big(t - \frac{\Delta t}{2}\Big) \leq |\mathbf{r}| \leq v\Big(t + \frac{\Delta t}{2}\Big). \tag{3.13}$$

The width of these arcs is therefore determined by the time-step size Δt, and $\Delta t \propto \frac{1}{N}$ where N is the number of time-points used in the ICZT over a specified time-window. If the ring artifacts in the images are caused by Δt, as hypothesized, and if the total absolute difference metric D is primarily determined by the differences in the ring-artifacts between images, then D will also be inversely proportional to N.

To determine the variation of this difference metric D across scans of the same phantom, ten scans of the Class III phantom were performed. The average values of the metric D across the reconstructions of the ten scans are displayed in Fig. 3.11. The hypothesized inverse relationship

between D and N was evaluated by fitting the relationship

$$D = \frac{a}{N} + b \tag{3.14}$$

to the measured values, where a and b were the fit parameters. The fit is displayed in red in Fig. 3.11, with the 99.7% confidence intervals displayed in the transparent shaded red region.

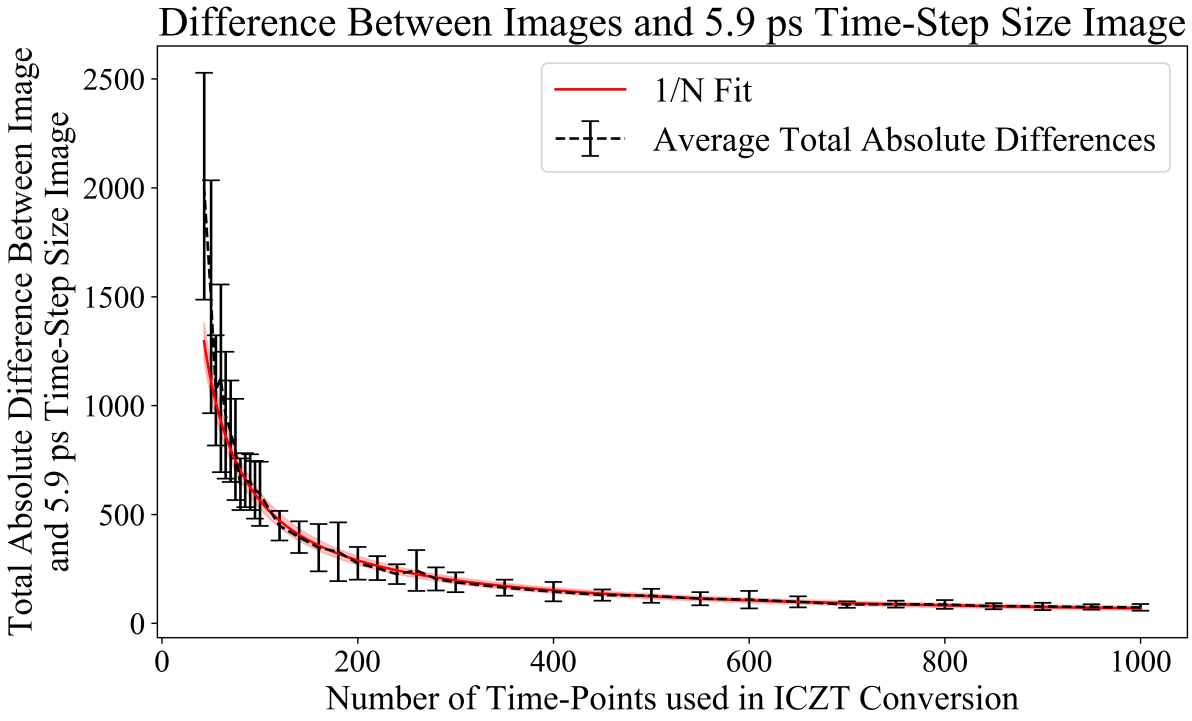


Figure 3.11: Average total absolute-difference of images produced using time-step sizes greater than 5.9 ps and the image produced after using the ICZT for FD-to-TD conversion with a time-step size of 5.9 ps, for 10 scans of the Class III phantom. Standard deviations of the average total absolute-difference over the images from the 10 scans are the displayed uncertainties. The shaded red region indicates the 99.7% confidence intervals on the fit. Figure adapted from [104].

Fig. 3.11 indicates that the total absolute difference between the target image and the reference image (produced using 5.9 ps time-step size) is inversely proportional to the number of time-points used in the ICZT. All measured points (excluding the point obtained from using the smallest number of time-points) are in agreement with this hypothesized relationship. These results are in support of the hypothesized relationship, indicating the width of the ring artifacts is caused by the

time-step size used in the ICZT. The time-step used in evaluation of the ICZT can therefore be selected to minimize the prominence of these artifacts.

The reconstructed image produced with a time-step size of 10.9 ps (equivalent to 550 time-points over 0-6 ns) was the image produced with the largest time-step that produced a difference metric D that was in agreement with the difference metric of the reconstruction produced using 1000 time-points, within the reported uncertainties. This indicates that the artifacts are not significantly different in these two reconstructions, as can be seen by comparing Fig. 3.5 (d) and Fig. 3.9 (d). A time-step of $\Delta t \leq 10.9$ ps is therefore sufficient for artifact reduction.

A time-step size of 10.9 ps is therefore sufficient for both tumor-detection (as indicated in Fig. 3.10) and artifact-reduction (as indicated in Fig. 3.11) in radar-based image reconstruction for the pre-clinical BMS system [17] used in this work. This system operates over 1-8 GHz and the necessary time-step size used to represent TD radar signals may be dependent on the bandwidth of the system.

The ICZT has been used in other systems for FD-to-TD conversion [71]. The system in [71] operated over 50 MHz to 20 GHz, resulting in a time-step size of $\Delta t \approx 50$ ps in TD radar signals obtained via the IDFT. This time-step size is approximately $\frac{1}{3}$ the size of the time-step obtained with the IDFT for the 1-8 GHz system used herein. The authors of [71] presented a brief analysis comparing the effects of the ICZT and IDFT on the contrast in reconstructed images. The results reported in [71] demonstrated that the use of the ICZT increased image contrast but no discussion of image artifacts was presented. Because the time-step of the IDFT-obtained signals in [71] is approximately $\frac{1}{3}$ the size of the time-step obtained with the IDFT in the system used herein, the ring artifacts produced in [71] are expected to be approximately $\frac{1}{3}$ the size of those present in reconstructions obtained after using the IDFT for FD-to-TD conversion with our system. The ring artifacts present in the images in [71] are less prominent than those obtained with our system in Fig. 3.9 (a), but are similar to the reconstruction in Fig. 3.9 (c), where the prominence of the ring artifacts has been reduced.

This investigation examined the effects of time-step size on image reconstruction when using the DMAS beamformer for image reconstruction. The conclusions obtained from this analysis are expected to hold for other DAS-based beamformers. All DAS-based beamformers rely on back-projecting the individual TD radar signals onto the image-space using the estimated time-delays described in Eq. 1.4 and the time-step size will affect the localization precision of the back-projected radar responses. This synthetic focusing procedure is used in all DAS-based beamformers [10, 38–40] and it is this procedure that the choice of time-step size affects.

3.4.2 Comparing the itDAS Algorithm to DAS and DMAS

The itDAS and itDMAS algorithms produced images with higher SMR and SCR than either literature-standard beamformers (DAS and DMAS) across all BI-RADS density classes. The iterative reconstruction methods consistently reduced both high- and low-intensity clutter, as is evident from the reconstructions in Fig. 3.7. In all cases, the iterative algorithms maintained the tumor response while significantly reducing clutter intensity in the images, as indicated in the SCR and SMR in Table 3.2.

All image reconstruction algorithms produced images of the Class I phantom with an identifiable tumor response. However, in Fig. 3.7, the SCRs of the DAS and DMAS reconstructions of the Class III phantom are not significantly greater than zero (as displayed in Table 3.2), indicating that the tumor response is not significantly different from the high-intensity clutter responses in the images. This is not the case for the itDAS and itDMAS reconstructions of the Class III phantom - these beamformers produced reconstructions with tumor responses that were significantly more intense than the high-intensity image clutter, as indicated by their SCRs of 4 ± 2 dB and 5 ± 3 dB (for itDAS and itDMAS respectively).

None of the reconstruction methods employed in this investigation accurately reconstructed the lesion size, but the tumor responses in the itDAS and itDMAS reconstructions in Fig. 3.7 are visible and located in the expected region. No significant differences were observed in the localization

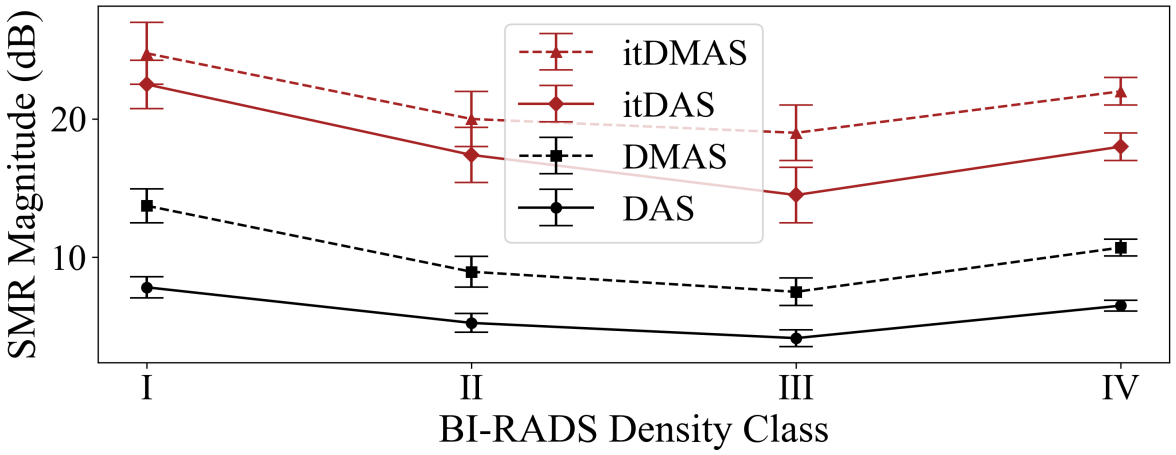
error of the tumor response in the four examined reconstruction algorithms. The localization error of reconstructions produced by the DAS and DMAS methods was (11 $\pm$ 4) mm, (12 $\pm$ 5) mm for itDAS, and (11 $\pm$ 4) mm for itDMAS.

The itDAS algorithm aims to build upon the radar signal model used in radar-based image reconstruction, allowing for the implementation of correction factors to improve the physics model without the large computation time required for tomographic reconstruction methods. The itDAS algorithm had a relative computation time of 11:1 to the DAS method, using a computer with an AMD Ryzen 2700X central processing unit. The non-iterative DAS and DMAS methods produced reconstructions in 9 s and 11 s (respectively), while the itDAS algorithm did so in 99 s. While the iterative algorithm does require a longer computation time, this increase is not prohibitive - the reconstructions were still produced in just over 1.5 minutes. No attempt to optimize the computation was made in this work.

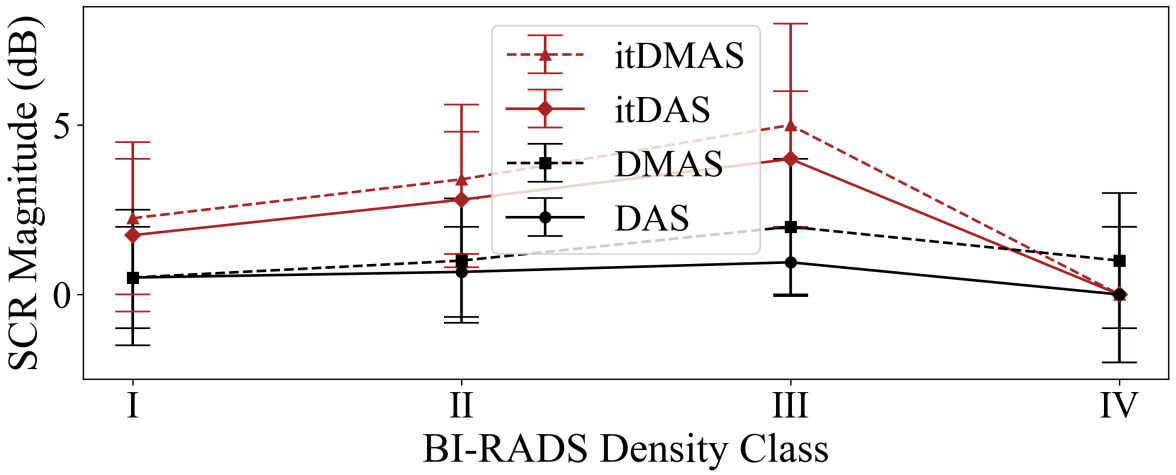
To examine the effects of breast density on image contrast for each of the four beamformers, the average SMR and SCR of the reconstructions produced of the phantoms of each BI-RADS density classification categories with an identifiable tumor response (a reconstructed image was defined to have an identifiable tumor response if the SCR was greater than zero) are displayed in Fig. 3.12.

Across BI-RADS density class, the iterative algorithms produced reconstructions with higher SMR and SCR than the literature standard DAS and DMAS beamformers. DMAS reconstructions were consistently higher-contrast than DAS images, as was found in [35, 42], with an average relative increase in SMR of 75% compared to the DAS beamformer on Class I phantoms, 70% on Class II phantoms, and 81% on Class III phantoms, and 64% on Class IV phantoms.

The iterative methods provided an even greater increase in contrast: the itDAS beamformer increased SMR by an average of 188% for Class I phantoms (relative to the DAS images), 231% for Class II, 249% for Class III, and 177% for Class IV. Improvements in SCR were as large as 321% for Class III phantoms. While both the itDAS and itDMAS reconstruction algorithms re-



(a)



(b)

Figure 3.12: Average (a) SMR and (b) SCR for the reconstruction algorithms using scans of phantoms representative of the four BI-RADS density classification categories. Figure adapted from [105].

sulted in significant increases in both SMR and SCR relative to the non-iterative beamformers, the SMR and SCR of itDAS and itDMAS reconstructions were not significantly different from each other in the majority of reconstructions. This indicates that the iterative structure is the dominant cause of the increased contrast in the iterative algorithms, rather than the pair-wise signal multiplication in itDMAS. Just as the pair-wise signal multiplication in the DMAS beamformer rewards signal coherence while punishing incoherence [38], so too does the iterative structure of the itDAS beamformer.

While the DMAS algorithm was initially presented as a DAS alternative that produced images with higher contrast [38], this is the only benefit to the DMAS beamformer. Unlike DMAS, itDAS both improves image contrast through its iterative structure and has the potential to further improve image quality through the implementation of correction factors into its signal model. Fig. 3.13 displays the measured sinogram (after ideal skin suppression) for the A2F1 phantom scan and the forward projection of the image estimate produced at each of the first six iterations during the itDAS reconstruction. While the tumor response becomes more apparent in later iterations, there are evident differences between the forward projections and the measured sinogram. These differences highlight the limitations of the current radar signal model. Future investigations that implement corrections for signal attenuation and the inhomogeneous propagation speed of the microwave signal are hypothesized to improve the signal model further and to cause the forward projections to more accurately model the measured data.

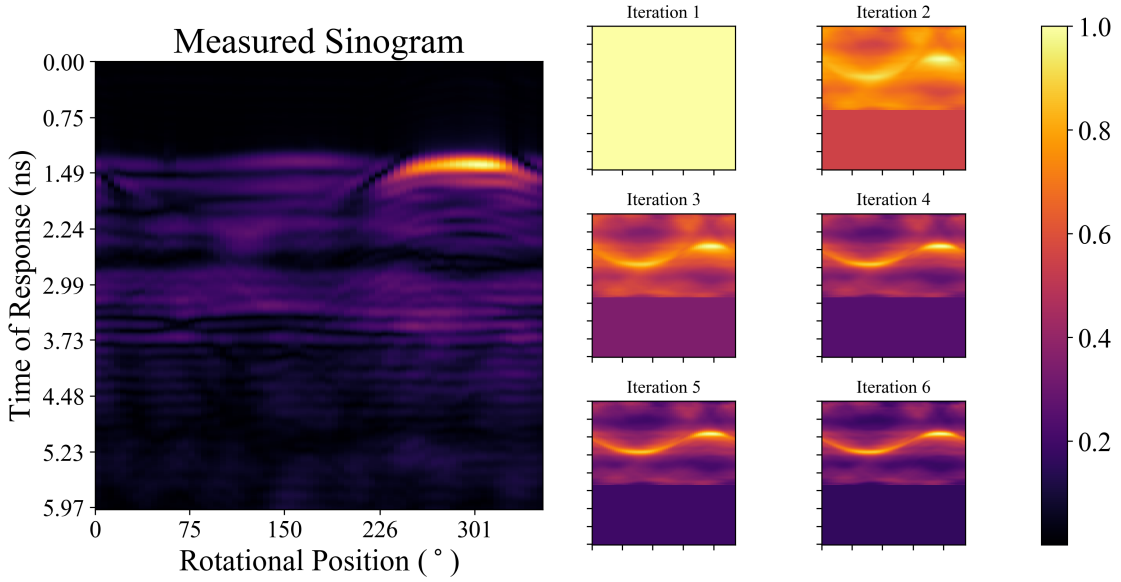


Figure 3.13: The measured sinogram (after ideal skin suppression) and the forward projection of the image estimate at each of the first six iterations during the itDAS reconstruction (displayed in Figure 3.7 (c)) of the Class I phantom. Each sinogram and forward projection has been normalized to have a maximum value of unity. Figure adapted from [105].

Despite the limitations of the forward radar model in the itDAS beamformer as employed in this work, the iterative structure provides significant improvements to image contrast.

3.4.3 Modeling Antenna and System Parameters in itDAS

Correcting for the antennas beam pattern consistently resulted in increased intensity of low-intensity clutter, as measured by the SMR, in reconstructed images. This increase was significant in four images. Modeling the beam pattern results in reducing the reflections that occur at angles off the central axis of the antenna, as can be seen in Fig. 3.2. In an experimental scan with the BMS system used herein, for a tumor that is not located at the center of the imaging chamber, the tumor only lies along the central axis of the antenna at two (opposite) measurement positions. Modeling the antennas beam pattern will result in reducing the tumor response at all other antenna positions and this reduction can be greater than 20 dB (as in Fig. 3.2). While this correction reduces the reflections that occur due to clutter located off the central axis of the antenna, it also reduces the tumor responses at the majority of measurement positions. This may explain the observed reduction in image contrast when this correction is implemented.

Correcting for the antennas gain increased the SMR (albeit not significantly) in four reconstructions and reduced the SMR (also not significantly) in one reconstruction. No change was observed in all other reconstructions. These results indicate that modeling the antenna's frequency-dependent gain may improve image contrast, but the effect is not significant in the majority of cases (in all images examined herein). The antenna gain correction was implemented in the same way as the output pulse correction (as in Eq. 3.6 and Eq. 3.7), and while the output pulse resulted in improved SMR (improvements in all reconstructions and significant improvements in three images) and SCR over the itDAS algorithm without corrections, the antenna gain correction not result in significant improvements. To investigate this, Fig. 3.14 displays the time-domain representation of the antenna gain and the VNA's output pulse, as were used in the implementation of the correction factors in Eq. 3.6 and Eq. 3.7.

The time-domain representation of the antenna gain, $g(t)$, has a narrow (relative to that of the VNA pulse) central lobe, and relatively minor side-lobes. The effects of the gain and output pulse correction factors on the forward model are similar, given the similarities of the time-domain

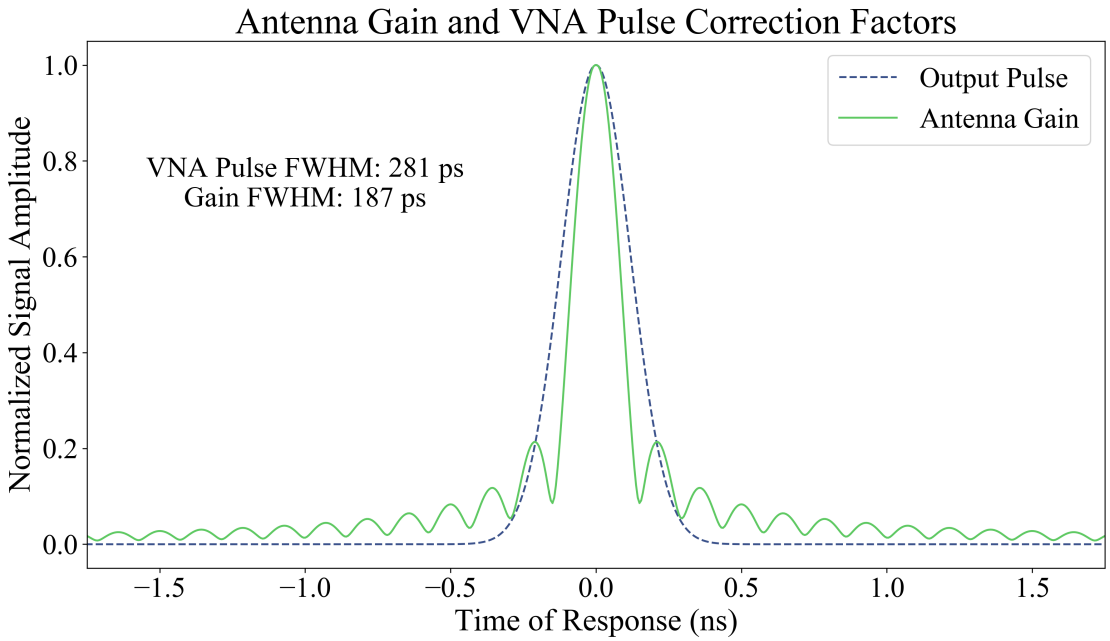
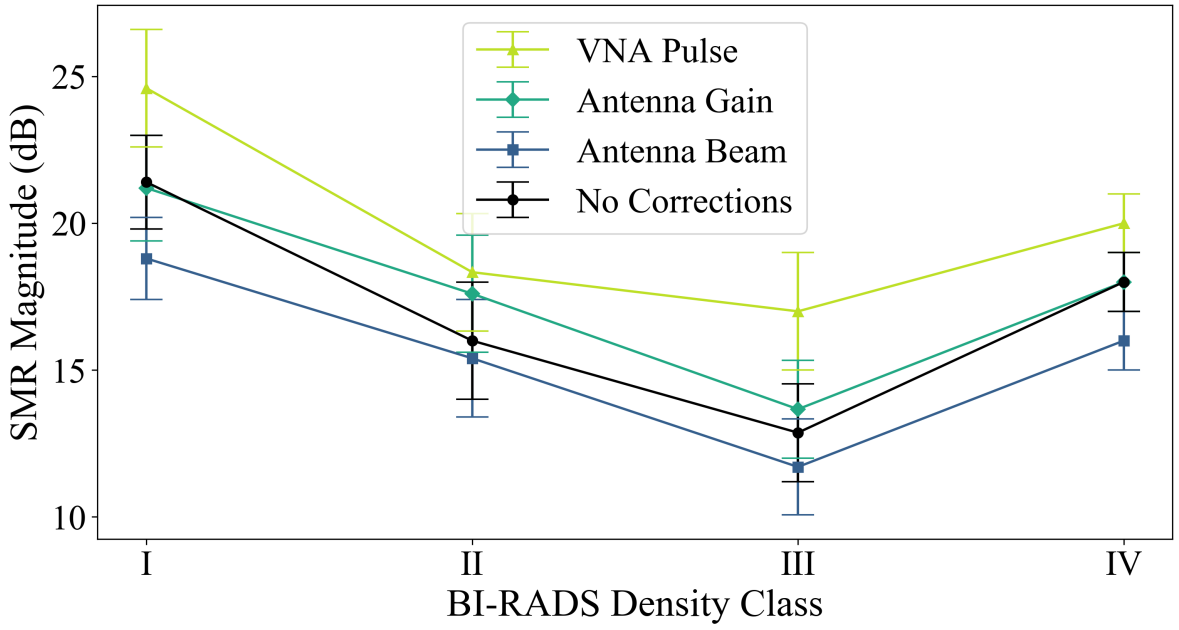


Figure 3.14: The models of the time-domain representation of the antenna's frequency-dependent gain and the output pulse of the VNA used in the implementation of the respective correction factors.

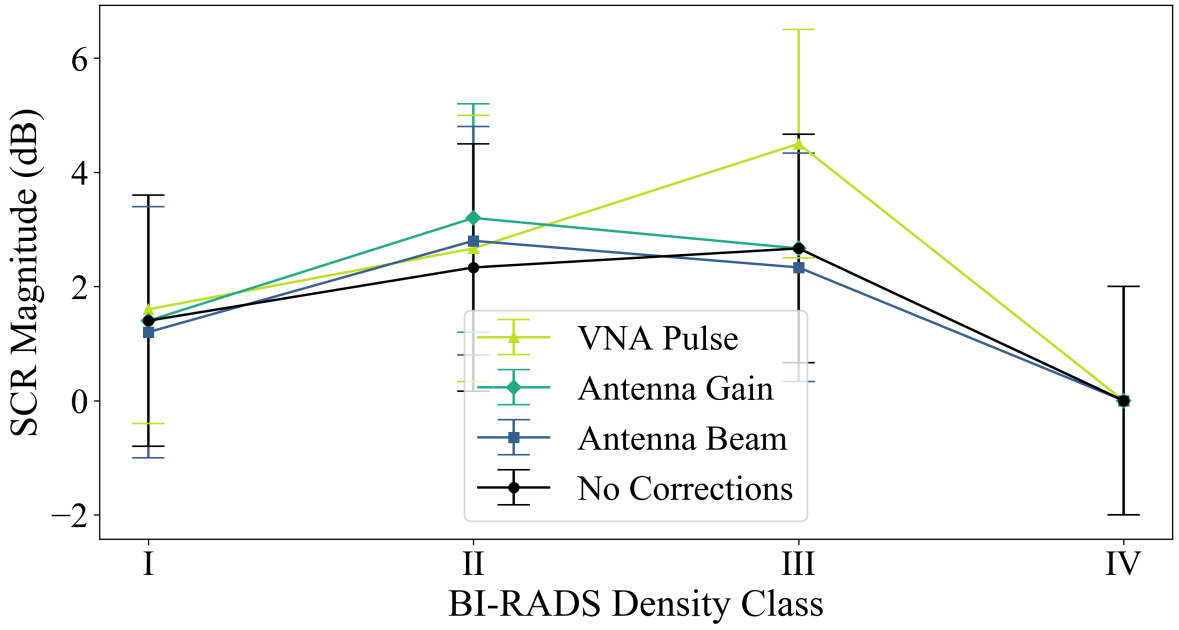
functions of the antenna gain $g(t)$ and output pulse $p(t)$, as displayed in Fig. 3.14, and the similar implementations, as shown in Eq. 3.6 and Eq. 3.7. However, the antenna gain $g(t)$ has a full-width at half-maximum of $\delta t \approx 187$ ps while the output pulse $p(t)$ has a full-width at half-maximum of $\delta t \approx 281$ ps. The wider central lobe of the output pulse function causes the VNA pulse correction factor to have a larger effect on the radar signals $\mathbf{s}_m(t)$ than the antenna gain function.

Fig. 3.15 illustrates the effects of each correction factor on the average SMR and SCR for all reconstructions with an identifiable tumor response of each BI-RADS density class. The output pulse resulted in improved SMR and SCR across all BI-RADS classes, and significantly increased the SMR in Class III reconstructions.

The results obtained in this section indicate that modeling the antenna beam pattern in the itDAS reconstruction algorithm does not improve image contrast, due to the suppression of the tumor-responses for measurement positions where the tumor does not lie along the central axis of the antenna, but that correcting for the antenna's frequency-dependent gain and the output pulse of



(a)



(b)

Figure 3.15: Average (a) SMR and (b) SCR of reconstructions for phantoms of each BI-RADS density classification category produced by the itDAS reconstruction algorithm using various correction factors.

the VNA can improve image contrast, significantly in some cases.

3.5 Conclusion

A time-step size of 11 ps was found to be sufficient for both artifact reduction and tumor-detection for radar-based image reconstruction with the 1-8 GHz used herein. The ICZT was necessary to obtain this and reconstructions produced using the IDFT were found to contain prominent ring artifacts. In one case, the IDFT-obtained reconstruction failed to have an identifiable tumor response, while the ICZT-obtained reconstruction had an identifiable tumor response.

The novel itDAS beamformer was found to produce reconstructions with significantly higher contrast with respect to both high- and low-intensity clutter when compared to either the DAS or DMAS beamformers. These promising results were observed for all BI-RADS density classification categories but the largest increase in contrast was observed in heterogeneously dense BI-RADS Class III phantom reconstructions, increasing contrast by as much as 249% when compared to the DAS beamformer. Only one BI-RADS Class IV phantom was used in this investigation, but the results for the Class III density class are promising, indicating that the itDAS may be more suitable for reconstructing images of dense breasts.

The itDMAS beamformer was also found to increase image contrast, although it did not result in significant increases compared to those obtained with itDAS. This indicates that the primary cause of the increased contrast present in the reconstructions obtained with the iterative beamformers is due to their iterative structure rather than the pair-wise signal multiplication present in itDMAS. Just as the pair-wise signal multiplication in DMAS had initially resulted in improved contrast over DAS [38], the iterative structure of itDAS further improves contrast by rewarding signal coherence within the iterative algorithm structure.

Modeling the antenna's beam pattern in itDAS was found to reduce image contrast due to the suppression of the tumor response in all measurement positions where the tumor was located off the central antenna axis. Correcting for the antenna's frequency-dependent gain was found to increase image contrast, albeit not significantly. Of the three correction factors examined herein, the

only correction which resulted in consistent and significant improvement in image quality was the correction for the output pulse of the VNA. This factor significantly increased image contrast in three reconstructions and increased contrast in all observed reconstructions. These results demonstrate the potential of the itDAS algorithm - individual physics components can be introduced into the signal model and their effects can be individually evaluated. While the three corrections implemented herein made relatively minor modifications to the signal model, significant improvement in image quality was observed when the correction for the output pulse of the VNA was implemented.

4. Application of Machine Learning Methods for Tumor-Detection

This chapter describes the application of machine learning methods for automated tumor detection in breast microwave sensing and the first use of deep learning techniques for tumor detection with UM-BMID. The challenge of overfitting using experimental datasets is discussed and three approaches used to improve model generalization are investigated. The selection of machine learning algorithms that can exploit the inherent locality of the sinogram data representation is discussed and the performance of such algorithms is compared to the performance of machine learning techniques that can not utilize the sinogram structure. A brief comparison between the diagnostic performance of machine learning methods and image-based tumor detection using the DAS, DMAS, and itDAS algorithms is presented, and an estimate of the diagnostic performance of machine learning methods for automated tumor detection in an air-based breast microwave sensing system is described.

4.1 Introduction to Machine Learning Methods in BMS

Machine learning methods in breast microwave sensing have examined classification of tumor responses as benign or malignant [80–83]. No large-scale experimental examinations have been presented in the literature to-date, with most research either using simulated data [83–85] or small-scale experimental datasets [80–82, 86–89], using up to 150 scans of 10 unique phantoms in [86].

Machine learning methods offer an alternative to image-based tumor detection approaches. Given the challenges in skin suppression techniques, image reconstruction algorithms, objective

image quality metric development, and image-based tumor detection criteria in radar-based breast microwave imaging, machine learning methods that predict the presence of a tumor using only the measured electromagnetic data may allow for tumor-detection without having to address these challenges. The itDAS beamformer presented in Chapter 3 of this thesis outperformed standard beamforming approaches with respect to image quality, but image-based diagnosis also requires the development of robust and objective image-based tumor detection criteria and skin suppression methods. Future work in radar-based imaging can explore these challenges, but machine learning methods may overcome the challenges by using the raw measured electromagnetic information directly.

A thorough analysis of the potential diagnostic performance of machine learning methods for tumor-detection in experimental measurements is absent from the literature. The difficulty in constructing breast phantoms and the time required to perform experimental scans may have limited the development of large experimental datasets, but the University of Manitoba Breast Microwave Imaging Dataset [44] was developed to address these challenges and contains over 1257 scans of MRI-derived phantoms. This dataset is an order of magnitude larger than any presented in the published literature to-date and has provided the opportunity to evaluate machine learning algorithms on a relatively large-scale experimental dataset.

This work presents, to the best of our knowledge, the first thorough investigation into the potential diagnostic utility of machine learning methods for automated tumor diagnosis in breast microwave sensing using UM-BMID. The challenges inherent to using experimental datasets are described, techniques for improving model generalizability are discussed, and an estimate of the diagnostic performance of machine learning techniques for tumor detection is presented.

4.2 Methods

4.2.1 Defining Tumor-Detection as a Binary Classification Problem

Breast cancer screening with mammography is performed to detect the presence of a cancerous lesion in the breast, but the diagnostic outcome of a mammogram is not a binary classification. A mammogram of the breast is classified into one of seven categories in the BI-RADS assessment scheme [5], as displayed in Table 4.1. Categories 2–6 indicate that a mass was detected in the breast and different paths of differential diagnosis are recommended for these categories [5].

Table 4.1: BI-RADS Assessment Categories [5]

Assessment Category	Description
Category 0	Incomplete information
Category 1	Negative result - no indication of malignant tumor
Category 2	Benign mass detected
Category 3	Likely benign mass detected
Category 4	Suspicious mass detected
Category 5	Likely malignant mass detected
Category 6	Known biopsy-proven malignant mass

Differentiating benign and malignant tumors is necessary for clinical breast cancer diagnosis. A misdiagnosis of a benign mass can result in unnecessary invasive procedures (biopsy), further imaging (which also exposes a patient to risks, including further exposure to ionizing radiation if a second mammogram is performed), and stress to the patient. False-positives have a cost to both the healthcare system and to the individual patients. False-negatives are also clearly a cause for concern - a misdiagnosis of a malignant mass can result in untreated cancerous growth and may ultimately result in death.

Cancer detection is not, in general, a binary classification problem in a realistic clinical scenario. However, the ultimate goal of diagnosis is a binary classification task - cancer is either

present or absent in the patient. Broadly, the biological ground-truth can also be viewed as a binary (a cancerous mass is present or absent). From this higher-level perspective, cancer detection can be seen as a binary classification task. This model is also a relatively straight-forward approach for an initial investigation into the diagnostic viability of a novel cancer detection method. Given that a large-scale experimental investigation into the diagnostic capability of machine learning methods in breast microwave sensing has yet to be performed, the problem of cancer detection can be reasonably modeled as a binary classification problem, in which the predicted outcome from a scan of the breast is the presence (or absence) of a cancerous lesion. This work is performed under the assumption that breast cancer diagnosis can be reasonably framed as a binary classification problem.

4.2.2 Selected Datasets

The University of Manitoba Breast Microwave Imaging Dataset (UM-BMID) contains data from 249 scans of first-generation phantoms (Fig. 2.1) and 1008 scans of second-generation phantoms (Fig. 2.3), excluding reference scans. UM-BMID was divided into two generations based on the generation of phantoms that were used in the scans - the first generation of UM-BMID consists of the scans performed with the first-generation phantoms and the second-generation of UM-BMID consists of the scans performed with the second-generation phantoms.

Both generations of UM-BMID were used in this work. The first-generation dataset was used to perform an initial investigation into the viability of machine learning methods for tumor-detection and the second-generation dataset was used to more rigorously investigate the diagnostic performance of these methods on a larger and more diverse dataset. Table 4.2 displays a comparison of the two generations of UM-BMID.

Table 4.2: Comparison of the Two Generations of UM-BMID, Adapted from [44]

	Generation-One	Generation-Two
Number of scans	249	1008
Number of unique phantoms	13	66
Measured S-parameters	S_{11}	S_{11}, S_{21}
3D-printed material	Polycarbonate	Polycarbonate Copolyester
Coating material	Polyurethane	None

4.2.3 Data Structure and Model Selection

Tumor-detection can be performed using the raw measured information from a scan or some transformation of that data. Image-based classification is dependent on the choice of image reconstruction algorithm, and given the present challenges in image reconstruction in BMS, this approach is premature. This work will explore the viability of using machine learning methods for breast cancer diagnosis in BMS using the magnitude of the time-domain S_{11} scattering parameters. Although S_{21} measurements were collected in the 1008 scans that comprise the second-generation of UM-BMID, this initial investigation only utilizes the S_{11} information.

During an experimental scan, the pre-clinical BMS system used herein [17] performs frequency-domain measurements at 1001 linearly-spaced frequencies over 1-8 GHz at 72 antenna positions along a circular scan trajectory. This 1001×72 complex array contains all electromagnetic information from the scan, but the relationship between the frequency-domain scattering parameters and the presence of a tumor is highly nonlinear. An approach that utilizes the frequency-domain S-parameters for classification would also have a feature-space with a large dimensionality (72072 complex features using the 1001×72 measured array). However, the S-parameters can be converted to the time-domain with the inverse discrete Fourier transform. This time-domain sinogram can be used to reduce the dimensionality of the feature space, as only a small portion of the 1001 time-points contains information about reflections originating from the breast tissues. A time-domain window can be applied to remove these unwanted signals, reducing the dimensional-

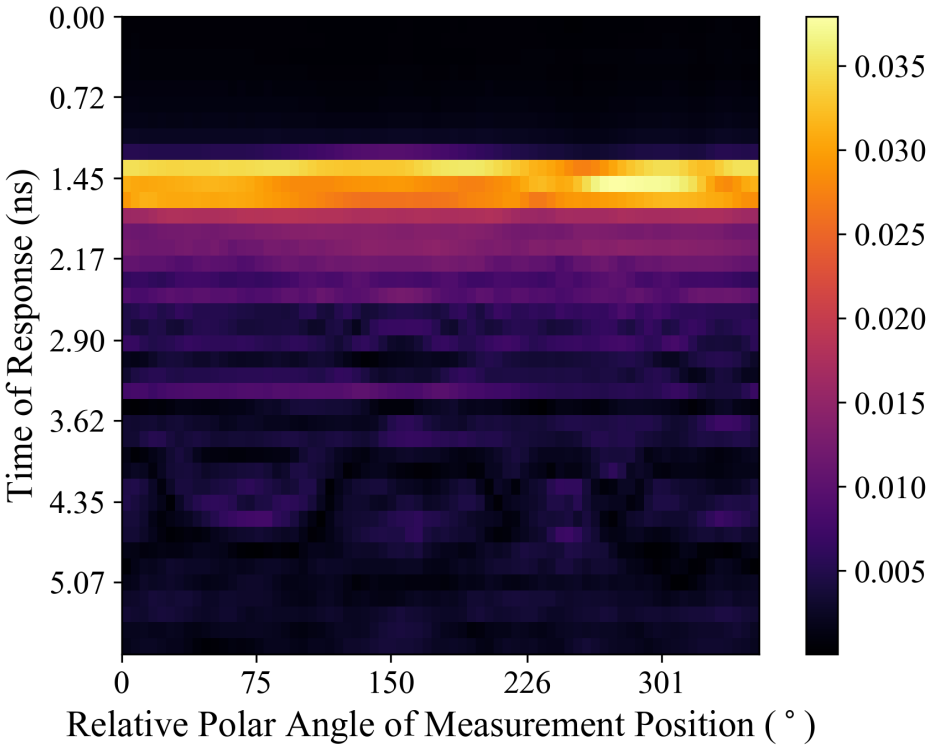


Figure 4.1: Sinogram obtained from phantom scan.

ity from 1001×72 to 35×72. This 35×72 array of magnitude of the time-domain S_{11} parameters is referred to as a sinogram. A sample time-domain sinogram is displayed in Fig. 4.1.

This sinogram structure has another advantage over the frequency-domain representation. There is inherent locality to the pixels within the sinogram. The locality along the time dimension is clear – this dimension of the sinogram corresponds to the time-domain responses measured from one antenna position, and therefore two adjacent pixels correspond to two nearby responses in the time-domain. The locality along the rotational angle dimension is due to the circular antenna trajectory during the scan. Each antenna measurement position is located at a polar angle of ≈4.9° from the neighboring positions. Adjacent pixels along the rotational angle dimension therefore also have an inherent locality. This locality in the data structure can also be observed in Fig. 4.2, in which the sinogram obtained from a scan of a metal rod is displayed. This metal rod acts as an impulse for the imaging system and produces an approximately sinusoidal response in the sinogram space.

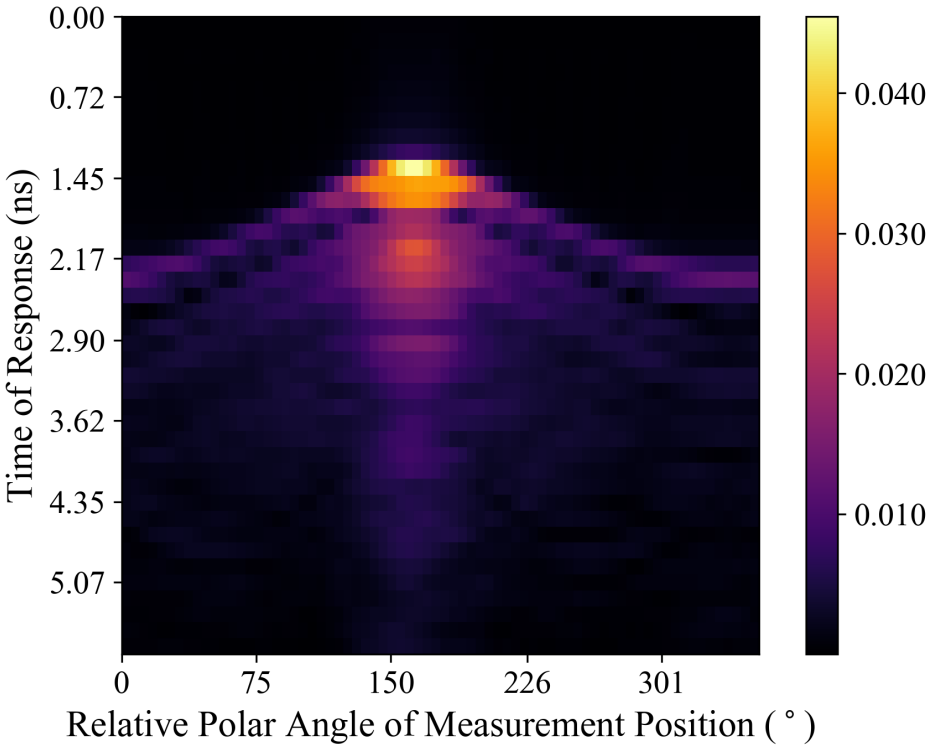


Figure 4.2: Sinogram obtained from scan of 2 mm diameter metal rod in imaging chamber.

Convolutional neural networks (CNNs) are capable of exploiting the inherent locality that is present in image-like data structures (ex: images of handwritten digits) [115]. Because the measured scan data can be represented as a sinogram, CNNs may outperform other classification techniques due to their ability to use the inherent structural information of the data. Other typical classification algorithms fail to utilize the inherent structural information, and these methods, including dense neural networks (DNNs) and logistic regression, are expected to be outperformed by CNNs. CNNs have not yet been used with the sinogram structure for machine learning applications in BMS, and this work presents, to the best of our knowledge, the first investigation into the diagnostic viability of this approach.

4.2.4 Machine Learning Models and Training Methods

Two machine learning models were used in this investigation. A logistic regression classifier was used as a representative shallow-learning classifier, and a CNN was used as a representative deep-learning model that could exploit the inherent locality in the sinogram data structure.

The investigation using the first generation of UM-BMID randomly assigned 50 samples to the testing set (the remaining 199 samples were assigned to the training set and were used for grid-search cross-validation). The 50 test samples were randomly selected, under the following conditions: the test set was required to have approximately uniform distributions over class label (i.e., 50% of test samples contained a tumor), BI-RADS density classification category, and tumor-size. Additionally, no sample in the test set had the same tumor position, tumor size, and phantom ID as any sample in the training set.

The investigation using the second generation of UM-BMID used a test set consisting of 250 samples. These samples were randomly selected, under the same conditions that were used for the first generation of UM-BMID, with the additional criteria that the second generation test set must be approximately uniform over adipose-shell ID. Division into training and testing sets occurred before any further training methods.

All models were trained using 5-fold grid-search cross-validation. The logistic regression classifier was used with L2-regularization and grid-search was obtained to determine the best-performing value of the inverse of the regularization weight parameter (denoted as C) over a logarithmic grid over the bounds $10^{-7} \leq C \leq 10^{23}$. The number of epochs used when training the CNN was defined as the hyperparameter for the CNN models, and the grid-search was performed over a linear grid over the bounds $1 \leq N \leq 5000$ where N is the number of epochs, with a grid step-size of 1 epoch. The best-performing hyperparameters were determined as those which resulted in the highest average ROC AUC on the validation sets.

The CNN was trained using the Adam optimizer [116]. The parameters of the Adam optimizer

used in this work are displayed in Table 4.3. These parameters are the defaults in TensorFlow 2.0. A batch size of 32 samples was used in training and the categorical cross entropy was used as the cost function during training.

Table 4.3: Parameters of the Adam Optimizer used in this Investigation

Parameter	Value
Learning rate	0.001
β_1	0.9
β_2	0.999
ε	10^{-7}

The initial CNN architecture was:

- Input (35×72 sinogram)
- Convolutional layer (32 filters, each 3×3 with relu activation)
- Max pooling layer (3×3 kernel)
- Dense output layer (2 neurons with softmax activation)

All reported results are the averages over 20 runs, and the reported uncertainties are the standard deviations of the metric values over these runs. The diagnostic accuracy, sensitivity, specificity, and ROC AUC were used as performance metrics.

4.3 Results

4.3.1 Classifier Performance on UM-BMID Gen-1

The average validation ROC AUC as a function of number of training epochs is displayed in Fig. 4.3. Based on the results in Fig. 4.3, the optimal number of training epochs was selected to

be 105 epochs. A similar analysis was performed for all grid-search cross-validation procedures in this work.

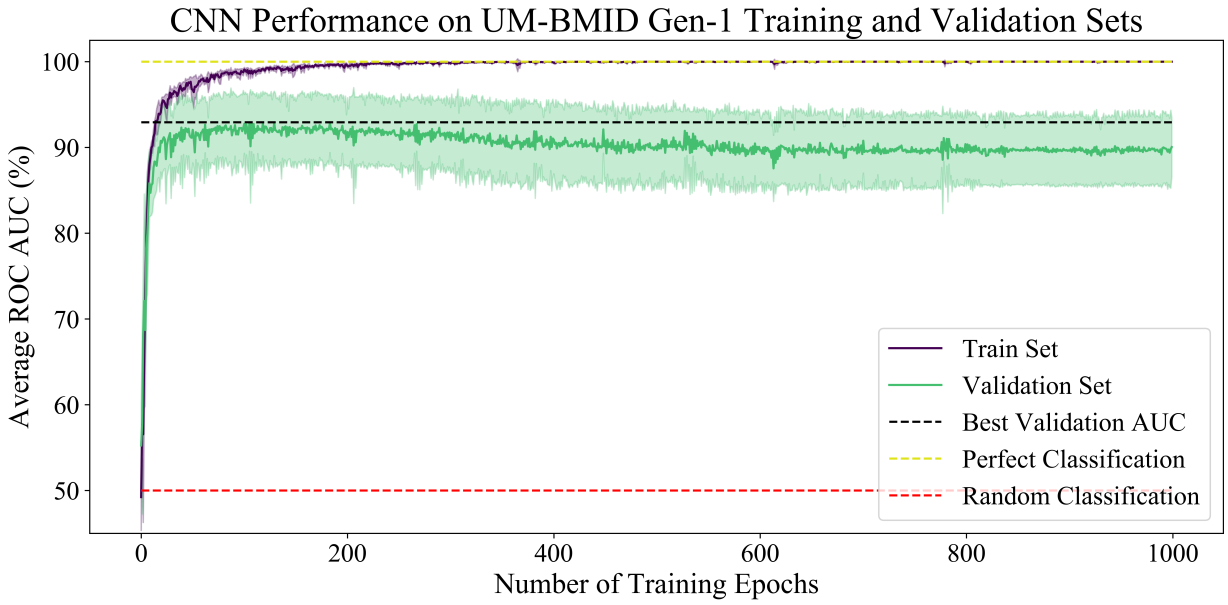


Figure 4.3: Average ROC AUC over cross validation sets to determine optimal number of training epochs when using the first generation of UM-BMID. Standard deviation of ROC AUC over the cross validation sets indicated in shaded regions. The optimal number of training epochs was determined to be 105.

The ROC AUC, diagnostic accuracy, sensitivity, and specificity of the trained logistic regression and CNN classifiers on the test of the first generation of UM-BMID are displayed in Fig. 4.4.

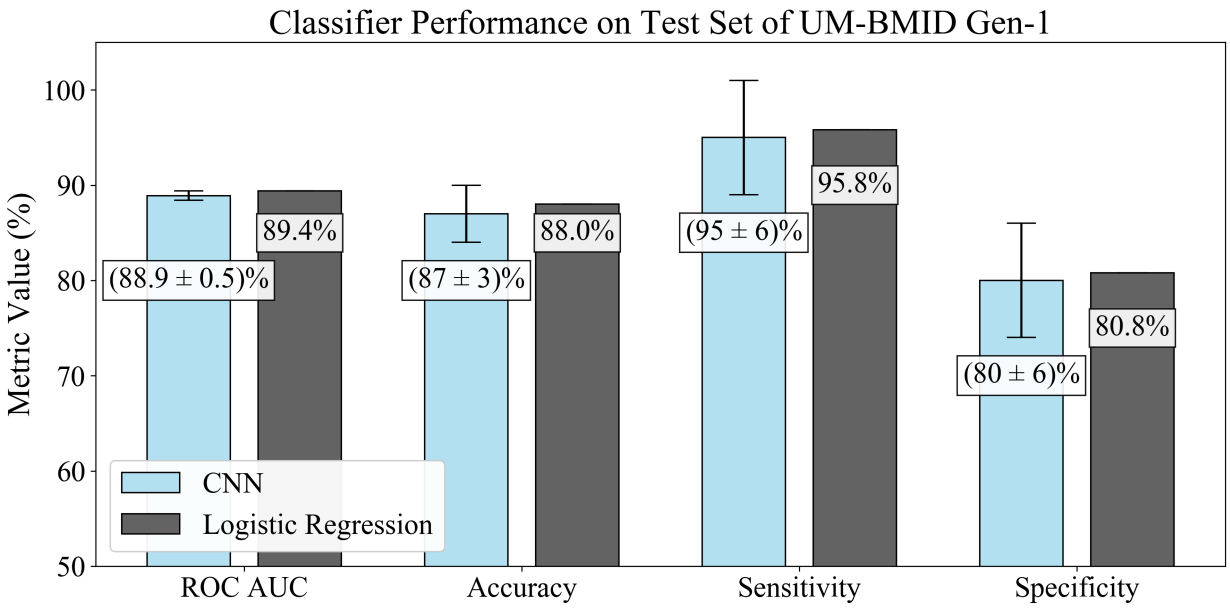


Figure 4.4: Diagnostic performance of logistic regression and CNN classifiers on test set of first generation scans of UM-BMID.

Both classifiers obtained promising results and the achieved ROC AUCs were in agreement, with the CNN obtaining an ROC AUC of $(88.9 \pm 0.5)\%$. Both classifiers performed significantly better than a random classifier, indicating both methods were able to learn a relationship between the input sinograms and the output tumor-detection label. These initial promising results prompted the development of the second generation of breast phantoms (Fig. 2.3) and UM-BMID.

4.3.2 Classifier Performance on UM-BMID Gen-2

The ROC AUC, diagnostic accuracy, sensitivity, and specificity of the trained logistic regression and CNN classifiers on the test of the second generation of UM-BMID are displayed in Fig. 4.5.

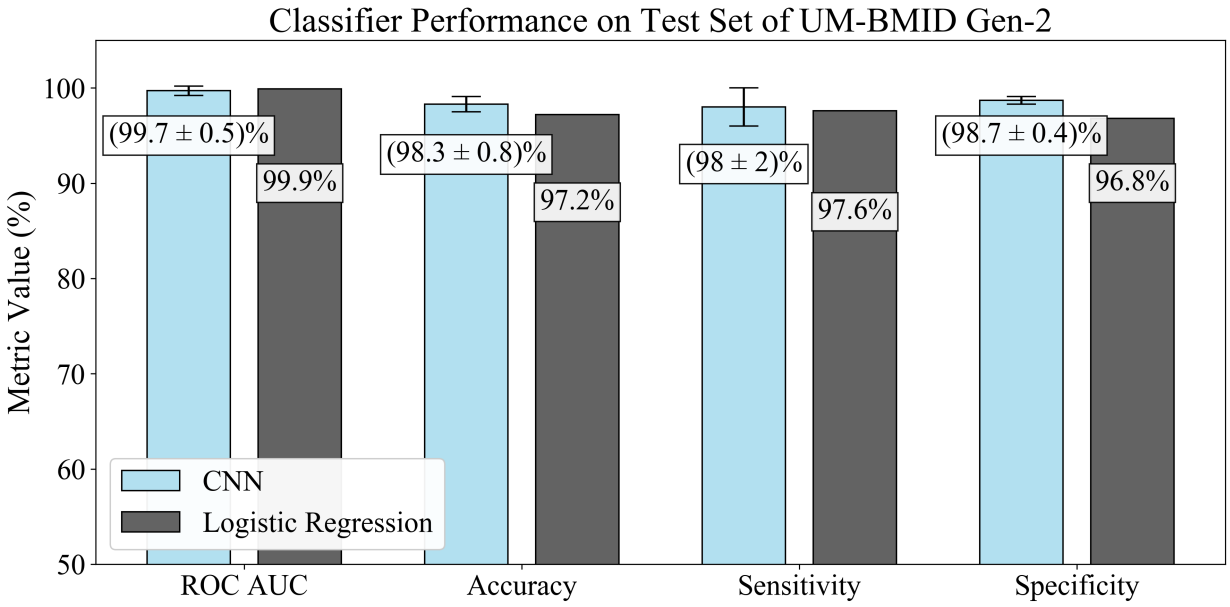


Figure 4.5: Diagnostic performance of logistic regression and CNN classifiers on test set of second generation scans of UM-BMID.

While the results in Fig. 4.5 may appear promising, no optimal number of training epochs or value of regularization weight C were obtained during the grid-search cross-validation. No degradation in cross-validation performance was observed as the number of training epochs was increased from 5000 to 10000 when training the CNN, with the validation ROC AUC above 99% over that range. The best-performing inverse of the regularization weight, C, when training the logistic regression classifier was 10^{23} (corresponding to a regularization weight of 10^{-23}), indicating no model regularization was the best-performing scenario. These troubling results warranted further analysis and investigation.

4.4 Discussion

4.4.1 Interpretation of Results and Limitations

The results presented in Fig. 4.4 indicated that machine learning models were a promising approach to automated tumor-detection in BMS. However, troubling results were obtained after using the machine learning algorithms with a larger dataset (Fig. 4.5). The high AUC scores (greater than 99%) obtained by both the logistic regression and CNN models indicate that the models may have overfit. To further investigate this possibility, these models were trained using the second generation of UM-BMID and tested with the data from the first generation. While there are differences between the two generations (phantom material, phantom coating, and presence of second antenna in the second generation), none of these differences are expected to significantly affect the measured S_{11} data. The performance of the algorithms (trained on the second generation dataset) on the first generation dataset provides a measurement of the generalizability of the models. This performance is displayed in Fig. 4.6.

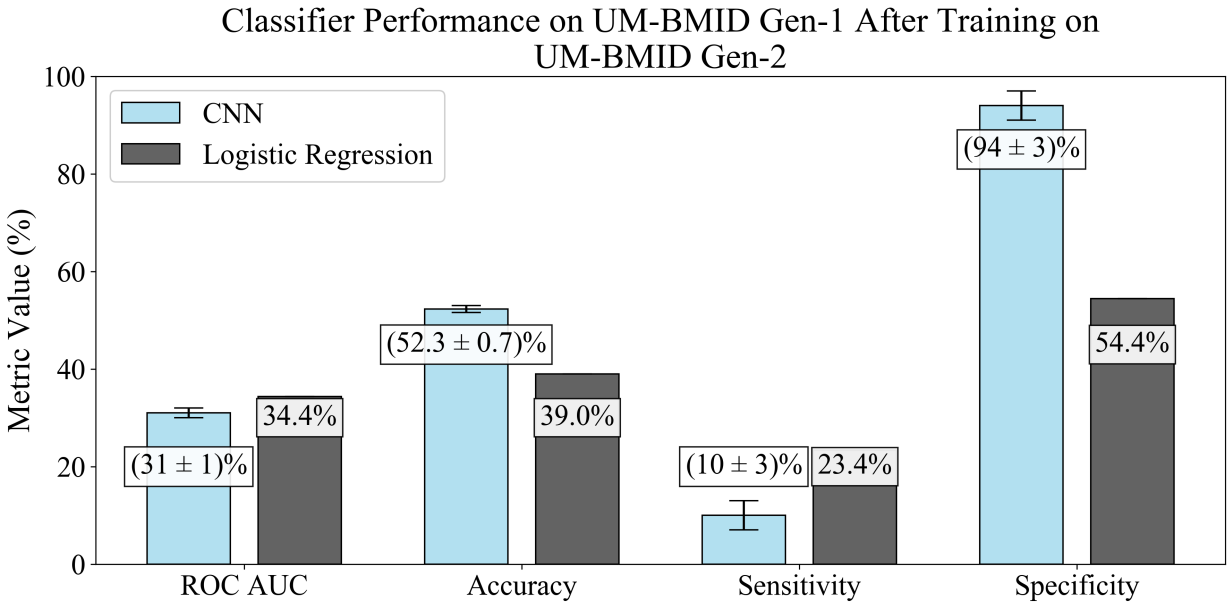


Figure 4.6: Diagnostic performance of logistic regression and CNN classifiers on first generation of UM-BMID after training on second generation of UM-BMID.

The results in Fig. 4.6 indicate that the models trained with the second generation dataset learn a relationship which results in worse-than-random performance on the first generation dataset. This indicates the models did not learn a relationship that can be generalized to unseen data and overfit on the training set. Similar performance was observed if the models were trained on the first generation dataset and evaluated with the second generation dataset.

The high performance obtained in Fig. 4.5 must be reconciled with the poor model generalization observed in Fig. 4.6. While the test set used to evaluate the model and produce the performance metrics displayed in Fig. 4.5 consisted of samples that were not seen by the classifiers during training or hyperparameter tuning, the classifier was still able to obtain an ROC AUC of over 99% on this test set. This may be due to the limited diversity between the training and testing sets. Although the second generation of UM-BMID was designed so that no two scans were the same with respect to several important parameters (described in Section 2.2.3), the 1008 scans of 66 unique breast phantoms resulted in approximately 15 scans of each adipose-fibroglandular shell combination, and 112 scans of each adipose shell. The adipose shell geometry determines the largest measured reflections (occurring at the air-phantom interface), and so the data collected in the 112 scans of each adipose shell are expected to have a high degree of similarity. Despite the efforts to maximize data diversity in UM-BMID, the number of unique phantoms ultimately limits the diversity of the dataset, and the model generalizability must be improved.

To improve the model generalizability, three techniques were investigated. These techniques were selected to increase the sample-to-feature ratio (SFR) or to reduce the model complexity. The SFR can be improved by reducing the dimensionality of the feature space. This was addressed using a novel data representation - the reduced sinogram - and through data augmentation strategies to synthetically increase the size of the dataset. To reduce the model complexity, a simpler CNN architecture was investigated. The following three subsections present these methods and discuss the results obtained with these techniques.

4.4.2 Reducing the Dimensionality of the Feature Space

Using the 35×72 sinogram representation of the scan data results in 2520 features describing each sample. Even in the second generation of UM-BMID, which consists of 1008 samples, this results in a SFR of 0.4. With an SFR < 1, machine learning models are likely to overfit. The SFR could be improved by performing more phantom scans, but this costs considerable experimental time and, given the present number of unique phantoms, would not introduce significantly greater diversity into the training dataset. Alternatively, a different data representation could be used.

To increase the SFR, a narrower time window was applied, retaining only 30 points in the time domain. To further increase the SFR, each of these 30×72 sinograms were split into twelve reduced sinograms, each of shape 30×6. The i^{th} reduced sinogram was defined as

$$\mathbf{S}_i = \begin{bmatrix} \mathbf{s}_i & \mathbf{s}_{i+12} & \mathbf{s}_{i+24} & \dots & \mathbf{s}_{i+60} \end{bmatrix}, \; i = 0, 1, ..., 11, \tag{4.1}$$

where $\mathbf{s}_m$ is time-domain radar signal measured at the m^{th} antenna position in the original sinogram.

The reduced sinogram representation maintains the locality that is inherent to the sinogram structure, albeit with a larger polar angle separation between adjacent antenna positions (4.9° in the original, ≈ 58.8° in the reduced sinogram). This representation results in an SFR of 67.2 with the second generation dataset through increasing the number of individual samples by a factor of 12 and reducing the dimensionality of the feature space from 2520 dimensions to 180 dimensions.

4.4.3 Data Augmentation Strategies

Data augmentation was the second technique used to improve the SFR. Data augmentation methods generate synthetic samples from measured samples within the dataset. Two augmentation strategies were used to synthetically increase the size of the dataset and were employed on the training set. Horizontal reflection of each sinogram was used to double the size of the dataset. The

horizontal reflection of each sinogram $\mathbf{S}$ produced the augmented sample $\mathbf{S}^{ref}$,

$$\mathbf{S}^{ref} = \begin{bmatrix} \mathbf{s}_{71} & \mathbf{s}_{70} & \mathbf{s}_{69} & \dots & \mathbf{s}_{1} & \mathbf{s}_{0} \end{bmatrix}, \tag{4.2}$$

where $\mathbf{s}_m$ is the m^{th} time-domain radar signal.

This horizontal reflection corresponds to having physically scanned a phantom with its tissue structure geometry having been reflected (with respect to the y-axis in the imaging chamber, as indicated in the reconstructions in Fig. 3.7). This augmentation synthetically doubled the size of the dataset and therefore doubled the SFR.

Horizontal translation was also used to generate augmented samples. Five synthetic translated samples were generated from each sample in the dataset, after having generated the horizontally-reflected augmented samples. The j^{th} translated sample produced from each sinogram was defined as

$$\mathbf{S}_j^{trans} = \begin{bmatrix} \mathbf{s}_{[(10j) \bmod 72]} & \mathbf{s}_{[(1+10j) \bmod 72]} & \cdots & \mathbf{s}_{[(71+10j) \bmod 72]} \end{bmatrix}, \quad j = 0, 1, ..., 5. \tag{4.3}$$

The augmented samples generated from this operation are equivalent to the scan data that would have been obtained if the phantom had been scanned after having been rotated through a polar angle of $(49j)^\circ$. This augmentation strategy synthetically increased the number of samples by a factor of six. This augmentation was employed after horizontal reflection augmentation was applied. After both augmentation methods, the SFR was increased by a factor of 12.

The effects of data augmentation in combination with the reduced sinogram structure were also examined. When the two methods were used together, data augmentation strategies were applied to the dataset before the reduced sinogram structure was applied. Table 4.4 displays the effects of both data augmentation and the reduced sinogram structure to the SFR of the dataset.

Table 4.4: Effects of Sinogram Reduction and Data Augmentation on UM-BMID Gen-2

	Full Sinogram Representation, No Augmentation	Full Sinogram Representation, Augmentation	Reduced Sinogram Representation, Augmentation
Number of Samples	1008	12096	145152
Number of Features	2520	2520	180
SFR	0.4	4.8	806.4

4.4.4 Revisiting Model Architecture Selection

To further reduce the possibility of overfitting, the complexity of the CNN model was reduced. This simplified architecture was:

- Input (30×6 reduced sinogram or 35×72 full sinogram)
- Convolutional layer (8 filters, each 3×3 with relu activation)
- Max pooling layer (7×1 kernel)
- Dense output layer (2 neurons with softmax activation)

This model has lower complexity due to the smaller number of filters in the convolutional layer and increased regularization due to the more aggressive max pooling filter size along the time-domain axis of the sinogram.

4.4.5 Evaluation of Model Generalization

The effects of each of the three aforementioned methods aimed at improving the model generalization were evaluated by training the classifier on the second generation of UM-BMID and testing on the first generation. Table 4.5 displays the ROC AUC obtained with the CNN models on the first generation of UM-BMID after using the possible combinations of the three model generalization techniques.

Table 4.5: Effects of Techniques to Improve Model Generalization on CNN Model Performance

Data Representation	Model Architecture	Data Augmentation	ROC AUC (%)
Full Sinogram	CNN	None	31 ± 1
Full Sinogram	CNN	Full Augmentation	60 ± 2
Full Sinogram	Simplified CNN	None	55 ± 4
Full Sinogram	Simplified CNN	Full Augmentation	76 ± 3
Reduced Sinogram	CNN	None	56.6 ± 0.7
Reduced Sinogram	CNN	Full Augmentation	54 ± 2
Reduced Sinogram	Simplified CNN	None	70 ± 2
Reduced Sinogram	Simplified CNN	Full Augmentation	72 ± 4

The use of data augmentation with the simplified CNN model resulted in the highest ROC AUC, albeit not significantly higher than the ROC AUC achieved when using the reduced sinogram data representation with the simplified CNN and data augmentation. Data augmentation was required for better-than-random classifier performance with the full sinograms but had no significant effect when used with the reduced sinogram data structure.

Each individual sample using the reduced sinogram data representation contains only $\frac{1}{12}$ of the radar signals contained in each full sinogram sample. This reduction in feature-space dimensionality comes at the cost of also reducing the information contained in the sample features. As can be seen in the sinogram displayed in Fig. 4.2, the response of a scattering object is largest at the measurement position nearest to the scattering object. This may cause the reduced sinograms that do not contain the radar signals measured nearest the tumor position to present a more difficult tumor-detection scenario.

The simplified CNN architecture resulted in significantly improved diagnostic performance when using either the full sinogram or reduced sinogram data representations, indicating that appropriate model design is necessary for viable classifier performance. Further work may address model architecture selection in greater depth to identify a best-performing architecture.

Data augmentation did have a significant effect on the diagnostic performance of the CNN

when used with the full sinogram data representation. Two data augmentation techniques were employed, and to investigate the effects of each separately, the evaluation procedure was repeated using each technique individually. The results from this are displayed in Fig. 4.7.

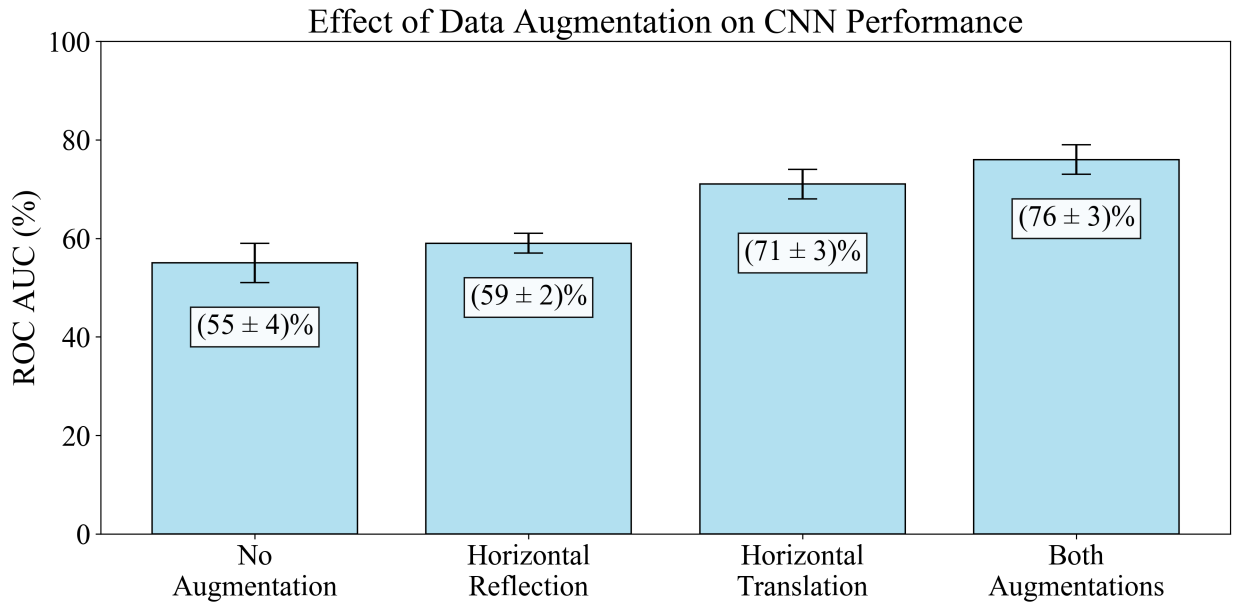


Figure 4.7: Effects of data augmentation strategies on the diagnostic performance of CNN classifier on first generation of UM-BMID after training on second generation of UM-BMID.

The results in Fig. 4.7 indicate that both data augmentation techniques improved classifier performance (although horizontal reflection did not significantly increase the ROC AUC when used without horizontal translation), and that the best performance was obtained when both techniques were used. Data augmentation strategies have not been employed in past applications of machine learning in breast microwave sensing and the results obtained here indicate that these strategies are necessary for obtaining viable classifier performance, even when using a relatively large experimental dataset.

A second method was used to evaluate the generalizability of the trained model. Because the adipose shell determines the strongest measured reflections (i.e., the air-phantom interface reflections), the adipose shell ID is hypothesized to be a significant factor in the dataset diversity. To maximize the diversity between the training and testing datasets, the simplified CNN model

was trained (with full data augmentation) on the full sinograms obtained from scans of all but one adipose shell and was evaluated on the sinograms obtained from the scans of the phantoms of the left-out adipose shell. These results are displayed in Fig. 4.8.

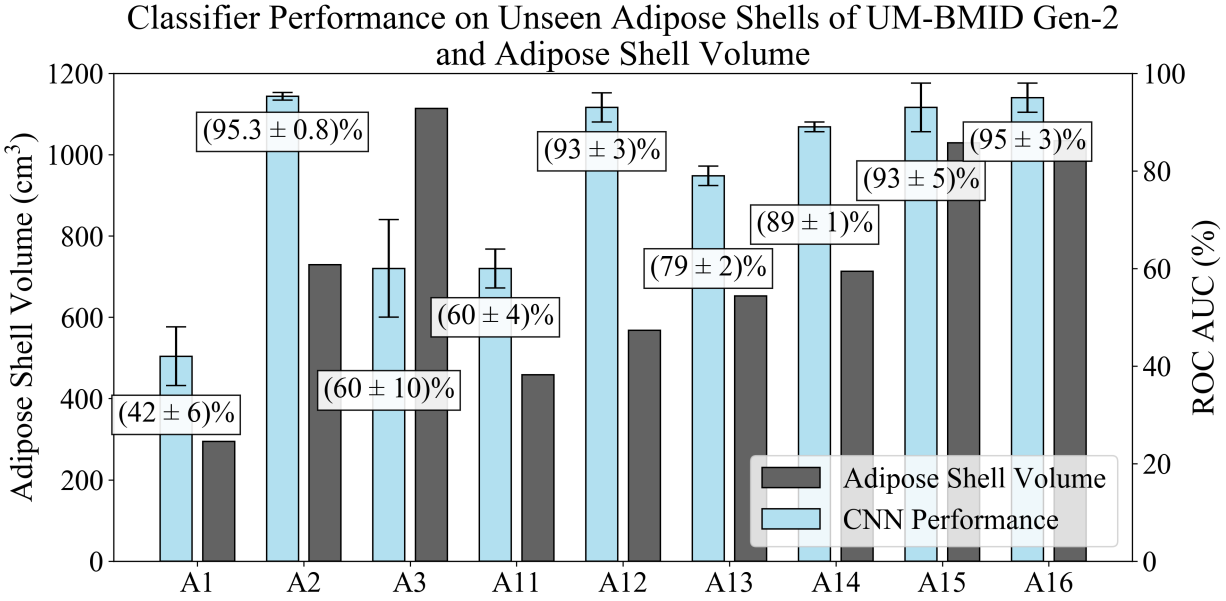


Figure 4.8: Diagnostic performance of the (simplified) CNN classifier on each adipose shell after training on scans of all phantoms excluding that adipose shell. Full data augmentation was used during training. Adipose shell volume also displayed for reference.

The classifier performances in Fig. 4.8 vary widely, with the classifier performing no better than random when testing on the A1 or A3 adipose shells. Notably, the A1 shell was the smallest shell in the phantom array by volume, and the A3 phantom shell was the largest. It should also be noted that the first generation dataset used only the shells A1, A2, and A3. These results may indicate that a more diverse array of phantoms with respect to adipose shell (or, more generally, breast shape) is required to improve classifier generalizability.

The average ROC AUC obtained by the CNN across all test adipose IDs was (78 $\pm$ 4)%. This value is in agreement with the ROC AUC of (76 $\pm$ 3)% obtained after training on the second generation of UM-BMID and testing on the first generation. This agreement indicates that this value may be an accurate estimate of the ability of the trained CNN to generalize to unseen data. This ROC AUC is significantly better than that obtained with a random classifier, and while there

is room for improvement, this value is a first estimate of the diagnostic performance of machine learning models for tumor-detection in experimental data. Given the range of the ROC AUC obtained in Fig. 4.8, machine learning models may have the potential to obtain ROC AUC scores above 95%, but a diverse array of phantoms are required for this evaluation.

If the A1 (smallest in dataset) and A3 (largest in dataset) shells are excluded from this analysis, the average ROC AUC across the remaining adipose shells was (86 $\pm$ 3)%. This is an estimate of the potential diagnostic performance of the technique when evaluated on breast phantoms that are within the breast volume bounds of the training set. The two smallest shells, A1 and A11, presented the greatest challenge to the classifier. This may have been due to the fact that in 64.3% of the scans of these two phantoms, the tumors were not positioned in the same vertical plane as the antennas, due to the limited chest-wall-to-nipple length of the phantoms. One limitation of UM-BMID is that the scans were performed with only one vertical antenna position and additional vertical measurement positions may be useful for classification purposes. If the two smallest shells (A1 and A11) and the largest shell (A3) are excluded from the analysis, then the average ROC AUC was (91 $\pm$ 2)%. This is an estimate of the diagnostic performance of the classifier when the testing set is constrained to consist of phantoms with breast volumes that are within the breast volume bounds of the training set and when the tumor is located at the same vertical position as the antennas.

The results in Table 4.5 demonstrate that a CNN classifier can obtain an ROC AUC of (76 $\pm$ 3)%. A similar analysis was performed using a logistic regression classifier, but neither data augmentation nor the reduced sinogram representation resulted in a logistic regression classifier that obtained an ROC AUC greater than 50%. The diagnostic results obtained with a logistic regression classifier are compared to those obtained with a CNN when evaluated using the first generation dataset after training on the second generation dataset are displayed in Fig. 4.9.

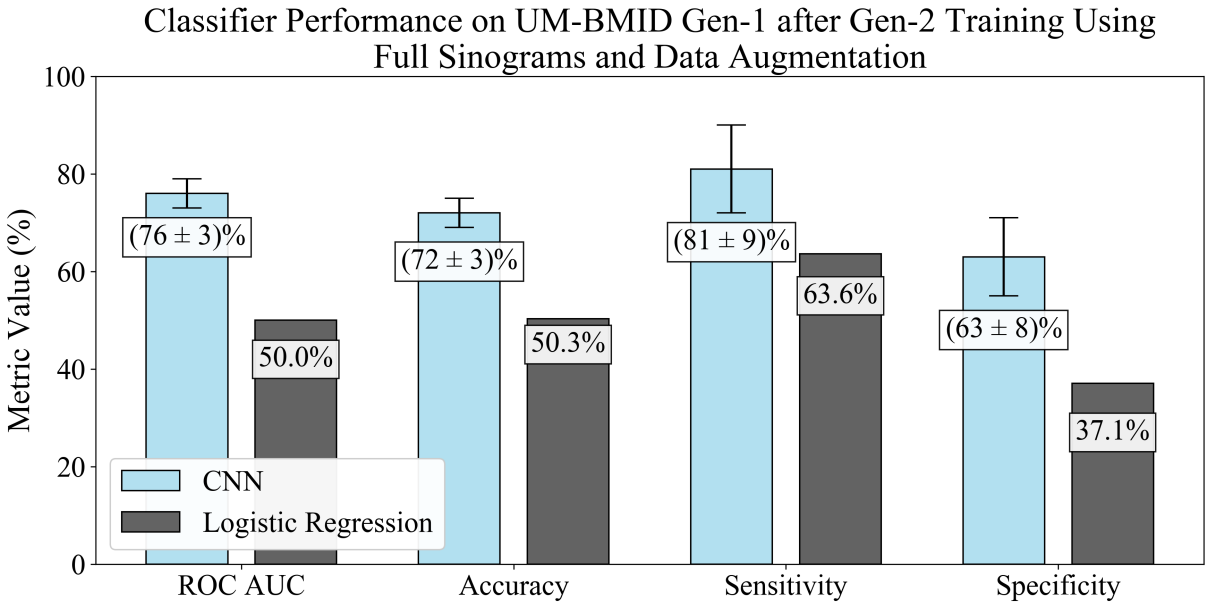


Figure 4.9: Diagnostic performance of logistic regression and CNN classifiers on first generation of UM-BMID after training on second generation of UM-BMID when using the full sinogram data representation, data augmentation strategies, and the simplified CNN architecture.

These results indicate that sophisticated machine learning algorithms are required for tumor-detection, and that shallow learning approaches (i.e., the logistic regression classifier) are not viable. To determine if the CNN was able to make use of the inherent locality of the sinogram data structure, a dense neural network (DNN) was also employed. The architecture of the DNN was:

- Input (30×6 reduced sinogram or 35×72 full sinogram)
- Dense layer (16 neurons, relu activation)
- Dense layer (16 neurons, relu activation)
- Dense output layer (2 neurons with softmax activation)

No approach using the DNN was able to achieve an ROC AUC greater than 50% when evaluated on the first generation dataset after training on the second generation dataset. These results indicate that the CNN was able to utilize the inherent locality of the sinogram data structure for

tumor detection, as the CNN was the only classifier observed to obtain diagnostic performance that was significantly better than random.

4.4.6 Viability of Machine Learning for Automated Tumor Detection Compared to Image-based Detection in Breast Microwave Sensing

This work presents the largest-scale experimental investigation into the viability of machine learning for automated tumor-detection in the published breast microwave sensing literature to-date. The open-access dataset used in this investigation (available at `https://bit.ly/UM-bmid`) is the largest experimental dataset in the literature to-date by an order of magnitude, and 66 unique breast phantoms were used to construct the dataset. Despite the efforts to maximize data diversity, overfitting was observed without the use of data augmentation, and the similarity between phantom scans required two unique methods for evaluating the generalizability of the classification techniques.

The use of data augmentation and a simplified CNN architecture were observed to improve model generalizability and the diagnostic performance of the CNN for tumor-detection in the air-based BMS system is estimated to be between $(78 \pm 4)\%$ and $(91 \pm 3)\%$, where the upper estimate is obtained when the testing set is constrained to consist of phantoms with breast volumes that are within the breast volume bounds of the training set and when the tumor is located at the same vertical position as the antennas. These results are promising, and the upper estimate is competitive with estimates of the ROC AUC in mammography with and without machine learning supports (estimated ROC AUCs of 89% and 87% respectively) from a 2019 study of 240 mammograms from the USA and Europe [117]. Machine learning models in mammography have obtained ROC AUCs between 69.2–97.8% [118], and the results obtained in this work form a promising first step into machine learning -based diagnosis in BMS.

However, several challenges remain when using machine learning methods for automated tumor detection in BMS. Results obtained with one system or set of phantoms may not be applicable

to other systems or phantoms (as seen in Fig. 4.6). Machine learning methods are also often used as black box techniques and understanding the classification predictions can be challenging. Image-based tumor detection allows for more transparent classification, and, ideally, radar-based image reconstruction techniques should be robust to system-specific parameters (choice of coupling medium, system bandwidth, antennas, etc.) or should be able to accommodate system-specific parameters (as in the itDAS algorithm presented in Chapter 3).

A comparison between the diagnostic performance of image-based detection with current beamforming techniques and machine learning methods is warranted. To estimate the diagnostic performance of image-based techniques, the SCR and localization error of reconstructions produced by the DAS, DMAS, and itDAS beamformers were used to obtain an objective image-based detection criterion.

To determine whether a tumor was detected in an image, the SCR (defined in Eq. 3.8) was compared to a threshold value. If the SCR of the image was above the threshold, the image was annotated as having a detected tumor. If the SCR was below the threshold, the image was annotated as having not detected the presence of a tumor. To determine if a detected tumor was a true tumor, the localization error of the image was determined (defined in Eq. 3.10). If the localization error was below a threshold value, the image was annotated as a true-positive. If the localization error was above a threshold value (indicating the detected tumor-response occurred outside of the expected tumor region), the image was annotated as a false-positive. For the purposes of this initial investigation, the localization error threshold was set to 20 mm and the SCR threshold was treated as a variable decision threshold. This approach is similar to that used in [52].

The reconstructions produced by the DAS, DMAS, and itDAS beamformers on the dataset of 36 phantom scans presented in Chapter 3 were used to estimate the sensitivity and specificity of each reconstruction method at 100 linearly-spaced SCR thresholds between 0 dB and 10 dB. Table 4.6 displays the ROC AUC achieved when all reconstructions were examined and when either 5 mm radius tumors were excluded or when both 5 mm radius and 10 mm radius tumors

were excluded.

Table 4.6: Comparison of Image-based Detection by DAS, DMAS, and itDAS

Beamformer	ROC AUC (%) Using All Scans	ROC AUC (%) Excluding 5 mm Tumors	ROC AUC (%) Excluding 5 mm and 10 mm Tumors
DAS	35 ± 1	49 ± 2	68.5 ± 0.6
DMAS	35.4 ± 0.4	49.4 ± 0.6	69.8 ± 0.6
itDAS	40.3 ± 0.4	52.8 ± 0.3	71.6 ± 0.1

These results demonstrate the current challenges in image-based tumor-detection using both literature standard techniques and the novel itDAS beamformer. While the itDAS beamformer outperformed the literature standard methods, all image-based tumor-detection approaches performed worse than even the lower-bound estimate of $(76 \pm 3)\%$ for machine learning approaches. Additionally, it is clear that image-based detection is dependent on tumor size. Machine learning methods are also expected to be dependent on tumor size (and on other factors, including breast size, breast density, and tumor position), and future work can investigate the diagnostic performance of machine learning methods as a function of these variables.

This brief estimation of the ROC AUC of image-based tumor detection methods is limited due to the choice of localization error threshold and the use of a tumor-detection criteria that requires *a priori* knowledge of the tumor location. Additionally, it was performed on a smaller dataset (36 total phantoms cans, 9 of which did not contain a tumor). Future work can examine the performance of image-based detection using the entirety of UM-BMID.

Despite these limitations, the challenges present in image-based tumor detection in breast microwave sensing are clear. This work demonstrates that machine learning approaches are a viable alternative, achieving higher diagnostic performance and allowing for automated diagnosis that does not require *apriori* information regarding the tissue geometry.

4.5 Conclusions

This chapter demonstrates the potential diagnostic viability of machine learning methods for automated tumor-detection in breast microwave sensing using a large experimental open-access dataset. The dataset consisted of scans of MRI-derived breast phantoms, and data diversity was obtained by ensuring no two phantom scans were identical with respect to key phantom parameters relating to the tissue geometry. Despite these efforts to maximize data diversity, overfitting was observed when using both CNN and logistic regression classifiers for tumor-detection. Initial model generalizability was poor, as the ROC AUC obtained when testing the models on the first generation of UM-BMID after training on the second generation was less than 50%.

Three techniques were explored to improve model generalizability. An alternative data representation was used - the reduced sinogram - which reduced the dimensionality of the feature space from 2520 to 180 dimensions. Two data augmentation strategies were employed (horizontal reflection and translation of the sinograms) to synthetically increase the size of the dataset by a factor of 12, and a simplified CNN architecture was used. While all techniques resulted in improved model generalization, the best-performing approach was a combination of data augmentation strategies and the simplified CNN architecture. The diagnostic performance of the CNN was estimated to be between $(76 \pm 3)\%$ and $(91 \pm 3)\%$, where the upper estimate is obtained when the testing set is constrained to consist of phantoms with breast volumes that are within the breast volume bounds of the training set and when the tumor is located at the same vertical position as the antennas. The performance of a CNN under these conditions was compared to that of a logistic regression classifier and a dense neural network. Only the CNN was found to obtain better-than-random classification performance, indicating that the inherent locality of the sinogram data representation can be exploited for tumor-detection purposes.

This work demonstrates the viability of machine learning techniques for automated tumor detection in an air-based breast microwave sensing system. A brief comparison was made to image-

based tumor detection techniques using reconstructions produced by the DAS, DMAS, and it-DAS beamformers. The machine learning models used in this work significantly outperformed the reconstruction methods. The promising results presented herein are the first using a large experimental dataset for tumor-detection in breast microwave sensing and demonstrate the potential diagnostic utility of machine learning methods in breast microwave sensing for automated tumor detection.

5. Conclusions

Breast microwave sensing (BMS) is an emerging modality that has the potential to be used as a breast cancer screening technique. Research in BMS has been ongoing for over two decades but challenges remain before the modality is suitable for clinical use. Improvements to tumor-detection methods are required in both image-based and algorithmic diagnosis methods. This thesis presents novel improvements in image reconstruction and machine learning methods - the two primary methods for tumor-detection in breast microwave sensing. This thesis aims to address the challenge of tumor-detection in BMS through the development of the largest (by an order of magnitude) experimental dataset available in the published literature to-date, the development of a novel image reconstruction algorithm that can accommodate system-specific effects and model more of the physics of microwave imaging, and through an investigation into the application of convolutional neural networks with the measured sinograms for automated tumor-detection.

The development of the University of Manitoba Breast Microwave Imaging Dataset (UM-BMID) represents not only the largest published experimental dataset to-date, but also, to the best of our knowledge, the only open-access dataset (available at `https://bit.ly/UM-bmid`). Chapter 2 of this thesis described the development of UM-BMID using our groups air-operated radar-based breast microwave imaging system and the array of MRI-derived breast phantoms developed by our group. This chapter also presented an initial investigation into the potential viability of machine learning methods for automatic tumor-detection in BMS. The logistic regression classifier obtained a promising ROC AUC of $(94.4 \pm 0.5)\%$ which was in agreement with the results obtained in past studies of the diagnostic performance of machine learning methods with simulated BMS systems. This initial investigation demonstrated one use of UM-BMID and Chapters 3-4 of this thesis use the dataset for further analysis. UM-BMID contains the data from 1257 scans of

MRI-derived phantoms, the .stl files used to 3D-print the individual phantoms, and extensive metadata from each scan.

The third chapter of this thesis used a subset of the data contained in UM-BMID to examine the effects of the inverse discrete Fourier transform (IDFT) and the inverse chirp z-transform (ICZT) for frequency-to-time domain transformation on radar-based image reconstruction. The IDFT was observed to produce reconstructions with prominent circular artifacts while the ICZT-obtained images did not contain these artifacts, and, in one phantom scan, the ICZT-obtained image contained an identifiable tumor response while the IDFT-obtained image did not. The ICZT allows for an arbitrary time-step size used to represent the time-domain radar signals and an investigation into the optimal time-step size was performed. A time-step size of 11 ps was found to be sufficient for both artifact reduction and tumor-detection.

Chapter 3 also presented two novel image reconstruction algorithms, the iterative delay-and-sum (itDAS) and the iterative delay-multiply-and-sum (itDMAS) beamformers. These iterative methods were compared to the standard delay-and-sum (DAS) and delay-multiply-and-sum (DMAS) methods using a subset of UM-BMID. The iterative algorithms were observed to consistently produce reconstructions with higher contrast than the standard beamformers, with the largest increase observed in BI-RADS Class III heterogeneously dense phantoms, where the average contrast was increased by as much as 249% when compared to the DAS beamformer. The itDAS algorithm also has the advantage of allowing for the incorporation of correction factors that improve upon the radar signal model used in the literature-standard approaches. Three correction factors were investigated in this work. These factors modeled the beam pattern of the antennas used in our system, the frequency-dependent gain of the antennas, and the output pulse of the VNA used in the system. While the beam pattern correction did not result in measurable improvements to image quality, modeling the frequency-dependent gain of the antennas did improve contrast, albeit not significantly. Modeling the output pulse of the VNA did consistently and significantly improve the image contrast. While only three correction factors were investigated in this work, the itDAS algorithm allows for further corrections, allowing for components of the physical model of microwave

imaging to be implemented and analyzed individually.

Chapter 4 examined the application of machine learning methods for tumor-detection in BMS. This is the first investigation into the diagnostic performance of machine learning methods in breast microwave sensing using an experimental dataset containing data from more than 150 phantom scans. This work was also the first in the published literature to examine the use of convolutional neural networks (CNNs) with the sinogram representation of the measured scan data. Despite the large and relatively diverse dataset, overfitting was observed to be a challenge, and poor model generalization was observed. While no two scans in UM-BMID were identical with respect to key phantom and geometric parameters, the use of only 66 unique phantoms to generate 1008 scans in the second generation dataset resulted in a relatively high degree of data similarity. Three techniques to reduce the observed overfitting and to improve model generalization were analyzed. The use of a simplified CNN architecture, a reduced sinogram data representation, and data augmentation strategies were used for this purpose.

While all three techniques improved model generalization, the best-performing strategy used data augmentation and the simplified CNN architecture. The use of the reduced sinogram representation improved performance when compared to the results obtained before any techniques were applied to improve model generalization, but the reduced sinogram model used 180 features to represent each sample, compared to the 2520 features used in the full sinogram representation. This reduction in feature space dimensionality is useful for improving the sample-to-feature ratio but resulted in a more challenging tumor-detection scenario due to the reduced information used to describe each sample. The ROC AUC of the simplified CNN when trained using data augmentation strategies is estimated to be between $(76 \pm 3)\%$ and $(91 \pm 3)\%$, where the upper estimate is obtained when the testing set is constrained to consist of phantoms with breast volumes that are within the breast volume bounds of the training set and when the tumor is located at the same vertical position as the antennas. The performance of the CNN was compared to that of a logistic regression classifier and a dense neural network, and only the CNN was found to obtain results that were significantly better than those of a random classifier. These results indicate that the CNN ar-

chitecture can exploit the inherent locality of the sinogram data representation for tumor-detection.

This thesis demonstrates the feasibility of machine learning methods for automated tumor-detection in an air-based BMS system using experimental data from scans of MRI-derived phantoms. A brief comparison between the diagnostic performance of image-based tumor detection using the DAS, DMAS, and itDAS beamformers and that obtained with the machine learning methods was performed. The machine learning methods significantly outperformed the image-based tumor detection methods. These results demonstrate the challenges present in image-based detection in BMS. While the itDAS beamformer described in Chapter 3 significantly outperforms the literature-standard techniques, more sophisticated image-based detection criteria and reconstruction methods are required for image-based diagnosis in BMS to be clinically viable. The itDAS reconstruction method has the advantage of allowing for the incorporation of correction factors that can significantly affect image quality (as observed herein when correcting for the output pulse of the VNA), and future work investigating correction factors for the inhomogeneous propagation speed of the microwave signal, signal attenuation, and dispersion effects may be necessary for image-based methods to be viable. The results obtained with machine learning methods are promising, and this thesis has set the stage for future large-scale analyses in BMS through the development of the first and largest open-access dataset in the literature and through the promising results obtained with the application of CNNs using the sinogram data representation.

A. Appendix

The following Python code contains the implementation of the itDAS beamformer. The implementation is also available at `https://github.com/TysonReimer/itDAS`.

```
1
2  import numpy as np
3
4
5  def back_proj(td_data, pix_angs, pix_dists, prop_speed, ini_t, fin_t,
6          use_dmas=False):
7    """Back-projects time-domain data onto the image-space
8
9    Performs back-projection using time-domain data. Uses either the
10   DAS or DMAS beamformer as its basis.
11
12   Parameters
13   ----------
14   td_data : array_lke
15     The time-domain data (sinogram) that will be back-projected into
16     the image space
17   pix_angs : array_like
18     The angles off of the central axis of the antenna of every
19     pixel, for each antenna position, in degrees
20   pix_dists : array_like
21     The distances between each pixel and the antenna, for each
22     antenna position, in meters
23   prop_speed : float
24     The estimated propagation speed of the microwave signal in m/s
25   ini_t : float
```

```
    The initial time (s) of the td_data (i.e., the first element
    in each radar signal corresponds to the ini_t of response)
  fin_t : float
    The final time (s) of the td_data (i.e., the last element in
    each radar signal corresponds to the fin_t of response)
  use_dmas : bool
    If True, uses the delay-multiply-and-sum beamformer as the
    back-projection operator. Otherwise, uses the delay-and-sum
    beamformer

  Returns
  -------
  back_projection : array_like
    The back-projection, in the image-space, of the td_data
  """

  td_data = np.abs(td_data)  # Take the abs-value

  # Find the number of points in the time-domain used to represent the
  # signal, and the number of antenna positions
  n_time_pts, n_ant_pos = td_data.shape

  # Find the vector of the time-points used to represent the time
  # domain signal, and the incremental step-size
  scan_times = np.linspace(ini_t, fin_t, n_time_pts)
  scan_time_step = np.abs(scan_times[1] - scan_times[0])

  # Init arr for storing the back-projection from each antenna
  # position
  back_projections = np.zeros_like(pix_angs)

  # Init arr to return
  back_projection = np.zeros(np.shape(pix_angs)[1:])
```

```
59
60  # Find the pixels in front of the antenna, for each antenna position
61  pix_front_of_ant = np.abs(pix_angs) < 90
62
63  # Find the response-times for every pixel
64  pix_times = pix_dists * pix_front_of_ant / prop_speed
65
66  # Find the upper and lower bounds on the time-of-response estimates
67  # for each pixel
68  upper_pix_times = scan_times + 0.5 * scan_time_step
69  lower_pix_times = scan_times - 0.5 * scan_time_step
70
71  # For every antenna position used in the scan
72  for ant_pos in range(n_ant_pos):
73
74    # Find the response times of each pixel, for this antenna
75    # position
76    pix_times_here = pix_times[ant_pos, :, :]
77
78    # For every time-point of response
79    for time_pt in range(np.size(td_data, axis=0)):
80
81      # Find the coordinates of the pixels that correspond to this
82      # time-of-response
83      resp_idxs = np.logical_and(pix_times_here
84                      > lower_pix_times[time_pt],
85                        pix_times_here
86                      < upper_pix_times[time_pt])
87
88      # Get the value that will be back-projected to the pixels at
89      # the resp_idxs
90      back_proj_val = td_data[time_pt, ant_pos]
91
```

```
92        # Back-project the value to the image-space
93        back_projections[ant_pos, :, :][resp_idxs] += back_proj_val
94
95    # If using the DMAS beamformer as the foundation of the
96    # back-projection method
97    if use_dmas:
98
99      # For every antenna position, perform pair-wise signal
100     # multiplication with every other antenna position
101     for ant_pos in range(n_ant_pos):
102       for second_ant_pos in range(ant_pos + 1, n_ant_pos):
103
104         # Perform pair-wise signal multiplication before
105         # summation
106         back_projection += (back_projections[ant_pos, :, :]
107                   * back_projections[second_ant_pos, :, :])
108
109   else:  # Use the DAS as the foundation of the back-projection method
110
111     # Sum the back-projections from each antenna position
112     back_projection = np.sum(back_projections, axis=0)
113
114   return back_projection
115
116
117 def get_roi(roi_rad, m_size, ant_rad):
118   """Return binary mask for central circular region of interest
119
120   Returns a binary mask in which a circular region of interest is set
121   to True and the region outside is set to False
122
123   Parameters
124   ----------
```

```
125   roi_rad : float
126     The radius (in meters) of the inner circular region of interest
127   m_size : int
128     The number of pixels along one dimension used to define the
129     model-space
130   ant_rad : float
131     The radius of the antenna scan trajectory in meters
132   """
133
134   # Get arrays for the x,y positions of each pixel
135   pix_xs, pix_ys = get_xy_arrs(m_size, ant_rad)
136
137   # Find the distance from each pixel to the center of the model space
138   pix_dist_from_center = np.sqrt(pix_xs**2 + pix_ys**2)
139
140   # Get the region of interest as all the pixels inside the
141   # circle-of-interest
142   roi = np.zeros([m_size, m_size], dtype=np.bool)
143   roi[pix_dist_from_center < roi_rad] = True
144
145   return roi
146
147
148 def fwd_proj(img_model, pix_angs, pix_dists, prop_speed, ini_t,
149         fin_t, n_time_pts, ant_rad):
150   """Forward-projects the img_model into the time-domain
151
152   Computes the forward projection of the image_model - projecting
153   from the image-space to the data-domain / sinogram space.
154
155   Parameters
156   ----------
157   img_model : array_like
```

```
    The model of the object in the image-space
  pix_angs : array_like
    The angle off of the central axis of the antenna of each pixel,
    for each antenna position, in degrees
  pix_dists : array_like
    The distances between each pixel and the antenna, for each
    antenna position, in meters
  prop_speed : float
    The estimated propagation speed of the microwave signal, m/s
  ini_t : float
    The initial time-point used to represent the radar signals in
    the time-domain, in seconds (i.e., the first point in the
    fwd_proj corresponds to the ini_t time-of-response)
  fin_t : float
    The final time-point used to represent the radar signals in the
    time-domain, in seconds (i.e., the last point in the
    fwd_proj corresponds to the fin_t time-of-response)
  n_time_pts : int
    The number of points used to represent the radar signals in the
    time-domain
  ant_rad : float
    The radius of the antenna trajectory during the scan

  Returns
  -------
  fwd_projection : array_like
    The forward projection of the image_model in the time-domain
    (i.e., sinogram-space)
  """

  # Find the number of antenna positions used in the scan
  n_ant_pos = pix_angs.shape[0]

```

```
191  # Make the vector representing the time-points of the radar signals
192  # in the time domain
193  scan_times = np.linspace(ini_t, fin_t, n_time_pts)
194
195  # Init arr to return
196  fwd_projection = np.zeros([n_time_pts, n_ant_pos], dtype=np.complex64)
197
198  # Get ROI (within antenna trajectory)
199  roi = get_roi(roi_rad=ant_rad, ant_rad=ant_rad,
200          m_size=np.size(img_model, axis=0))
201
202  # Apply window to set pixels outside of ROI to zero
203  img_model[np.logical_not(roi)] = 0
204
205  # Find the physical width of each pixel in meters
206  pix_dist_width = 2 * ant_rad / pix_angs.shape[0]
207
208  # Convert this physical width to a time-of-response width
209  pix_time_width = pix_dist_width / prop_speed
210
211  # Find the pixels that are in front of the antenna, for each antenna
212  # position
213  pix_in_front_ant = np.abs(pix_angs) < 90
214
215  # Find the response times of every pixel, and the upper and lower
216  # bounds on these estimates
217  pix_times = pix_dists * pix_in_front_ant / prop_speed
218
219  # Find the upper and lower bounds on the time-of-response estimates
220  # for each pixel
221  upper_pix_times = pix_times + 0.5 * pix_time_width
222  lower_pix_times = pix_times - 0.5 * pix_time_width
223
```

```
  # For every antenna position in the scan
  for ant_pos in range(n_ant_pos):

    # For every time-point in the time-domain radar signal
    for time_pt in range(n_time_pts):

      # Find the coordinates of the pixels that correspond to this
      # time_pt time-of-response
      resp_idxs = np.logical_and(scan_times[time_pt]
                      < upper_pix_times[ant_pos, :, :],
                      scan_times[time_pt]
                      > lower_pix_times[ant_pos, :, :])

      # Find the values in the img_model that will be contributing
      # to the forward projection here
      contributing_values = img_model[resp_idxs]

      # Sum the contributing values after applying any correction
      # factors
      fwd_projection[time_pt, ant_pos] += np.sum(contributing_values)

  return fwd_projection


def itdas(td_data, ini_t, fin_t, ant_rad, speed, m_size,
      ini_ant_ang=-130.0, use_dmas=False, n_iters=6):
  """Reconstructs an image of the td_data using the itDAS algorithm

  Uses the itDAS reconstruction algorithm to reconstruct an image.

  Parameters
  ----------
  td_data : array_like
```

```
    The time-domain data obtained from an experimental scan that
    will be used to reconstruct an image of the scanned object
ini_t : float
    The initial time-point used in the sinogram (typically 0 s),
    in seconds
fin_t : float
    The final time-point used in the sinogram (typically 6e-9 s),
    in seconds
ant_rad : float
    The radius of the antennas trajectory during the scan,
    after accounting for phase-delay using apply_ant_t_delay() func
speed : float
    The estimated propagation speed of the signal in the scan, in
    meters/second
m_size : int
    The number of pixels along one dimension to be used when
    reconstructing an image
ini_ant_ang : float
    The angle off of the positive x-axis of the *initial* antenna
    position during the scan
use_dmas : bool
    If True, uses the DMAS beamformer as the back-projection
    operator
n_iters : int
    The number of iterations that will be used to reconstruct the
    image

Returns
-------
img : array_like
    A 2D reconstructed image of the object space
"""

```

```
n_time_pts, n_ant_pos = td_data.shape

# Calculate these arrays once to save computation time
pix_dists, pix_angs = get_pix_dists_angs(m_size, n_ant_pos, ant_rad,
                    ini_ant_ang=ini_ant_ang)

# Initialize image estimate to be a homogeneous map
img = 0.001 * np.ones([m_size, m_size])

# Get the back-projection of a unity matrix in the data domain, for
# normalization purposes
unity_back_proj = back_proj(np.ones_like(td_data), pix_angs,
              pix_dists, speed, ini_t, fin_t,
              use_dmas=use_dmas)

# Get the forward-projection of a unity matrix in the image-speace,
# for normalization purposes
unity_fwd_proj = fwd_proj(np.ones_like(img), pix_angs, pix_dists,
              speed, ini_t, fin_t, n_time_pts, ant_rad)

# Iterate until the set number of iterations has elapsed
for iter_idx in range(n_iters):

  # Compute the forward projection of the current image estimate
  fwd_proj_img = fwd_proj(img, pix_angs, pix_dists, speed,
              ini_t, fin_t, n_time_pts, ant_rad)

  # Normalize the forward projection
  fwd_proj_img /= unity_fwd_proj

  # Compute the ratio between the experimental data and this
  # forward projection
  fwd_proj_ratio = td_data / fwd_proj_img
```

```
323
324     # Back project this ratio into the object space
325     back_proj_ratio = back_proj(fwd_proj_ratio, pix_angs, pix_dists,
326                     speed, ini_t, fin_t, use_dmas=use_dmas)
327
328     # Normalize the back projection
329     back_proj_ratio /= unity_back_proj
330
331     # Update the image estimate by multiplying it with this
332     # back-projected ratio
333     img *= back_proj_ratio
334
335   return img
336
337
338 def get_pix_dists_angs(m_size, n_ant_pos, ant_rad, ini_ant_ang=-130.0):
339   """Returns the distance and angle between each pixel and antenna
340
341   Returns arrays in which each pixel is assigned its distance from the
342   antenna and its angle off of the central axis of the antenna in
343   degrees, for each antenna position used in a scan
344
345   Parameters
346   ----------
347   m_size : int
348     The number of pixels along one dimension used to define the
349     image-space
350   n_ant_pos : int
351     The number of antenna positions used in the scan
352   ant_rad : float
353     The radius of the antenna trajectory during the scan in meters
354   ini_ant_ang : float
355     The initial angle offset (in deg) of the antenna from the
```

```
356     negative x-axis
357
358   Returns
359   -------
360   pix_dists : array_like
361     3D arr in which each pixel is assigned the value corresponding
362     to its distance from the antenna for that antenna position
363     (i.e., for NxMxL arr, N is the number of antenna positions,
364     MxL represents the model space)
365   pix_angs : array_like
366     3D arr in which each pixel is assigned the value corresponding
367     to its angle off of the central angle of the antenna for that
368     antenna position (i.e., for NxMxL arr, N is the number of
369     antenna positions, MxL represents the model space)
370   """
371
372   # Get the antenna x,y positions
373   ant_xs, ant_ys = get_ant_scan_xys(ant_rad, n_ant_pos,
374                     ini_ant_ang=ini_ant_ang)
375
376   # Initialize arrays
377   pix_dists = np.ones([n_ant_pos, m_size, m_size])
378   pix_angs = np.ones_like(pix_dists)
379
380   # Get the x,y positions of every pixel in the model
381   pix_xs, pix_ys = get_xy_arrs(m_size, ant_rad)
382
383   for ant_pos in range(n_ant_pos):
384
385     # Find the x,y-position differences between each pixel and
386     # the antenna for this ant_pos
387     x_diffs = pix_xs - ant_xs[ant_pos]
388     y_diffs = pix_ys - ant_ys[ant_pos]
```

```
389
390     # Convert these x,y-position differences into an absolute
391     # geometric difference
392     pix_dists[ant_pos, :, :] = 2 * np.sqrt(x_diffs**2 + y_diffs**2)
393
394     # Obtain the angles for these pixels
395     pix_angs[ant_pos, :, :] = -np.arctan2(ant_xs[ant_pos] * y_diffs
396                           - ant_ys[ant_pos] * x_diffs,
397                           ant_xs[ant_pos] * x_diffs
398                           + ant_ys[ant_pos] * y_diffs)
399
400   pix_angs = np.rad2deg(pix_angs)
401
402   # Convert the angles so that they have the proper range (pixels
403   # to the left of the antennas central axis have negative angles,
404   # pixels to the right of the antennas central axis have positive
405   # angles; i.e., the central axis of the antenna lies at the
406   # angle 0deg).
407   pix_angs[np.abs(pix_angs) < 90] = 0
408   indexing_array = np.zeros_like(pix_angs)
409   indexing_array[pix_angs < 0] = -1
410   indexing_array[pix_angs > 0] = 1
411   pix_angs[indexing_array == -1] += 180
412   pix_angs[indexing_array == 1] -= 180
413   pix_angs[indexing_array == 0] = 180
414
415   return pix_dists, pix_angs
416
417
418 def get_ant_scan_xys(ant_rad, n_ant_pos, ini_ant_ang=-130.0):
419   """Returns the x,y positions of each antenna position in the scan
420
421   Returns two vectors, containing the x- and y-positions in meters of
```

```
422   the antenna during a scan.
423
424   Parameters
425   ----------
426   ant_rad : float
427     The radius of the trajectory of the antenna during the scan,
428     in meters
429   n_ant_pos : int
430     The number of antenna positions used in the scan
431   ini_ant_ang : float
432     The initial angle offset (in deg) of the antenna from the
433     negative x-axis
434
435   Returns
436   -------
437   ant_xs : array_like
438     The x-positions in meters of each antenna position used in the
439     scan
440   ant_ys : array_like
441     The y-positions in meters of each antenna position used in the
442     scan
443   """
444
445   # Find the polar angles of each of the antenna positions used in the
446   # scan
447   ant_angles = (np.linspace(0, (355 / 360) * 2 * np.pi, n_ant_pos) +
448           np.deg2rad(ini_ant_ang))
449   ant_angles = np.flip(ant_angles)
450
451   ant_xs = np.cos(ant_angles) * ant_rad  # Find the x-positions
452
453   ant_ys = np.sin(ant_angles) * ant_rad  # Find the y-positions
454
```

```
455   return ant_xs, ant_ys
456
457
458 def get_xy_arrs(m_size, ant_rad):
459   """Finds the x/y position of each pixel in the image-space
460
461   Returns arrays that contain the x-distances and y-distances of every
462   pixel in the model.
463
464   Parameters
465   ----------
466   m_size : int
467     The number of pixels along one dimension of the model
468   ant_rad : float
469     The radius of the antenna trajectory during the scan in meters
470
471   Returns
472   -------
473   x_dists : array_like
474     A 2D arr. Each element in the arr contains the x-position of
475     that pixel in the model, in meters
476   y_dists : array_like
477     A 2D arr. Each element in the arr contains the y-position of
478     that pixel in the model, in meters
479   """
480
481   # Initialize the arrays
482   x_coords = np.ones([m_size, m_size])
483   y_coords = np.ones_like(x_coords)
484
485   # Assign each pixel the 1-based index of that pixel
486   for pix in range(m_size):
487     x_coords[pix, :] = pix + 1
```

```
488     y_coords[:, pix] = pix + 1
489
490   # Find the distances for these pixels
491   x_dists = (x_coords - m_size // 2) * 2 * ant_rad / m_size
492   y_dists = -(y_coords - m_size // 2) * 2 * ant_rad / m_size
493
494   return x_dists, y_dists
```

References

[1] D. R. Brenner, H. K. Weir, A. A. Demers, L. F. Ellison, C. Louzado, A. Shaw, D. Turner, R. R. Woods, and L. M. Smith, "Projected estimates of cancer in Canada in 2020," *Canadian Medical Association Journal*, vol. 192, no. 9, pp. E199–E205, 2020.

[2] Canadian Cancer Statistics Advisory Committee, "Canadian cancer statistics 2019." Toronto, ON: Canadian Cancer Society, 2019. Accessed: 2020-04-09.

[3] P. C. Gøtzsche and K. J. Jørgensen, "Screening for breast cancer with mammography," *Cochrane Database of Systematic Reviews*, vol. 22, no. 1469-493X (Electronic), p. CD001877, 2013.

[4] The Canadian Task Force on Preventive Health Care, "Recommendations on screening for breast cancer in average-risk women aged 40-74 years," *Canadian Medical Association Journal*, vol. 183, no. 17, pp. 1991–2001, 2011.

[5] E. Sickles, C. D'Orsi, L. Basset, and *et al*, *ACR BI-RADS®Mammography*. Reston, VA: American College of Radiology, 2013.

[6] P. A. Carney, D. L. Miglioretti, B. C. Yankaskas, K. Kerlikowske, R. Rosenberg, C. M. Rutter, B. M. Geller, L. A. Abraham, S. H. Taplin, M. Dignan, G. Cutter, and R. Ballard-Barbash, "Individual and combined effects of age, breast density, and hormone replacement therapy use on the accuracy of screening mammography," *Annals of Internal Medicine*, vol. 138, no. 3, pp. 168–175, 2003.

[7] K. E. McLean and J. Stone, "Role of breast density measurement in screening for breast cancer," *Climacteric*, vol. 21, no. 3, pp. 214–220, 2018.

[8] B. L. Sprague, R. E. Gangnon, V. Burt, A. Trentham-Dietz, J. M. Hampton, R. D. Wellman, K. Kerlikowske, and D. L. Miglioretti, "Prevalence of mammographically dense breasts in the United States," *Journal of the National Cancer Institute*, vol. 106, no. 10, pp. 1–6, 2014.

[9] L. Irwig, N. Houssami, and C. van Vliet, "New technologies in screening for breast cancer: A systematic review of their accuracy," *British Journal of Cancer*, vol. 90, no. 11, pp. 2118–2122, 2004.

[10] S. C. Hagness, A. Taflove, and J. Bridges, "Two-dimensional FDTD analysis of a pulsed microwave confocal system for breast cancer detection: Fixed-focus and antenna-array sensors," *IEEE Transactions on Biomedical Engineering*, vol. 45, no. 12, pp. 1470–1479, 1998.

[11] N. K. Nikolova, "Microwave imaging for breast cancer," *IEEE Microwave Magazine*, vol. 12, no. 7, pp. 78–94, 2011.

[12] B. M. Moloney, D. O'Loughlin, S. A. Elwahab, and M. J. Kerin, "Breast cancer detection - A synopsis of conventional modalities and the potential role of microwave imaging," *Diagnostics*, vol. 10, no. 2, pp. 1–13, 2020.

[13] E. Fear, P. Meaney, and M. Stuchly, "Microwaves for breast cancer detection?," *IEEE Potentials*, vol. 22, no. 1, pp. 12–18, 2003.

[14] D. O'Loughlin, M. O'Halloran, B. M. Moloney, M. Glavin, E. Jones, and M. A. Elahi, "Microwave breast imaging: Clinical advances and remaining challenges," *IEEE Transactions on Biomedical Engineering*, vol. 65, no. 11, pp. 2580–2590, 2018.

[15] Liewei Sha, E. R. Ward, and B. Stroy, "A review of dielectric properties of normal and malignant breast tissue," in *Proceedings IEEE SoutheastCon 2002*, (Columbia, SC, USA), pp. 457–462, IEEE, 2002.

[16] T. Sugitani, S.-i. Kubota, S.-i. Kuroki, K. Sogo, K. Arihiro, M. Okada, T. Kadoya, M. Hide, M. Oda, and T. Kikkawa, "Complex permittivities of breast tumor tissues obtained from cancer surgeries," *Applied Physics Letters*, vol. 104, no. 25, pp. 1–5, 2014.

[17] M. Solis-Nepote, T. Reimer, and S. Pistorius, "An air-operated bistatic system for breast microwave radar imaging: Pre-clinical validation," in *2019 41st Annual International Conference of the IEEE Engineering in Medicine and Biology Society (EMBC)*, (Berlin, Germany), pp. 1859–1862, IEEE, 2019.

[18] P. M. Meaney, M. W. Fanning, Dun Li, S. P. Poplack, and K. D. Paulsen, "A clinical prototype for active microwave imaging of the breast," *IEEE Transactions on Microwave Theory and Techniques*, vol. 48, no. 11, pp. 1841–1853, 2000.

[19] E. C. Fear, J. Bourqui, C. Curtis, D. Mew, B. Docktor, and C. Romano, "Microwave breast imaging with a monostatic radar-based system: A study of application to patients," *IEEE Transactions on Microwave Theory and Techniques*, vol. 61, no. 5, pp. 2119–2128, 2013.

[20] E. Porter, E. Kirshin, A. Santorelli, M. Coates, and M. Popović, "Time-domain multistatic radar system for microwave breast screening," *IEEE Antennas and Wireless Propagation Letters*, vol. 12, pp. 229–232, 2013.

[21] A. Preece, I. Craddock, M. Shere, L. Jones, and H. L. Winton, "MARIA M4: Clinical evaluation of a prototype ultrawideband radar scanner for breast cancer detection," *Journal of Medical Imaging*, vol. 3, no. 3, pp. 1–6, 2016.

[22] E. Porter, M. Coates, and M. Popovic, "An early clinical study of time-domain microwave radar for breast health monitoring," *IEEE Transactions on Biomedical Engineering*, vol. 63, no. 3, pp. 1–10, 2016.

[23] E. Porter, R. Kazemi, A. Santorelli, and M. Popovic, "Study of daily tissue changes through breast monitoring with time-domain microwave radar," in *2015 9th European Conference on Antennas and Propagation (EuCAP)*, (Lisbon, Portugal), pp. 1–5, IEEE, 2015.

[24] E. Porter, A. Santorelli, and M. Popovic, "Time-domain microwave radar for breast screening: Initial testing with volunteers," in *2014 8th European Conference on Antennas and Propagation (EuCAP)*, (The Hague, Netherlands), pp. 104–107, IEEE, 2014.

[25] E. Porter, A. Santorelli, and M. Popovic, "Time-domain microwave radar applied to breast imaging: Measurement reliability in a clinical setting," *Progress in Electromagnetics Research*, vol. 149, pp. 119–132, 2014.

[26] S. Sasada, N. Masumoto, H. Song, K. Kajitani, A. Emi, and T. Kadoya, "Portable impulse-radar detector for breast cancer: A pilot study," *Journal of Medical Imaging*, vol. 5, no. 2, pp. 1–5, 2018.

[27] H. Song, S. Sasada, T. Kadoya, M. Okada, K. Arihiro, X. Xiao, and T. Kikkawa, "Detectability of breast tumor by a hand-held impulse-radar detector: Performance evaluation and pilot clinical study," *Scientific Reports*, vol. 7, no. 1, pp. 1–11, 2017.

[28] B. R. Lavoie, J. Bourqui, and E. C. Fear, "Metrics for assessing the similarity of microwave breast imaging scans of healthy volunteers," *IEEE Transactions on Medical Imaging*, vol. 37, no. 8, pp. 1788–1798, 2018.

[29] C. Curtis, B. R. Lavoie, and E. Fear, "An analysis of the assumptions inherent to near-field beamforming for biomedical applications," *IEEE Transactions on Computational Imaging*, vol. 3, no. 4, pp. 953–965, 2017.

[30] C. Curtis and E. Fear, "Coherent summation of monostatic radar signals," in *2013 7th European Conference on Antennas and Propagation (EuCAP)*, (Gothenburg, Sweden), pp. 628–629, IEEE, 2013.

[31] B. R. Lavoie, M. Okoniewski, and E. C. Fear, "Estimating the effective permittivity for reconstructing accurate microwave-radar images," *PLOS ONE*, vol. 11, no. 9, pp. 1–25, 2016.

[32] E. Porter, A. Santorelli, R. Kazemi, and M. Popovic, "Microwave time-domain radar: Healthy tissue variations over the menstrual cycle," *IEEE Antennas and Wireless Propagation Letters*, vol. 14, pp. 1310–1313, 2015.

[33] E. Porter, H. Bahrami, A. Santorelli, B. Gosselin, L. A. Rusch, and M. Popovic, "A wearable microwave antenna array for time-domain breast tumor screening," *IEEE Transactions on Medical Imaging*, vol. 35, no. 6, pp. 1501–1509, 2016.

[34] M. Shere, I. Lyburn, R. Sidebottom, H. Massey, C. Gillett, and L. Jones, "MARIA®M5: a multicentre clinical study to evaluate the ability of the Micrima radio-wave radar breast imaging system (MARIA®) to detect lesions in the symptomatic breast," *European Journal of Radiology*, vol. 116, pp. 61–67, 2019.

[35] M. A. Elahi, D. O'Loughlin, B. R. Lavoie, M. Glavin, E. Jones, E. C. Fear, and M. O'Halloran, "Evaluation of image reconstruction algorithms for confocal microwave imaging: Application to patient data," *Sensors*, vol. 18, no. 6, pp. 1–21, 2018.

[36] T. Reimer, D. Rodriguez Herrera, M. Solis Nepote, and S. Pistorius, "The use of a novel microwave radar reconstruction algorithm to image lesions in realistic 3D breast phantoms," in *2018 12th European Conference on Antennas and Propagation (EuCAP)*, (London, UK), pp. 1–5, IET, 2018.

[37] T. Reimer, M. S. Nepote, and S. Pistorius, "Initial results using an MLEM-based reconstruction algorithm for breast microwave radar imaging," in *2018 18th International Symposium on Antenna Technology and Applied Electromagnetics (ANTEM)*, (Waterloo, ON, Canada), pp. 1–2, IEEE, 2019.

[38] H. B. Lim, N. T. T. Nhung, E.-P. Li, and N. D. Thang, "Confocal microwave imaging for breast cancer detection: Delay-multiply-and-sum image reconstruction algorithm," *IEEE Transactions on Biomedical Engineering*, vol. 55, no. 6, pp. 1697–1704, 2008.

[39] M. O'Halloran, M. Glavin, and E. Jones, "Improved confocal microwave imaging of the breast using path-dependent signal weighting," in *2011 URSI General Assembly Scientific Symposium*, (Istanbul, Turkey), pp. 1–4, IEEE, 2011.

[40] M. Klemm, I. J. Craddock, J. A. Leendertz, A. Preece, and R. Benjamin, "Improved delay-and-sum beamforming algorithm for breast cancer detection," *International Journal of Antennas and Propagation*, vol. 2008, pp. 1–9, 2008.

[41] M. Klemm, J. A. Leendertz, D. Gibbins, I. J. Craddock, A. Preece, and R. Benjamin, "Microwave radar-based breast cancer detection: Imaging in inhomogeneous breast phantoms," *IEEE Antennas and Wireless Propagation Letters*, vol. 8, pp. 1349–1352, 2009.

[42] M. A. Elahi, B. R. Lavoie, E. Porter, M. Glavin, E. Jones, E. C. Fear, and M. O'Halloran, "Comparison of radar-based microwave imaging algorithms applied to experimental breast phantoms," in *2017 General Assembly and Scientific Symposium of the International Union of Radio Science (URSI GASS)*, vol. 3, (Montreal, QC, Canada), pp. 1–4, IEEE, 2017.

[43] J. M. Felício, J. M. Bioucas-Dias, J. R. Costa, and C. A. Fernandes, "Microwave breast imaging using a dry setup," *IEEE Transactions on Computational Imaging*, vol. 6, pp. 167–180, 2020.

[44] T. Reimer, J. Krenkevich, and S. Pistorius, "An open-access experimental dataset for breast microwave imaging," in *2020 14th European Conference on Antennas and Propagation (EuCAP)*, pp. 1–5, in press.

[45] D. R. Herrera, T. Reimer, M. Solis Nepote, and S. Pistorius, "Manufacture and testing of anthropomorphic 3D-printed breast phantoms using a microwave radar algorithm optimized for propagation speed," in *2017 11th European Conference on Antennas and Propagation (EuCAP)*, (Paris, France), pp. 3480–3484, IEEE, 2017.

[46] J. Garrett and E. Fear, "A new breast phantom with a durable skin layer for microwave breast imaging," *IEEE Transactions on Antennas and Propagation*, vol. 63, no. 4, pp. 1693–1700, 2015.

[47] M. J. Burfeindt, T. J. Colgan, R. Owen Mays, J. D. Shea, N. Behdad, B. D. Van Veen, and S. Hagness, "MRI-derived 3-D-printed breast phantom for microwave breast imaging validation," *IEEE Antennas and Wireless Propagation Letters*, vol. 11, pp. 1610–1613, 2012.

[48] N. Joachimowicz, B. Duchene, C. Conessa, and O. Meyer, "Reference phantoms for microwave imaging," in *2017 11th European Conference on Antennas and Propagation (EuCAP)*, (Paris, France), pp. 2719–2722, IEEE, 2017.

[49] M. T. Islam, M. Samsuzzaman, S. Kibria, and M. T. Islam, "Experimental breast phantoms for estimation of breast tumor using microwave imaging systems," *IEEE Access*, vol. 6, pp. 78587–78597, 2018.

[50] B. L. Oliveira, D. O'Loughlin, M. O'Halloran, E. Porter, M. Glavin, and E. Jones, "Microwave breast imaging: experimental tumour phantoms for the evaluation of new breast cancer diagnosis systems," *Biomedical Physics and Engineering Express*, vol. 4, no. 2, pp. 1–16, 2018.

[51] S. Di Meo, L. Pasotti, I. Iliopoulos, M. Pasian, M. Ettorre, M. Zhadobov, and G. Matrone, "Tissue-mimicking materials for breast phantoms up to 50 GHz," *Physics in Medicine and Biology*, vol. 64, no. 5, pp. 1–13, 2019.

[52] D. O'Loughlin, B. L. Oliveira, A. Santorelli, E. Porter, M. Glavin, E. Jones, M. Popovic, and M. O'Halloran, "Sensitivity and specificity estimation using patient-specific microwave imaging in diverse experimental breast phantoms," *IEEE Transactions on Medical Imaging*, vol. 38, no. 1, pp. 303–311, 2019.

[53] T. Rubaek, P. M. Meaney, P. Meincke, and K. D. Paulsen, "Nonlinear microwave imaging for breast-cancer screening using Gauss–Newton's method and the CGLS inversion algorithm," *IEEE Transactions on Antennas and Propagation*, vol. 55, no. 8, pp. 2320–2331, 2007.

[54] T. Henriksson, N. Joachimowicz, C. Conessa, and J. Bolomey, "Quantitative microwave imaging for breast cancer detection using a planar 2.45 GHz system," *IEEE Transactions on Instrumentation and Measurement*, vol. 59, no. 10, pp. 2691–2699, 2010.

[55] T. M. Grzegorczyk, P. M. Meaney, P. A. Kaufman, R. M. diFlorio-Alexander, and K. D. Paulsen, "Fast 3-D tomographic microwave imaging for breast cancer detection," *IEEE Transactions on Medical Imaging*, vol. 31, no. 8, pp. 1584–1592, 2012.

[56] A. Fhager, M. Gustafsson, and S. Nordebo, "Image reconstruction in microwave tomography using a dielectric Debeye model," *IEEE Transactions on Biomedical Engineering*, vol. 59, no. 1, pp. 156–166, 2012.

[57] A. Fouda and F. L. Teixeira, "Ultra-wideband microwave imaging of breast cancer tumors via Bayesian inverse scattering," *Journal of Applied Physics*, vol. 115, no. 6, pp. 1–8, 2014.

[58] R. Scapaticci, P. Kosmas, and L. Crocco, "Wavelet-based regularization for robust microwave imaging in medical applications," *IEEE Transactions on Biomedical Engineering*, vol. 62, no. 4, pp. 1195–1202, 2015.

[59] M. El-Shenawee and E. L. Miller, "Spherical harmonics microwave algorithm for shape and location reconstruction of breast cancer tumor," *IEEE Transactions on Medical Imaging*, vol. 25, no. 10, pp. 1258–1271, 2006.

[60] C. Kaye, I. Jeffrey, and J. LoVetri, "Improvement of multi-frequency microwave breast imaging through frequency cycling and tissue-dependent mapping," *IEEE Transactions on Antennas and Propagation*, vol. 67, no. 11, pp. 7087–7096, 2019.

[61] N. Abdollahi, J. LoVetri, and I. Jeffrey, "A combined algorithm for high resolution microwave breast imaging using Eigenfunction-based prior," in *2019 13th European Conference on Antennas and Propagation (EuCAP)*, (Krakow, Poland), pp. 1–3, IEEE, 2019.

[62] N. Abdollahi, D. Kurrant, P. Mojabi, M. Omer, E. Fear, and J. LoVetri, "Incorporation of ultrasonic prior information for improving quantitative microwave imaging of breast," *IEEE Journal on Multiscale and Multiphysics Computational Techniques*, vol. 4, pp. 98–110, 2019.

[63] M. Ronagh and M. Eshghi, "Hybrid genetic algorithm and particle swarm optimization based microwave tomography for breast cancer detection," in *2019 IEEE 9th Symposium on Computer Applications Industrial Electronics (ISCAIE)*, (Malaysia), pp. 244–248, IEEE, 2019.

[64] A. H. Golnabi, P. M. Meaney, S. D. Geimer, and K. D. Paulsen, "3-D microwave tomography using the soft prior regularization technique: Evaluation in anatomically realistic MRI-derived numerical breast phantoms," *IEEE Transactions on Biomedical Engineering*, vol. 66, no. 9, pp. 2566–2575, 2019.

[65] N. Simonov, B. Kim, K. Lee, S. Jeon, and S. Son, "Advanced fast 3-D electromagnetic solver for microwave tomography imaging," *IEEE Transactions on Medical Imaging*, vol. 36, no. 10, pp. 2160–2170, 2017.

[66] Z. Guo, Z. Miao, and P. Kosmas, "Application of the DBIM-TwIST algorithm to 3-D microwave tomography data," in *12th European Conference on Antennas and Propagation (EuCAP)*, (London, UK), pp. 1–4, IET, 2018.

[67] M. Azghani and F. Marvasti, "L2-regularized iterative weighted algorithm for inverse scattering," *IEEE Transactions on Antennas and Propagation*, vol. 64, no. 6, pp. 2293–2300, 2016.

[68] P. Mojabi and J. LoVetri, "Experimental evaluation of composite tissue-type ultrasound and microwave imaging," *IEEE Journal on Multiscale and Multiphysics Computational Techniques*, vol. 4, pp. 119–132, 2019.

[69] D. Rodriguez-Herrera, D. Flores-Tapia, and S. Pistorius, "Comparison of image quality metrics for electromagnetic wave propagation speed estimation in breast microwave radar imaging scenarios," in *2014 8th European Conference on Antennas and Propagation (EuCAP)*, (The Hague, Netherlands), pp. 516–519, IEEE, 2014.

[70] E. C. Fear and M. A. Stuchly, "Microwave system for breast tumor detection," *IEEE Microwave and Guided Wave Letters*, vol. 9, no. 11, pp. 470–472, 1999.

[71] E. C. Fear, J. Sill, and M. A. Stuchly, "Experimental feasibility study of confocal microwave imaging for breast tumor detection," *IEEE Transactions on Microwave Theory and Techniques*, vol. 51, no. 3, pp. 887–892, 2003.

[72] I. J. Craddock, A. Preece, J. Leendertz, M. Klemm, R. Nilavalan, and R. Benjamin, "Development of a hemi-spherical wideband antenna array for breast cancer imaging," in *2006 European Conference on Antennas and Propagation (EuCAP)*, (Nice, France), pp. 1–5, IEEE, 2006.

[73] D. Flores-Tapia, G. Thomas, and S. Pistorius, "A wavefront reconstruction method for 3-D cylindrical subsurface radar imaging," *IEEE Transactions on Image Processing*, vol. 17, no. 10, pp. 1908–1925, 2008.

[74] Y. Kuwahara, S. Miura, Y. Nishina, K. Mukumoto, H. Ogura, and H. Sakahara, "Clinical test of microwave mammography," in *2013 IEEE Antennas and Propagation Society International Symposium (APSURSI)*, (Orlando, FL, USA), pp. 2028–2029, IEEE, 2013.

[75] D. Byrne and I. J. Craddock, "Time-domain wideband adaptive beamforming for radar breast imaging," *IEEE Transactions on Antennas and Propagation*, vol. 63, no. 4, pp. 1725–1735, 2015.

[76] E. Bond, X. Li, S. Hagness, and B. D. Van Veen, "Microwave imaging via space-time beamforming for early detection of breast cancer," *IEEE Transactions on Antennas and Propagation*, vol. 51, no. 8, pp. 1690–1705, 2003.

[77] B. Guo, Y. Wang, J. Li, P. Stoica, and R. Wu, "Microwave imaging via adaptive beamforming methods for breast cancer detection," *Journal of Electromagnetic Waves and Applications*, vol. 20, no. 1, pp. 53–63, 2006.

[78] T. Reimer, M. Solis-Nepote, and S. Pistorius, "The impact of the inverse chirp z-transform on breast microwave radar image reconstruction," in *2019 European Microwave Conference in Central Europe (EuMCE)*, (Prague, Czech Republic), pp. 626–629, IEEE, 2019.

[79] L. A. Shepp and Y. Vardi, "Maximum likelihood reconstruction for emission tomography," *IEEE Transactions on Medical Imaging*, vol. 1, no. 2, pp. 113–122, 1982.

[80] R. C. Conceição, H. Medeiros, D. M. Godinho, M. O'Halloran, D. Rodriguez-Herrera, D. Flores-Tapia, and S. Pistorius, "Classification of breast tumor models with a prototype microwave imaging system," *Medical Physics*, vol. 47, no. 4, pp. 1860–1870, 2020.

[81] R. C. Conceição, H. Medeiros, M. O'Halloran, D. Rodriguez-Herrera, D. Flores-Tapia, and S. Pistorius, "Initial classification of breast tumour phantoms using a UWB radar prototype," in *2013 International Conference on Electromagnetics in Advanced Applications (ICEAA)*, (Torino, Italy), pp. 720–723, IEEE, 2013.

[82] R. C. Conceição, H. Medeiros, M. O'Halloran, D. Rodriguez-Herrera, D. Flores-Tapia, and S. Pistorius, "SVM-based classification of breast tumour phantoms using a UWB radar prototype system," in *2014 URSI General Assembly and Scientific Symposium (URSI GASS)*, (Beijing, China), pp. 1–4, IEEE, 2014.

[83] B. Gerazov and R. C. Conceicao, "Deep learning for tumour classification in homogeneous breast tissue in medical microwave imaging," in *IEEE EUROCON 2017 -17th International Conference on Smart Technologies*, (Ohrid, Macedonia), pp. 564–569, IEEE, 2017.

[84] T. Reimer, J. Sacristan, and S. Pistorius, "Improving the diagnostic capability of microwave radar imaging systems using machine learning," in *2019 13th European Conference on Antennas and Propagation (EuCAP)*, (Krakow, Poland), pp. 1–5, IEEE, 2019.

[85] J. Sacristán, B. L. Oliveira, and S. Pistorius, "Classification of electromagnetic signals obtained from microwave scattering over healthy and tumorous breast models," in *2016 IEEE Canadian Conference on Electrical and Computer Engineering (CCECE)*, (Vancouver, BC, Canada), pp. 1–5, IEEE, 2016.

[86] A. Santorelli, Y. Li, E. Porter, M. Popović, and M. Coates, "Investigation of classification algorithms for a prototype microwave breast cancer monitor," in *8th Eur. Conf. Antennas Propag. (EuCAP)*, (The Hague, Netherlands), pp. 320–324, IEEE, 2014.

[87] H. Song, Y. Li, and A. Men, "Microwave breast cancer detection using time-frequency representations," *Medical and Biological Engineering and Computing*, vol. 56, no. 4, pp. 571–582, 2018.

[88] M. A. Aldhaeebi, T. S. Almoneef, A. Ali, Z. Ren, and O. M. Ramahi, "Near field breast tumor detection using ultra-narrow band probe with machine learning techniques," *Scientific Reports*, vol. 8, pp. 1–16, 2018.

[89] S. P. Rana, M. Dey, G. Tiberi, L. Sani, A. Vispa, G. Raspa, M. Duranti, M. Ghavami, and S. Dudley, "Machine learning approaches for automated lesion detection in microwave breast imaging clinical data," *Scientific Reports*, vol. 9, pp. 1–12, 2019.

[90] J. LoVetri, M. Asefi, N. Abdollahi, K. Brown, N. Geddert, and I. Jeffrey, "Phantom study of a flat-faceted air-based microwave breast imaging system," in *12th European Conference on Antennas and Propagation (EuCAP)*, (London, UK), pp. 1–2, IET, 2018.

[91] J. Tobon-Vasquez, F. Vipiana, M. Casu, M. Vacca, I. Sarwar, R. Scapaticci, N. Joachimowicz, and B. Duchene, "Experimental assessment of qualitative microwave imaging using a 3-D realistic breast phantom," in *2017 11th European Conference on Antennas and Propagation (EuCAP)*, (Paris, France), pp. 2728–2731, IEEE, 2017.

[92] N. Z. Naghsh, A. Ghorbani, and H. Amindavar, "Compressive sensing for microwave breast cancer imaging," *IET Signal Processing*, vol. 12, no. 2, pp. 242–246, 2017.

[93] W.-K. Park, H. P. Kim, K.-J. Lee, and S.-H. Son, "MUSIC algorithm for location searching of dielectric anomalies from S-parameters using microwave imaging," *Journal of Computational Physics*, vol. 348, pp. 259–270, 2017.

[94] E. Norouzzadeh, S. Chamaani, and J. Moll, "Parametric study of time-reversal imaging for the detection of tumors in MRI-derived breast phantoms," in *2019 12th German Microwave Conference (GeMiC)*, (Stuttgart, Germany), pp. 206–209, IEEE, 2019.

[95] A. Alqallaf and R. Dib, "Focused synthetic aperture radar imaging approach for multi-tumor screening," *Journal of Engineering Research*, vol. 7, no. 3, pp. 232–243, 2019.

[96] A. Naghibi, M. S. H. Rad, V. Khorashadi-Zadeh, and A. R. Attari, "Skin artifact removal algorithms for radar-based microwave breast cancer detection," in *Iranian Conference on Electrical Engineering (ICEE)*, (Mashhad, Iran), pp. 659–664, IEEE, 2018.

[97] E. A. Aydin and M. K. Keles, "UWB rectangular microstrip patch antenna design in matching liquid and evaluating the classification accuracy in data mining using random forest algorithm for breast cancer detection with microwave," *Journal of Electrical Engineering and Technology*, vol. 14, pp. 2127–2136, 2019.

[98] D. O'Loughlin, M. A. Elahi, E. Porter, A. Shahzad, B. L. Oliveira, M. Glavin, E. Jones, and M. O'Halloran, "Open-source software for microwave radar-based image reconstruction," in *12th European Conference on Antennas and Propagation (EuCAP)*, (London, UK), pp. 1–4, IET, 2018.

[99] T. Rydholm, A. Fhager, M. Persson, and P. Meaney, "A first evaluation of the realistic supelec-breast phantom," *IEEE Journal of Electromagnetics, RF and Microwaves in Medicine and Biology*, vol. 1, no. 2, pp. 59–65, 2017.

[100] N. Joachimowicz, B. Duchêne, C. Conessa, and O. Meyer, "Easy-to-produce adjustable realistic breast phantoms for microwave imaging," in *2016 10th European Conference on Antennas and Propagation (EuCAP)*, (Davos, Switzerland), pp. 1–4, IEEE, 2016.

[101] A. Mashal, F. Gao, and S. C. Hagness, "Heterogeneous anthropomorphic phantoms with realistic dielectric properties for microwave breast imaging experiments," *Microwave and Optical Technology Letters*, vol. 53, no. 8, pp. 1896–1902, 2011.

[102] N. Joachimowicz, C. Conessa, T. Henriksson, and B. Duchêne, "Breast phantoms for microwave imaging," *IEEE Antennas and Wireless Propagation Letters*, vol. 13, pp. 1333–1336, 2014.

[103] E. Porter, J. Fakhoury, R. Oprisor, M. Coates, and M. Popović, "Improved tissue phantoms for experimental validation of microwave breast cancer detection," in *4th European Conference on Antennas and Propagation (EuCAP)*, (Barcelona, Spain), pp. 1–5, IEEE, 2010.

[104] T. Reimer, M. Solis-Nepote, and S. Pistorius, "The impact of the inverse chirp z-transform on breast microwave radar image reconstruction," *International Journal of Microwave and Wireless Technologies*, pp. 1–7, 2020.

[105] T. Reimer, M. Solis-Nepote, and S. Pistorius, "The application of an iterative structure to the delay-and-sum and the delay-multiply-and-sum beamformers in breast microwave imaging," *Diagnostics*, vol. 10, no. 6, pp. 1–15, 2020.

[106] A. Modiri and K. Kiasaleh, "Permittivity estimation for breast cancer detection using particle swarm optimization algorithm," in *33rd Annual International Conference of the IEEE Engineering in Medicine and Biology Society*, (Boston, MA, USA), pp. 1359–1362, IEEE, 2011.

[107] T. Williams, E. C. Fear, and D. W. Westwick, "Tissue sensing adaptive radar for breast cancer detection: investigations of reflections from the skin," in *IEEE Antennas and Propagation Society Symposium, 2004*, vol. 3, (Monterey, CA, USA), pp. 2436–2439, IEEE, 2004.

[108] S. Caorsi and C. Lenzi, "Skin removal techniques for breast cancer radar detection based on artificial neural networks," in *2015 IEEE 15th Mediterranean Microwave Symposium (MMS)*, (Lecce, Italy), pp. 1–4, IEEE, 2015.

[109] M. Sarafianou, I. J. Craddock, and T. Henriksson, "Towards enhancing skin reflection removal and image focusing using a 3-D breast surface reconstruction algorithm," *IEEE Transactions on Antennas and Propagation*, vol. 61, no. 10, pp. 5343–5346, 2013.

[110] B. Maklad, C. Curtis, E. Fear, and G. Messier, "A skin response estimation and suppression technique for radar-based microwave breast imaging applications," in *2012 6th European Conference on Antennas and Propagation (EUCAP)*, (Prague, Czech Republic), pp. 1772–1775, IEEE, 2012.

[111] T. Pope, M. Read, T. Medsker, A. Buschi, and A. Brenbridge, "Breast skin thickness: normal range and causes of thickening shown on film-screen mammography," *Canadian Association of Radiologists Journal*, vol. 35, no. 4, pp. 365–368, 1984.

[112] M. Lazebnik, D. Popovic, L. McCartney, C. B. Watkins, M. J. Lindstrom, J. Harter, S. Sewall, T. Ogilvie, A. Magliocco, T. M. Breslin, W. Temple, D. Mew, J. H. Booske, M. Okoniewski, and S. Hagness, "A large-scale study of the ultrawideband microwave dielectric properties of normal, benign and malignant breast tissues obtained from cancer surgeries," *Physics in Medicine and Biology*, vol. 52, no. 20, pp. 6093–6115, 2007.

[113] D. Frickey, "Using the inverse chirp-z transform for time-domain analysis of simulated radar signals," in *Proceedings of the 5th International Signal Processing Applications and Technology Conference*, (Dallas, TX, USA), pp. 1366–1371, USDOE, 1994.

[114] P. Hazarika, A. Santorelli, and M. Popovic, "Investigation of antenna array configurations for microwave radar breast screening," in *2016 17th International Symposium on Antenna Technology and Applied Electromagnetics (ANTEM)*, (Montreal, QC, Canada), pp. 1–2, IEEE, 2016.

[115] Y. Le Cun, B. Boser, J. Denker, D. Henderson, R. Howard, W. Hubbard, and L. Jackel, "Handwritten digit recognition with a back-propagation network," in *Advances in Neural Information Processing Systems*, pp. 396–404, 1990.

[116] D. Kingma and J. Ba, "Adam: A method for stochastic optimization," in *International Conference for Learning Representations*, (San Diego, CA, USA), pp. 1–15, 2015.

[117] A. Rodriguez-Ruiz, E. Krupinski, J.-J. Mordang, K. Schilling, S. H. Heywang-Kobrunner, I. Sechopoulos, and R. M. Mann, "Detection of breast cancer with mammography: Effect of an artificial intelligence support system," *Radiology*, vol. 290, no. 2, pp. 305–314, 2019.

[118] N. Houssami, G. Kirkpatrick-Jones, N. Noguchi, and C. I. Lee, "Artificial intelligence (AI) for the early detection of breast cancer: A scoping review to assess AI's potential in breast screening practice," *Expert Review of Medical Devices*, vol. 16, no. 5, pp. 351–362, 2019.